

Time-resolved studies of electron-phonon coupling in gold nanoparticles and hybrid nanoparticle assemblies

Dissertation

submitted to the Department of Chemistry,
Faculty of Mathematics, Informatics and Natural Sciences
of the University of Hamburg

in fulfillment of the requirements for
the degree of Doctor Rerum Naturalium

by
Dominik Höing

Hamburg

2023

This work was conducted between April 2019 and July 2023 in the group of Holger Lange at the Institute of Physical Chemistry, Department of Chemistry, Faculty of Mathematics, Informatics and Natural Sciences, University of Hamburg, Germany.

Examiner: Dr. Holger Lange
Co-examiner: PD Dr. Tobias Kipp
Date of Submission: 04.08.2023
Date of the oral defense: 24.11.2023
Date of print release: 16.01.2023

Publications

- **D. Hoeing**, R. Salzwedel, L. Worbs, Y. Zhuang, A.K. Samanta, J. Lübke, A.D. Estillore, K. Dlugolecki, C. Passow, B. Erk, N. Ekanayake, D. Ramm, J. Correa, C.C. Papadopoulou, A.T. Noor, F. Schulz, M. Selig, A. Knorr, K. Ayyer, J. Küpper, H. Lange, Optically induced electron density gradients drive coherent plasmonic nanoparticle oscillations. *Nano Letters* (2023), <https://doi.org/10.1021/acs.nanolett.3c00920>
- R. Salzwedel, A. Knorr, **D. Hoeing**, H. Lange, M. Selig, Theory of radial oscillations in metal nanoparticles driven by optically induced electron density gradients. *Journal of Chemical Physics*, **158**, 064107 (12 pp) (2023), <https://doi.org/10.1063/5.0139629>
- M. Herran, S. Juergensen, M. Kessens, **D. Hoeing**, A. Köppen, A. Sousa-Castillo, W.J. Parak, H. Lange, S. Reich, F. Schulz, E. Cortés, Plasmonic Bimetallic Two-Dimensional Supercrystals for H₂ Generation, *Nature Catalysis*, **6**, 1205-1214, (2023), <https://doi.org/10.1038/s41929-023-01053-9>
- Y.U. Staechelin, **D. Hoeing**, F. Schulz, H. Lange. Size-Dependent Electron-Phonon Coupling in Monocrystalline Gold Nanoparticles. *ACS Photonics* **8**, 752-757 (2021), <https://doi.org/10.1021/acsp Photonics.1c00078>
- **D. Hoeing**, F. Schulz, N.S. Mueller, S. Reich, H. Lange. Dark plasmon modes for efficient hot electron generation in multilayers of gold nanoparticles. *The Journal of Chemical Physics* **152**, 064710 (10 pp) (2020), <https://doi.org/10.1063/1.5131696>
- N.S. Mueller, B.G.M. Vieira, **D. Hoeing**, F. Schulz, E.B. Barros, H. Lange, S. Reich. Direct optical excitation of dark plasmon modes for hot electron generation. *Faraday Discussions* **214**, 159-173 (2019), <https://doi.org/10.1039/C8FD00149A>

Contents

1	Introduction	15
2	Theoretical background	19
2.1	Plasmonic properties of gold nanoparticles	19
2.1.1	Basic principles	19
2.1.2	Localized surface plasmon resonance	25
2.2	Hot carrier dynamics in gold nanoparticles	30
2.2.1	Overview	30
2.2.2	Electron-electron scattering	32
2.2.3	Electron-phonon coupling	33
2.2.4	Parameter studies on electron-phonon coupling in AuNP	36
3	Methods	45
3.1	Transient absorption spectroscopy	45
3.1.1	Introduction	45
3.1.2	Technical Overview	49
3.1.3	Data analysis	56
3.2	Sample preparation	61
3.2.1	Gold nanoparticle synthesis	61
3.2.2	Quality assessment	64
4	Temperature-dependent electron-phonon coupling	67
4.1	Two temperature model simulations	69

4.2	Temperature-dependent transient absorption	71
4.3	Discussion	79
5	Excitation mechanism of coherent acoustic phonon modes	83
5.1	Introduction	84
5.2	Theoretical descriptions of breathing modes	87
5.3	Experiments and data analysis	94
5.3.1	Particle synthesis	94
5.3.2	Single-particle imaging	96
5.3.3	Transient absorption spectroscopy	105
5.3.4	Two-temperature model simulations	107
5.4	Results and discussion	108
6	Hot electron dynamics of hybrid Au-Pt superlattices	119
6.1	Properties of AuNP superlattices	121
6.1.1	Plasmon-polariton modes and ultrastrong light-matter coupling	121
6.1.2	Hot-electron dynamics of AuNP superlattices	125
6.2	Hot electrons and hybrid systems for photocatalysis	128
6.3	Experiments	130
6.3.1	Transient absorption spectroscopy	130
6.3.2	Superlattice assembly	131
6.3.3	Photocatalysis	132
6.3.4	Optical micro-transmission and -reflection spectroscopy	133
6.3.5	Finite-difference time-domain simulations	133
6.3.6	Materials	134
6.4	Results	134
6.4.1	Samples	134
6.4.2	Photocatalytic properties	136
6.4.3	Hot electron dynamics	140
7	Summary and outlook	147
8	Appendix	175

List of abbreviations

2TM	two-temperature model
AA	ascorbic acid
AuNP	gold nanoparticle
AuNR	gold nanorod
BBO	barium borate
BSG	borosilicate glass
CMOS	complementary metal-oxide-semiconductor
CTAB	cetyltrimethylammonium bromide
CTAC	cetyltrimethylammonium chloride
DEG	diethylene glycol
e-e	electron-electron
e-ph	electron-phonon
FDTD	finite-difference time-domain
FEL	free-electron laser
FWHM	full width at half maximum
HAuCl₄	tetrachloroauric acid
IRF	instrument response function
ITO	indium tin oxide
LSPR	localized surface plasmon resonance
NA	numerical aperture
NaBH₄	sodium borohydride
ND	neutral density
NIR	near-infrared
NP	nanoparticle
OPA	optical parametric amplification
OPG	optical parametric generation
PSSH	thiolated polystyrene
PtNP	platinum nanoparticle
SAXS	small-angle x-ray scattering
SERS	surface-enhanced Raman scattering
SHG	second-harmonic generation
SPI	single-particle imaging
SPP	surface plasmon-polariton
TA	transient absorption
TEM	transmission electron microscopy
THF	tetrahydrofuran
WLC	white-light continuum
WLG	white-light generation
XRD	x-ray diffraction
YAG	Yttrium aluminium garnet

Abstract

Gold nanoparticles have gained significant attention in nanoscience for their plasmonic properties. The localized surface plasmon resonance of gold nanoparticles is a strong interaction between electrons and light, which results in high absorbance in the visible spectrum, highly localized enhancement of the electric field at the particle surface, as well as the generation of highly excited electrons. The lifetime of these "hot electrons" is on a picosecond timescale before they lose their energy through electron-phonon coupling. Both the excitation of the localized surface plasmon resonance and the resulting hot electron dynamics have been explored in context of fundamental light-matter coupling and applications that rely on light-energy conversion such as photocatalysis, solar cells, or photothermal cancer treatment. For example, self-assembled gold nanoparticle superlattices have been presented as a new metamaterial with optical properties exclusive to this type of platform. Furthermore, manipulating the hot electron dynamics might lead to charge transfer reactions that are otherwise energetically unfavorable. However, the fast relaxation time of hot electrons is detrimental to their utilization in many applications.

Electron-phonon coupling is usually described as a heat transfer from the electron to phonon distribution through the so-called two-temperature model, which includes a characteristic coupling factor. Exploring the dependency of this coupling factor on a variety of parameters has been at the heart of studying hot electron dynamics in gold nanoparticles for the last two decades, but there still remain open questions as to the valid parameter space of the two-temperature model as well as the influence of hot electrons in applications based on light-energy conversion. A powerful tool to address these questions is transient absorption spectroscopy. This technique allows assessing the electron temperature in gold nanoparticles on a femto- to picosecond timescale. Furthermore, new ultrashort x-ray techniques for studying the dynamic behavior of nanostructures are constantly developed at free-electron laser facilities.

In this work, transient absorption spectroscopy and single-particle imaging have been used to gain a deeper understanding of the hot electron dynamics

in plasmonic gold nanoparticles. In particular, three studies were conducted: 1) Typically, time-resolved studies of hot electron dynamics are conducted at room temperature. Using temperature-dependent transient absorption spectroscopy, the validity of the two-temperature model was explored for the low temperature range from 100 K to 350 K. The results reproduced the predictions made by the two-temperature model throughout the whole temperature range, even without including a temperature-dependent electron-phonon coupling factor or heat capacity below gold's Debye temperature in the model. 2) Single-particle imaging was established as a powerful technique to study the onset of coherent radial phonon modes, so-called "breathing modes". The results confirm the need for an additional excitation source to electron-phonon coupling described by the two-temperature model, which was previously conceptualized as "hot electron pressure". A new theoretical framework has been developed, which revealed the electron-density gradient as a novel description of this additional source. 3) Hybrid superlattices consisting of plasmonic gold and catalytic platinum nanoparticles were introduced as a novel platform for photocatalysis. Wavelength-dependent experiments have indicated a catalytic mechanism based on the local field enhancement by the gold nanoparticles. In this study, a competing effect by hot electron transfer from gold to platinum particles could not be found by transient absorption measurements, further supporting the proposed mechanism.

Zusammenfassung

Goldnanopartikel gehören aufgrund ihrer plasmonischen Eigenschaften zu den weit verbreitetsten Materialien in der Erforschung von Licht-Materie Wechselwirkungen. Die lokalisierte Oberflächenplasmonenresonanz ist eine starke Wechselwirkung zwischen elektrischem Feld und Elektronen und resultiert in hoher Absorption sichtbaren Lichts, einer starken Lokalisierung des elektrischen Felds an der Partikeloberfläche sowie der Erzeugung hoch angeregter Ladungsträger. Diese "heißen" Elektronen haben nur eine sehr geringe Lebenszeit von wenigen Pikosekunden bevor sie ihre Energie über Elektron-Phonon Kopplung an Gitterschwingungen abgeben. Sowohl die lokalisierte Oberflächenplasmonenresonanz als auch die Dynamik heißer Ladungsträger wurden in den letzten Jahrzehnten ausführlich in verschiedenen Bereichen erforscht. Dazu gehören sowohl fundamentale Licht-Materie Wechselwirkung als auch Anwendungen, welche auf Licht-Energie-Umwandlung basieren wie etwa Photokatalyse, Solarzellen, oder photothermische Krebstherapie. Zu den aktuellsten Entwicklungen gehören selbstangeordnete Nanopartikel-Filme - ein Metamaterial mit neuartigen optischen Eigenschaften. Außerdem könnte die Manipulation der Dynamik heißer Ladungsträger Reaktionen und Energieübertragungen ermöglichen, wo sie ansonsten energetisch ungünstig wären. Die Nutzung heißer Elektronen in Anwendungen wird jedoch durch ihre schnellen Relaxationszeiten erschwert.

Elektron-Phonon Kopplung wird üblicherweise als Wärmetransfer von Elektronen zu Phononen beschrieben. Dazu wird ein Zwei-Temperatur Modell angewendet, welches einen charakteristischen Kopplungsfaktor beinhaltet. Die Untersuchung der Abhängigkeit dieses Kopplungsfaktors von einer Vielzahl von Parametern stand in den letzten zwei Jahrzehnten im Mittelpunkt der Untersuchungen zur Dynamik heißer Elektronen in Goldnanopartikeln. Dabei ist der Gültigkeitsbereich des Zwei-Temperatur Modells noch nicht vollständig untersucht. Welchen Einfluss heiße Ladungsträger außerdem in photokatalytischen Reaktionen spielen ist ebenfalls eine offene Frage. Die Erforschung dieser offenen Fragestellungen zur Dynamik heißer Ladungsträger profitiert von der permanenten Entwicklung zeitaufgelöster Untersuchungsmethoden.

Während zeitaufgelöste Absorptionsspektroskopie eine etablierte und oft angewendete Methode darstellt, werden an Freie-Elektronen-Lasern neue Experimente basierend auf ultrakurzen Röntgenpulsen entwickelt, die zur Erforschung der dynamischen Eigenschaften von Nanopartikeln beitragen können, z.B. "Single-Particle Imaging".

In dieser Arbeit wurden transiente Absorptionsspektroskopie und Single-Particle Imaging eingesetzt, um ein tieferes Verständnis der Dynamik heißer Elektronen in plasmonischen Goldnanopartikeln zu erlangen. Insbesondere wurden drei Studien durchgeführt: 1) Mithilfe temperaturabhängiger transienter Absorptionsspektroskopie wurde die Gültigkeit des Zwei-Temperatur Modells für tiefe Temperaturen (100 K bis 350 K) untersucht. Die Ergebnisse reproduzierten die Vorhersagen des Zwei-Temperatur Modells über den gesamten Temperaturbereich, auch ohne Einbeziehung eines temperaturabhängigen Elektron-Phonon Kopplungsfaktors oder Wärmekapazität unterhalb der Debye-Temperatur von Gold in das Modell. 2) Single-Particle Imaging hat sich als leistungsstarke Technik zur Untersuchung kohärenter radialer Phononenmoden, sogenannter „breathing modes“, herausgestellt. Die Ergebnisse bestätigen die Notwendigkeit einer zusätzlichen Anregungsquelle zur Elektron-Phonon Kopplung, die zuvor als „Druck heißer Elektronen“ konzipiert wurde. Es wurde ein theoretischer Rahmen entwickelt, aus dem der Elektronendichtegradient als neuartige Beschreibung dieser zusätzlichen Quelle hervorgeht. 3) Die photokatalytischen Eigenschaften hybrider Superkristalle bestehend aus plasmonischen Gold- und katalytischen Platinanopartikeln wurden erforscht. Die Abhängigkeit der photokatalytischen Aktivität von der Anregungswellenlänge korreliert mit der Verstärkung des elektrischen Feldes in den Zwischenräumen der Goldnanopartikel durch die Plasmonen. Ein konkurrierender Einfluss durch den Transfer heißer Ladungsträger von Goldnanopartikeln zu Platinanopartikeln wurde mittels transienter Absorptionsspektroskopie untersucht. Dabei konnte kein Hinweis auf einen Elektronentransfer festgestellt und so der vorgeschlagene Mechanismus basierend auf der lokalen Feldverstärkung weiter bekräftigt werden.

Chapter 1

Introduction

Nanoscience studies the production, manipulation and properties of materials on the nanometer scale. In this size regime many materials change their behavior compared to their bulk counterparts. Among the many nanomaterials, noble metal nanoparticles have gained significant attention due to their plasmonic properties. A plasmon resonance is a collective excitation of conduction electrons at the surface of noble metals. Noble metal nanoparticles in particular exhibit localized surface plasmon resonances, which interact strongly with light, resulting in special absorption features and near-field enhancement of the electromagnetic field on sub-wavelength levels [1–4].

Among the metals studied in this context gold nanostructures have attracted significant - if not the most - attention in the scientific community. Two main reasons can be identified for that: Chemically, gold nanoparticles (AuNP) can be produced in mild conditions and through well-developed surface chemistry, they are passivated and can be tailored for application in different scenarios [5, 6]. Furthermore, the frequency of the localized surface plasmon resonance (LSPR) of AuNP is in the visible to near-infrared spectrum, which

simplifies its observation by optical means [4]. While the theoretical basis for describing the optical properties of AuNP has been introduced by Gustav Mie in 1908 [7], the field of AuNP-based plasmonics has been aided by the development of robust synthesis protocols such as the Turkevich method published in 1951 [8]. In line with the common theme in nanoscience, the relation between the AuNP's structure and their physical properties has been widely studied since then. For example, the size and shape of the nanostructures are deeply connected to the resonance width and frequency of the LSPR, respectively [9]. Recently, the achievements made in the field of nanoparticles synthesis have progressed towards using these as building blocks for metamaterials, which exhibit new collective properties [10–12].

The studies presented in this thesis all revolve around the question of how the energy absorbed by the plasmonic AuNPs is converted afterwards: Over the last two decades it has been established, that the optical excitation of AuNPs generates highly energetic charge carriers on a very short timescale [13]. These are thus termed "hot electrons" and their dynamic behavior has been widely studied. The common picture of hot electron dynamics includes four steps: (1) The dephasing of the LSPR or the excitation of direct transitions produce highly excited "non-thermal" electrons [14]. (2) Redistribution of energy within the electrons through inelastic scattering forms a thermal hot electron distribution [15, 16]. (3) The energy of the hot electron distribution transfers to phonons through electron-phonon (e-ph) coupling [13, 17–24] and (4) the energy of the phonons finally dissipates to the surrounding of the AuNP [25]. These processes are separated in their time-scale: Plasmon dephasing occurs within a few femtoseconds, electron-electron scattering within a few hundred femtoseconds, e-ph coupling within a few picoseconds and energy dissipation within a few hundred picoseconds to nanoseconds [13].

The progress made in the fields of plasmonics and hot electron science goes hand in hand with the development of the necessary tools to study them. For plasmonics and plasmonic metamaterials the ongoing improvement of synthesis routes and assembly protocols has been crucial [12, 26–28]. Studying the hot electron dynamics by optical means only became possible because of the development of ultrashort pulsed laser systems with sufficient time-resolution.

This included the invention of chirped-pulse amplification by Donna Strickland and Gérard Mourou in 1985 [29], which was awarded with the Nobel Prize in physics in 2018 [30]. Ultrashort laser pulses are now routinely used for time-resolved optical spectroscopy with femto- to picosecond resolution such as transient absorption (TA) spectroscopy [31, 32], which is the main experimental technique employed in this work. Furthermore, with the recent development of ultrashort x-ray techniques at free-electron laser facilities, new possibilities to study nanostructures such as single-particle imaging (SPI) have emerged [33, 34].

The ability to understand and utilize the plasmonic properties and hot electron dynamics of gold nanoparticles is promising for various reasons. These range from a fundamental science perspective in the context of light-matter [11, 35] and e-ph coupling [13] to the development of plasmonic and hot electron based applications such as photocatalysis [36–38], solar energy conversion [39], sensing [40, 41] or photothermal cancer treatment [42]. In all of these fields, a deep understanding of the hot electron dynamics of plasmonic materials is critical. The work presented in this thesis aims to contribute to this understanding. In particular, the following three studies will be presented:

Temperature-dependent electron-phonon coupling

Electron-phonon coupling can be conceptualized as heat transfer from an electron to phonon distribution through a "two-temperature model" (2TM) [13, 43]. This model assigns temperatures to each distribution and the energy transfer depends on the respective heat capacities and a material-specific coupling factor g . The first study seeks to explore the validity of this model at low temperatures down to 100 K, where the phonon heat capacity becomes a function of temperature.

Excitation mechanism of coherent acoustic phonon modes

Electron-phonon coupling also leads to the excitation of coherent acoustic phonon modes, which result in the periodic expansion of the particle diameter, so-called "breathing modes" [44–47]. The determination of the exact excitation mechanism of breathing modes has been proven difficult by standard techniques such as transient absorption spectroscopy and disparities between observations and models could only be resolved by introducing phenomenological factors into the models in the past [45, 48, 49]. In the second study, recently developed single-particle imaging has been utilized to study the breathing mode excitation and a new theoretical framework was used to understand the mechanism.

Hot electron dynamics of hybrid Au-Pt superlattices

Highly ordered, self-assembled AuNP "superlattices" have emerged as a new plasmonic metamaterial with optical properties exclusive to this platform [11, 12, 50]. At the moment the assembly protocols are expanded to produce hybrid superlattices, introducing new materials and functionality. In the third study, the photocatalytic properties of a hybrid superlattice containing AuNP and platinum nanoparticles (PtNP) are studied. In an antenna-reactor geometry, the plasmonic particles concentrate the electromagnetic energy into highly-localized nanometer sized volumes, 'hot-spots', where they seem to amplify the catalytic activity of the PtNP. To examine the competing contribution of hot charge carriers to this process, the hot electron dynamics of the AuNP and Au-Pt superlattices have been studied by transient absorption spectroscopy.

Before these studies are presented, the theoretical foundation of plasmonics and hot electron dynamics is revisited in chapter 2, followed by the description of the methodology used throughout this work in chapter 3. The three studies mentioned above are presented in chapters 4, 5 and 6 and contain detailed descriptions of the specific theory, literature and methodology of that respective part.

Chapter 2

Theoretical background

In this chapter the current state of the research on hot electron dynamics in AuNP following the excitation of the LSPR is presented. After introducing the general concepts of plasmonics in AuNP the current understanding of hot carrier dynamics that follow the plasmon excitation is discussed.

2.1 Plasmonic properties of gold nanoparticles

2.1.1 Basic principles

The starting point for describing the optical properties of metals such as gold is the free-electron model developed in the early 20th century by the successive works of Paul Drude and Hendrick Antoon Lorentz. The Drude-Lorentz model is a classical description of the electron transport properties associated with free electrons, i.e. electrons that are not bound to a specific

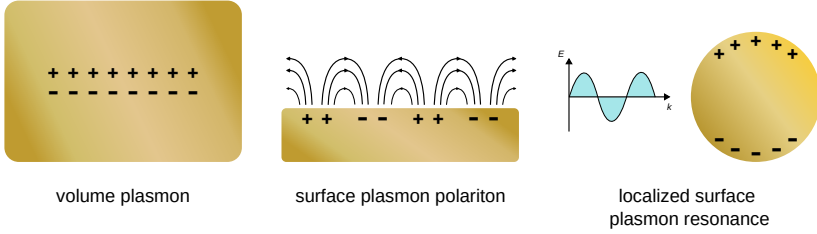


Figure 2.1: Depiction of different plasmon oscillation types in gold.

atomic core and therefore do not experience a restoring force [51]. This theory was further developed to adhere to Fermi-Dirac statistics by Arnold Sommerfeld [52]. The equation of motion of free electrons in an electromagnetic field $E(t) = E_0 e^{-i\omega t}$ [51] is

$$m_0 \ddot{x} + m_0 \gamma \dot{x} = -eE(t) \quad (2.1)$$

where m_0 is the electron mass, γ is the damping rate and e is the electron charge. Choosing $x(t) = x_0 e^{-i\omega t}$ leads to the solution

$$x(t) = \frac{e}{m_0(\omega^2 + i\gamma\omega)} E(t). \quad (2.2)$$

The electric displacement in a metal is given by $D = \epsilon_0 \epsilon_r E = \epsilon_0 E + P$ with the polarization $P = Nex$. Inserting equation 2.2 into these expressions yields:

$$D(t) = \epsilon_0 E(t) - \frac{Ne^2 E(t)}{m_0(\omega^2 + i\gamma\omega)}, \quad (2.3)$$

resulting in the equation for the dielectric function of the material:

$$\epsilon_r(\omega) = 1 - \frac{Ne^2}{\epsilon_0 m_0} \frac{1}{\omega^2 + i\gamma\omega} = 1 - \frac{\omega_p^2}{\omega^2 + i\gamma\omega}. \quad (2.4)$$

ω_p is the plasma frequency and defines the natural resonance frequency of a free electron gas oscillating against the background of a positive ionic lattice.

$$\omega_p = \sqrt{\frac{Ne^2}{\epsilon_0 m_0}} \quad (2.5)$$

N is the electron density. This charge oscillation is the plasma resonance or (volume) *plasmon*. In the low damping regime ($\gamma \rightarrow 0$) the dielectric function becomes

$$\epsilon_r(\omega) = 1 - \frac{\omega_p^2}{\omega^2} \quad (2.6)$$

with the dispersion relation (also shown in Fig. 2.2a):

$$\omega^2 = \omega_p^2 + k^2 c^2 \quad (2.7)$$

Therefore, the dielectric function $\epsilon_r = 0$ at the plasma frequency. This shows the longitudinal character of the volume plasmon oscillation. Because electromagnetic waves are transversal, volume plasmons are not excitable by light ($D = \epsilon_r \epsilon_0 E = 0$). Instead, other forms of excitation mechanisms have to be used to study this effect, like in electron energy loss spectroscopy [1, 51].

However, as the dielectric function is related to the refractive index via $n = \sqrt{\epsilon_r}$, the plasma frequency directly influences the optical properties of a material: the plasma frequency separates the transparency regime ($\omega > \omega_p$) from the reflectivity regime ($\omega < \omega_p$) (cf. Fig. 2.2b). Because most metals' plasma

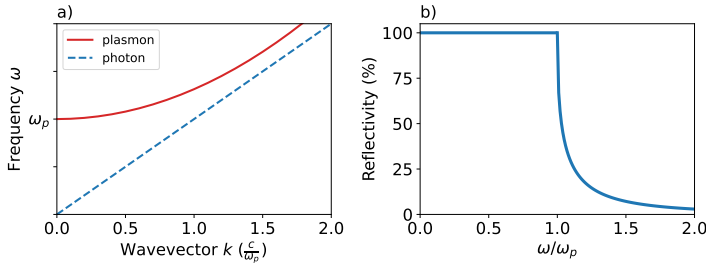


Figure 2.2: **a)** Dispersion relation of volume plasmons. **b)** Reflectivity of a metal in relation to the plasma frequency.

frequency is in the UV spectral region, they appear highly reflective in the visible.

Gold is one of few metals that have additional optical features in the visible range: interband absorption from the $5d$ to the $6sp$ band. This gives gold its distinct color compared to most colorless metals. Thus, the Drude-Lorentz model is only a good approximation of gold's optical properties for near infrared (NIR) wavelengths and longer [51]. To account for interband absorption the dielectric function is modified:

$$\epsilon_r(\omega) = \epsilon_{ib}(\omega) + 1 - \frac{\omega_p^2}{\omega^2 + i\gamma\omega} \quad (2.8)$$

In 1972 Johnson and Christy have measured gold's refractive index by reflectivity and transmission measurements (cf. Fig. 2.3) [53]. These data can be converted to the dielectric function and are nowadays commonly used to model gold's classical optical behavior.

In the context of this work it is also noteworthy that the dielectric function depends on the electron temperature. Brown et al. have pointed out that the

electron temperature will affect the Fermi distribution of the electrons and the electron-electron (e-e) scattering rate, which in turn lead to changes in the dielectric function of gold [22]. The dependence of the LSPR on temperature will be discussed in the next section.

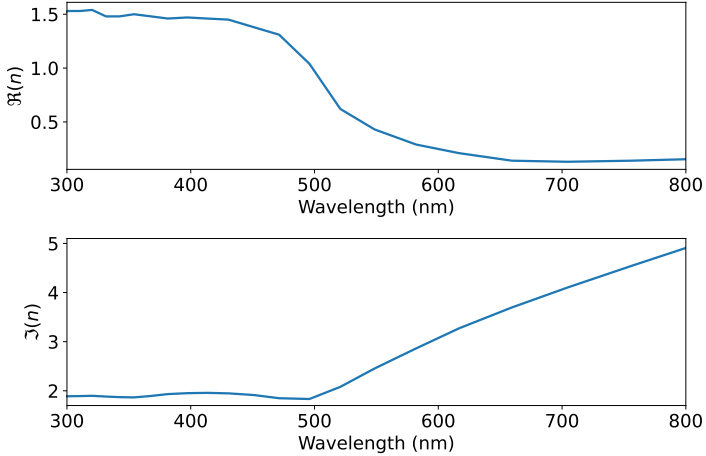


Figure 2.3: Real and imaginary part of the refractive index of gold measured by Johnson and Christy [53].

Gold films support surface plasmon polaritons (SPP). These are resonant charge density oscillations that travel along the metal-dielectric interface. Solving Maxwell's equations for such a system yields the dispersion relation [1, p. 26]:

$$k' = k_0 \sqrt{\frac{\epsilon_1 \epsilon_2}{\epsilon_1 + \epsilon_2}} \quad (2.9)$$

As shown in Fig. 2.4, the SPP dispersion relation exhibits an additional lower branch as compared to bulk plasmons. The lower polariton branch has a light-like character for low wavevectors and then tends towards the resonance fre-

quency of SPPs (ω_{SPP}). Between ω_{SPP} and ω_p the plasmon dispersion is purely imaginary and thus no electromagnetic waves are supported at that wavelength range. All light in that frequency range is reflected by the material [51]. Similar to bulk plasmons, SPPs are purely longitudinal oscillations and therefore not excitable by visible light without further aid by e.g. gratings [1, ch. 3]. This is apparent in the dispersion relation as there is always a momentum mismatch between surface plasmon polariton and photons.

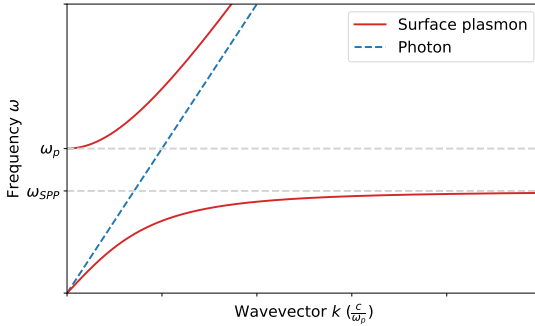


Figure 2.4: Dispersion relation of surface plasmon polaritons.

2.1.2 Localized surface plasmon resonance

Metal nanoparticles such as AuNP exhibit a localized surface plasmon resonance. These are collective oscillations of surface electrons against the positively charged lattice of gold atoms. In contrast to SPPs, these oscillations do not travel along the surface, i.e. they are localized.

Most commonly, the description of LSPRs is focused on the particle size range that the quasi-static approximation is valid in: For particles with diameter much smaller than the wavelength of the electric field ($d \ll \lambda$) the phase of the electric field is constant throughout the particle. By calculating the electric potentials in- and outside of an isotropic sphere with radius a described by its complex dielectric function ϵ and embedded in a non-absorbing medium with ϵ_m one arrives at an expression for the polarizability α [1, ch. 5]:

$$\alpha = 4\pi a^3 \frac{\epsilon - \epsilon_m}{\epsilon + 2\epsilon_m}. \quad (2.10)$$

Hence, the polarizability is enhanced resonantly if $\epsilon = -2\epsilon_m$, which is called the "Fröhlich condition". For a metal sphere in air, this condition is met at $\omega = \frac{\omega_p}{\sqrt{3}}$ and for gold particles with $5 \text{ nm} < a < 100 \text{ nm}$ the resonance is in the visible wavelength range [1, 4].

From the polarizability, the cross sections for scattering and absorption can be calculated:

$$C_{sca} = \frac{k^4}{6\pi} |\alpha|^2 = \frac{8\pi}{3} k^4 a^6 \left| \frac{\epsilon - \epsilon_m}{\epsilon + 2\epsilon_m} \right|^2 \quad (2.11a)$$

$$C_{abs} = k \text{Im}\{\alpha\} = 4\pi k a^3 \text{Im}\left\{ \frac{\epsilon - \epsilon_m}{\epsilon + 2\epsilon_m} \right\} \quad (2.11b)$$

with $k = 2\pi/\lambda$. These cross-sections can also be obtained from Mie-theory, which is an analytical solution of Maxwell's equations and therefore valid in more broader terms and not only in the quasi-static regime. According to Mie-theory, the frequency of the LSPR maximum can be expressed as [1, 7]:

$$\omega_{max} = \frac{\omega_p}{\sqrt{1 + 2\epsilon_m}} \quad (2.12)$$

In contrast to bulk plasmons and SPPs, an electric field can couple directly to the LSPR. Hence, AuNP exhibit a resonant absorption and scattering feature in the visible spectrum as shown in Fig. 2.5, giving a dispersion of AuNPs its distinct rubin-red color. To the lower-wavelength side the LSPR overlaps with interband transitions from the 5p to 6sp band [4].

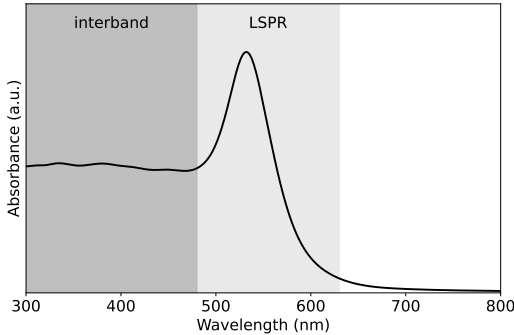


Figure 2.5: Simulated absorbance spectrum of a 40 nm AuNP.

Influences on the LSPR

Equations 2.10-2.11 as well as the Fröhlich condition already indicate the dependence of the LSPR on the surrounding medium and particle size. Below

30 nm, the particle size becomes smaller than the mean free path of the electrons, leading to additional surface scattering and damping of the LSPR [4, 9]. This effect is theoretically accounted for by an additional term to the damping constant:

$$\gamma(L) = \gamma_{bulk} + A \frac{v_F}{a} \quad (2.13)$$

with a material constant A , the Fermi-velocity v_F and particle radius a . For larger particles, the LSPR depends on the ratio of absorption- and scattering cross sections. Figure 2.6 shows these for 20 nm, 40 nm and 60 nm AuNPs as simulated using Mie theory. Because the absorption scales with a^3 while scattering scales with a^6 , absorption will dominate the overall extinction of small particles up to around 50 nm with scattering contributing more and more to the extinction with increasing size. For even bigger nanoparticles, the quasi-static approximation is no longer valid and multipolar plasmon oscillations become more important, resulting in a red-shift and broadening of the LSPR [4, 9].

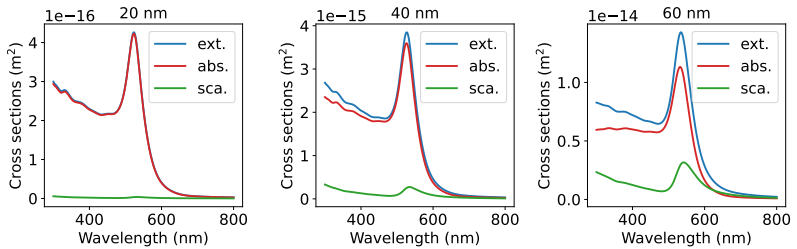


Figure 2.6: Extinction, absorption and scattering cross sections of differently sized AuNP in water calculated using the Mie-theory package PyMieScatt [54, 55]

The second major factor influencing the LSPR is the surrounding medium of the AuNPs. This contains the (usually non-absorbing) dispersion medium and

ligands that stabilize the particles in that medium. As predicted by the Fröhlich condition, an increase in dielectric function - e.g. going from air to water - will cause a red shift of the LSPR. To account for ligands on the particle surface and in solution, an effective dielectric function can be calculated using mixing rules [56]. Additionally, ligands will affect the LSPR by providing additional relaxation pathways for excited charge carriers and thereby cause chemical interface damping [57, 58]. Apart from non-absorbing media, AuNP can also be incorporated and/or combined with optically active materials, which leads to effects such as LSPR quenching or plasmon-exciton coupling [4]. The sensitivity of the LSPR to the immediate surrounding is one of the major effects utilized in plasmonic applications such as surface enhanced Raman scattering (SERS) [40].

The last noteworthy effect on the LSPR is temperature. As mentioned above, the LSPR frequency depends on the plasma frequency:

$$\omega_p(T) = \sqrt{\frac{e^2 n_e(T)}{m_{eff} \epsilon_0}}. \quad (2.14)$$

with the electron charge e , effective electron mass m_{eff} , the vacuum dielectric constant ϵ_0 and - most importantly in this case - the electron density $n_e(T)$. Thermal expansion of the particles with increasing temperature will lead to a decreasing electron density, which will in turn lead to a red-shift of the LSPR [4]. Additionally, through the temperature-dependent dielectric constant, the linewidth of the plasmon resonance increases with the temperature associated with the Fermi-distributed electrons [59, 60]. Figure 2.7 displays the absorption cross section of 30 nm AuNP calculated from Mie Theory for different temperatures. The temperature-dependent dielectric constant was taken from [22].

Plasmon dynamics

The main topic that this thesis is discussing is the dynamics of highly excited charge carriers in plasmonic AuNP. One excitation mechanism of these hot carriers is the coupling of the LSPR to electron-hole pairs. Generally, the damping of the LSPR is categorized into *radiative* and *non-radiative*. The non-radiative processes in turn are distinguished between scattering and collision-less processes [1, 14]. The refractive index of a plasmonic material introduced in equation 2.4 can be expressed as follows:

$$\epsilon(\omega) = 1 - \frac{\omega_p^2}{\omega^2 + i\gamma\omega - \beta k^2}. \quad (2.15)$$

γ expresses a scattering-related damping parameter that is comprised of e-e scattering, e-ph scattering, scattering on defects, scattering on surfaces etc. These scattering processes depend on material- and other physical parameters. For example, e-ph coupling usually increases with temperature and electron-surface scattering increases with the surface-to-volume ratio of nanoparticles [13, 61].

The β -term expresses Landau damping, which is a collision-less process by which single electrons gain energy from the LSPR as they are accelerated due to the phase-velocity relationship between a single electron and plasmon. Landau damping is considered to be the dominant damping mechanism of the LSPR in small nanoparticles as it scales with confinement [14].

Both of these damping mechanisms lead to the broadening of the plasmon resonance. Hence, the bandwidth of a LSPR observed in optical spectra is used to calculate the plasmon lifetime, which is usually in the low femtosecond range [62]. Because of this very short timescale, time-resolved measurements of the LSPR lifetime are challenging. However, the development of attosecond laser sources and newly developed E-field sampling techniques might enable a direct experimental access to the plasmon dephasing in the near future [63].

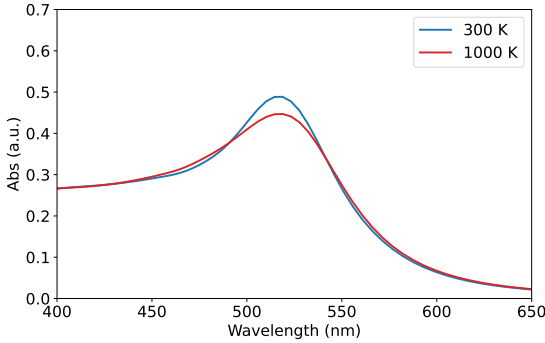


Figure 2.7: Absorbance spectra calculated using PyMieScatt for two temperatures 300 K and 1000 K. The particle size was set to 30 nm and dielectric functions for gold were obtained from the data provided by Brown et al. in Ref. [22]. n_{medium} was set to 1.33 for water.

2.2 Hot carrier dynamics in gold nanoparticles

2.2.1 Overview

The dynamics of charge carriers following the excitation of plasmonic materials is commonly described as a 4-step process (cf. Fig. 2.8): First, the plasmon dephases and Landau damping leads to the excitation of highly excited non-thermal electrons. Through e-e scattering these carriers exchange energy to form a "hot" Fermi distribution. Next the electrons relax via e-ph coupling. The last step is the energy transfer from the metal to the surrounding medium [13].

In principle, these processes can occur simultaneously. However, their timescales differ in orders of magnitude: Plasmon dephasing is the fastest process - only taking a few femtoseconds, which makes a direct observation of this effect

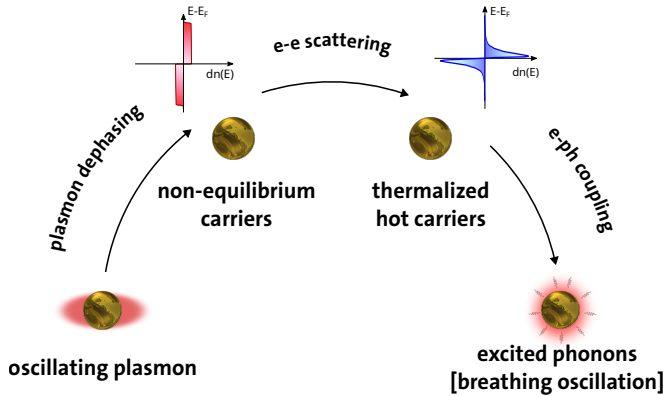


Figure 2.8: Overview of the hot electron dynamics in AuNP. The classic understanding of hot electron dynamics consisting of plasmon dephasing, e-e scattering and e-ph coupling (ph-ph coupling to the surroundings is omitted).

challenging. e-e scattering is a sub-picosecond process as well [18, 64, 65], while e-ph coupling occurs on a low picosecond timescale [18–21, 23, 24, 32, 66–68]. Lastly, depending on the material, the heat transfer from the particles to the surroundings is in the 100-1000’s ps range [13, 69–71].

Since hot charge carriers are thought to be useful for a range of applications, their dynamics have attracted much interest in the research community, especially since the development of tabletop solutions for femtosecond laser pulse generation in the late 1980’s and early 1990’s led to broad access to the timescales under investigation by optical means. In particular e-ph coupling is studied intensely to this day and the focus of this work as well.

2.2.2 Electron-electron scattering

Before we turn our attention to e-ph coupling - the main mechanism studied in this work - we must first arrive at an excited hot-electron distribution. As mentioned above the decay of the LSPR and direct interband transitions lead to the excitation of hot electrons. Within a short amount of time these electrons are not distributed according to a Fermi-Dirac statistics and are therefore termed "non-thermal". Because of the short lifetime of a few hundred femtoseconds, the initial non-thermal electron distribution is hard to assess experimentally. Experimental studies typically use either electron transport through barriers and molecules or time-resolved photoemission from thin films. Recent examples are the work of Reddy et al. who have used the energy-sensitive molecular orbitals of adsorbates for electron tunneling and Hartelt et al. who have used time-resolved photoemission electron microscopy [72,73]. However, the non-thermal electron distribution in AuNP could not be successfully resolved yet. Our current understanding of the non-thermal electron distribution in AuNP is therefore based on theoretical calculations. These show a wavelength dependent generation of hot charge carriers: Above the interband threshold of 2.3 eV, direct transitions lead to much higher excited holes than electrons. Below the interband threshold electrons and holes are created equally. Because of the required momentum transfer, this process is less intense than the direct excitation of hot carriers [61, 74].

Electron-electron scattering will lead to a redistribution of energy among electrons, eventually resulting in a "hot" Fermi-Dirac distribution of electrons. Theoretical studies of this process usually describe this process by applying Fermi's golden rule. Generally, the e-e scattering rate is proportional to the square of the energy difference between electron and Fermi-energy. Furthermore, the increase in temperature of the final hot electron distribution ΔT_e can be calculated by

$$\Delta T_e = \sqrt{T_0^2 + \frac{U}{\gamma}} - T_0 \quad (2.16)$$

where U is the absorbed energy, T_0 is the ambient temperature and γ is the electronic heat capacity coefficient [21]. This temperature increase is also accounted for by adding respective terms to the 2TM that is commonly used to describe the electron dynamics following plasmon decay. This model will be described in detail in the next chapter. The basic principle is describing the energy transfer from electrons to lattice vibrations as a heat transfer from electrons to phonons and e-e scattering is introduced into these equations by different extensions [16, 75, 76].

The rise time of the signal in transient optical pump-probe spectroscopy is sensitive to this process, because the TA signal depends on the temperature of the thermalized electron distribution, while non-thermalized electrons do not contribute to the signal. This allows to study e-e scattering depending on different parameters and e-e scattering times of roughly 400 fs to 500 fs are determined. Under 10 nm particle size the rise time decreases towards smaller particles while it remains roughly the same above 10 nm [18, 65]. Earlier studies on Au thin films by Sun et al. have found similar times, indicating bulk-like behavior for AuNP above 10 nm [64].

2.2.3 Electron-phonon coupling

In classical electrodynamics e-ph coupling was first introduced to explain the temperature-dependence of electric internal resistance of a metal. The average time between e-ph scattering events is inverse proportional to the resistance and an increase in temperature, i.e. in the kinetic energy of an electron, will lead to a lower coupling time and increased resistance. In semiconductors, e-ph coupling is responsible for the relaxation of an electron-hole pair to the bandgap, which explains the energy difference between absorbed and emitted photons. In the context of BCS theory of superconductors, e-ph coupling is responsible for the creation of Cooper pairs in metals at very low temperatures [77].

Generally, e-ph coupling is a process by which electrons and phonons exchange energy through Coulomb interactions. The electron's wavevector increases or decreases by annihilating or creating a phonon, respectively. Because the phonon energy is much lower than the Fermi-energy, electrons don't gain or lose a significant amount of their energy in a single scattering event. Hence, only electrons near the Fermi-level participate in e-ph coupling. This is also why the energy transfer from electrons to lattice vibrations is slower than the e-e interactions that lead to plasmon dephasing or energy redistribution within the electronic system.

In this work, two theories of e-ph coupling will be discussed and experimentally examined: the 2TM and a microscopic theory for describing the excitation of *breathing oscillations*, i.e. the coupling of electrons to coherent acoustic phonon modes that lead to an oscillation of the nanoparticle size. Additionally, a variety of approaches have been used to theoretically model e-ph coupling in gold, such as density functional theory [78, 79], Monte Carlo simulations [80], or time-dependent Boltzmann equation formalisms [23, 81].

Two-temperature model

In the context of e-ph coupling in metals, the 2TM was first used by Anisimov et al. in 1974 to describe electron emission from a laser heated metal [43]. The model expresses the energy of the electron and phonon distribution in terms of their respective temperatures $T_{e,L}$ and heat capacities $C_{e,L}$. The energy transfer between the distributions due to e-ph coupling is then basically described as a heat exchange between the two "heat baths", with a material specific e-ph coupling constant g governing the rate of heat exchange: $\partial E_e / \partial t = -g(T_e - T_L)$, $\partial E_L / \partial t = g(T_e - T_L)$ [32]. This results in a set of coupled differential equations describing the change in temperature of the electron and phonon distributions over time, respectively [43]:

$$C_e(T_e) \frac{\partial T_e}{\partial t} = -g(T_e - T_L) + \chi \Delta T_e + f(r, t), \quad (2.17)$$

$$C_L(T_L) \frac{\partial T_L}{\partial t} = g(T_e - T_L) \quad (2.18)$$

Equation 2.17 contains two additional terms: $\chi \Delta T_e$ describes the redistribution of energy within the electronic system and $f(r, t)$ the optical excitation of the electrons. If only e-ph coupling between an excited Fermi-distribution of hot electrons with known temperature and the lattice vibrations is considered, these two terms can be omitted. Due to the aforementioned differences in time scales between excitation of electrons, e-e scattering and e-ph coupling, the 2TM has been widely accepted as a good representation of the energy transfer from electrons to phonons [13]. Later works only either extended the 2TM or sought to understand details of the coupling constant g . For example, O’Keefe et al. have proposed a three-temperature model and an extended 2TM in order to explain e-e scattering and the related shift of the LSPR frequency observable in femtosecond optical spectroscopy shortly after plasmon desphasing [16]. However, the basic framework of the 2TM has been used like this for the last 30 years of research in this area [16, 18, 20, 21, 24, 32, 66, 67, 82, 83].

The main prediction of the 2TM is a rather obvious one: The time it takes for the electron and phonon subsystems to equilibrate depends on the temperature difference ($T_e - T_L$) between them. Thus, the more energy is deposited into the electronic system, the longer it will take for electrons and lattice to reach an equilibrium temperature (c.f. Fig. 2.9). Additionally, the electron temperature after excitation is much higher than this equilibrium due to the differences in heat capacity. The electronic heat capacity is given by the product of the heat capacity coefficient γ_e and the electronic temperature T_e : $C_e(T_e) = \gamma T_e$, with $\gamma = 61.76 \text{ Jm}^{-3}\text{K}^{-2}$ [77]. This linear relation holds true for electron temperatures up to about 3500 K [61]. The phonon heat capacity is a material constant for temperatures above the Debye-temperature (Θ_D) and decreases for lower temperatures. For gold $C_L = 25.418 \text{ J/molK}$ [84] and $\Theta_D = 170 \text{ K}$ [77].

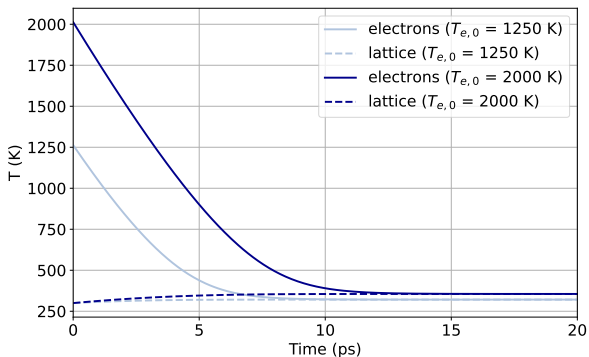


Figure 2.9: Electron and lattice temperatures in a 20 nm AuNP after excitation to two electronic temperatures $T_{e,0}$ according to the 2TM. g was set to $2.0 \times 10^{16} \text{ W m}^{-3} \text{ K}^{-1}$.

2.2.4 Parameter studies on electron-phonon coupling in AuNP

This section seeks to give an overview of the basic dependencies of e-ph coupling on the excitation conditions (wavelength and power) and sample parameters (size, crystallinity, ligands and composition). There are many more contexts in which e-ph coupling in AuNP is investigated. For a broad overview, the reader is referred to the excellent 2011 review by G. Hartland [13]. Some of the parameters that influence e-ph coupling are part of the studies presented in the rest of this thesis, such as the excitation of breathing modes, temperature-dependent coupling, or hot electron dynamics in hybrid systems for photocatalysis, and the respective theory is presented in those chapters.

Excitation wavelength and power

The 2TM predicts that the relaxation time of the hot electron distribution is dependent on the temperature difference between electrons and phonons. The initial temperature difference is given in Eq. 2.16 and depends on the absorbed energy U and ambient temperature T_0 . The absorbed energy in turn can be calculated via the absorbance or absorption cross section of the AuNP, which are functions of the photon energy (cf. Fig. 2.5-2.6), and the photon fluence per unit volume of gold:

$$U = \frac{I_{abs}}{N_{AuNP}V_{AuNP}} \quad (2.19)$$

The excitation wavelength dependence of the e-ph coupling time has been shown for AuNP of different sizes by Minutella et al. [68]. Two regimes have been identified: For a given photon flux, direct interband transitions lead to longer e-ph coupling times than intraband transitions. Around the resonant wavelength of the LSPR, the times seem to be longer as well. The same holds true for the e-ph coupling time as a function of the excitation fluence. Theoretical predictions of the coupling strength by Brown et al. in the same year confirmed the distinction between inter- and intraband regimes [85]. The linear power dependency of the e-ph coupling time has been shown by G. Hartland via time-resolved spectroscopy [32] and the slope of that linear relationship depends on the e-ph coupling constant g and the electronic heat capacity coefficient γ via

$$\tau_{e-ph} = \frac{\gamma}{g} T_{el}^{init.} = \frac{\gamma}{g} (\Delta T_{el}^{init.} + T_0). \quad (2.20)$$

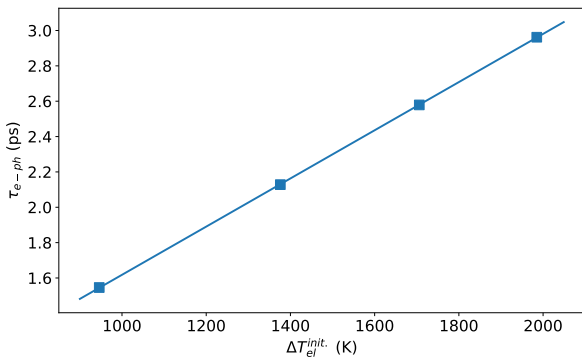


Figure 2.10: Typical e-ph coupling time vs. ΔT_{el}^{init} for AuNP.

Size and crystallinity

The following subsection presents a study I have been involved with in the conceptual design as well as first experiments together with one of our students Kai-Fu-Wong. The main body of work has been performed by my colleague Yannic Stächel. The study has been published here:

ACS Photonics, 2021, 8 (3), 752-757

A lot of research has been directed at the e-ph coupling constant and its dependence on various material and environmental parameters. For example, the particle size dependence of the coupling constant has been a matter of discussion for quite a long time. Previous experimental work - mainly performed via transient optical spectroscopy - both indicated the absence of any size dependence [18, 68, 86] while others have found an increasing coupling constant roughly below 10 nm [20, 83] supported by theoretical calculations by Saavedra et al. and Brown et al. [61, 87]. In theory, a size dependency of the e-ph coupling constant could result from the increase in scattering of the electrons at the particle surface with increasing surface-to-volume ratio of

small nanoparticles - in particular if the particle size becomes smaller than the mean free path of the electrons (ca. 50 nm [22]).

Another important material parameter to consider is the particle crystallinity: Internal grain boundaries or other defects should have the same effect as the particle surface - suggesting a crystallinity dependence of the e-ph coupling constant. This is supported by a number of experimental studies, which have found the e-ph coupling constant to increase for polycrystalline films compared to monocrystalline ones [66, 82, 88].

Studying the dependence of the physical properties on any material parameter requires a good control of such parameter in sample preparation. Because the synthesis of AuNP has been further developed parallel to the particle size studies mentioned above, it can be assumed that these were performed on polycrystalline particles. Since then, Zheng et al. have improved the synthesis routine to produce highly crystalline AuNP of different sizes [27] (the routine will be described in detail in chapter 3).

To disentangle the effects of particle size and crystallinity on the e-ph coupling constant, two sets of AuNP with different sizes were prepared: One synthesis route led to polycrystalline AuNPs and the other to monocrystalline particles. The crystallinity and sizes were assessed using transmission electron microscopy (TEM), x-ray diffraction (XRD) and UV-Vis spectroscopy (cf. Fig 2.11).

In order to obtain the coupling constant, TA measurements were performed. The exact methodology will be explained in detail in chapter 3. To summarize: For a given sample and excitation condition (photon energy and fluence), a decay of the TA signal is measured as a function of delay between pump and probe. For AuNP this decay is biexponential. The initial, fast decay is attributed to e-ph coupling [13]. Relating the according decay time to initial temperature of the hot electron distribution after e-e scattering for different $\Delta T_{el}^{init.}$ according to Eq. 2.20 determines the e-ph coupling constant g of a given sample.

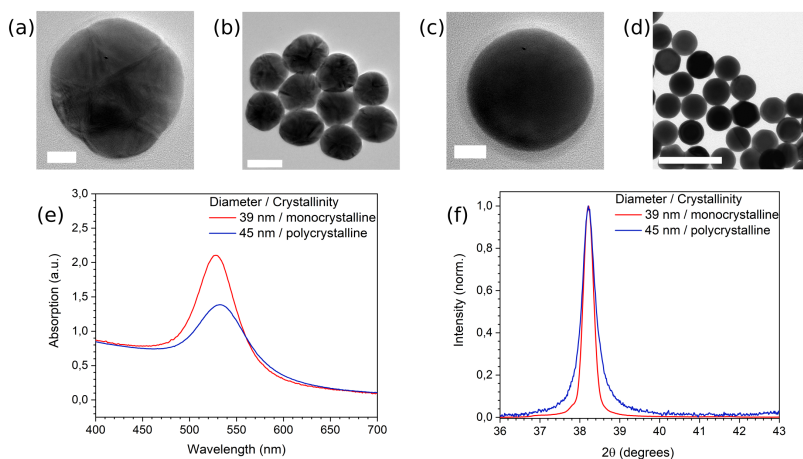


Figure 2.11: **a-d)** representative TEM images of 45 nm and 39 nm AuNP, respectively. **c)** UV-Vis spectra of the samples shown in a)-d). **d)** X-ray Bragg peak in the (111) direction of the samples shown in a)-d). Reprinted with permission from [24]. Copyright 2021 American Chemical Society.

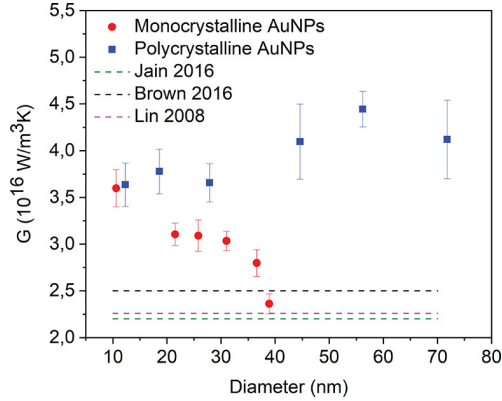


Figure 2.12: Electron-phonon coupling constant vs. particle size for mono- and polycrystalline AuNP. Dashed lines indicate bulk values of the e-ph coupling constant reported in [61, 67, 89]. Reprinted with permission from [24]. Copyright 2021 American Chemical Society.

This procedure was repeated for both sets of AuNP, yielding the coupling constant as a function of particle size for mono- and polycrystalline samples. The results are displayed in Fig. 2.12. These show a clear difference in size-dependence for mono- and polycrystalline AuNP: Polycrystalline particles do not show any size-dependent e-ph coupling. The coupling constant is around $3.6 \text{ W/m}^3\text{K}$ to $4.3 \text{ W/m}^3\text{K}$, whereas the monocrystalline particles exhibit a clear increase of g going from 40 nm to smaller particles. While the value for large particles is in the range of what has been determined for bulk gold [61, 67, 89], the value tends towards the same as for polycrystalline particles at 10 nm size.

The differences in g were attributed to the effect of grain boundaries as hypothesized above: For monocrystalline particles, surface scattering becomes a considerable factor in e-ph coupling around 30 nm to 40 nm , because the particle size becomes considerably smaller than the mean free path of the electrons. In polycrystalline particles, this size effect is compensated by scattering at in-

ternal grain boundaries. The mean crystallite sizes obtained from XRD via the Scherrer formula were 10 nm. For 10 nm particles, both synthesis routes resulted in monocrystalline particles and surface scattering becomes the dominant effect for the size-dependency.

Ligands and composition

Nanostructured materials exhibit special properties because of their increased surface-to-volume ratio. In the production of nanoparticles much attention needs to be allocated towards controlling the surface chemistry in order to produce homogeneous, high-quality structures. The wet-chemistry approach to synthesizing nanoparticles therefore utilizes ligands to control particle size and shape and prevent agglomeration. The surface passivation will also affect the physical properties of plasmonic nanoparticles. As mentioned in the LSPR theory section, the plasmon resonance is very sensitive to the dielectric function of the dispersion medium. Additionally, surface passivation will affect the hot electron dynamics as well. For example, Aruda et al. have used TA spectroscopy to compare e-ph coupling between 3.5 nm AuNP stabilized by thiol based and amine based ligands and have found a higher e-ph coupling constant for thiol stabilized AuNP. This effect was attributed to the alteration of electronic surface states by the covalent Au-sulfur bond [21]. A similar result was obtained by Foerster et al. who have studied chemical interface damping in Au nanorods of different sizes stabilized by thiol ligands compared to ethanol or cetyltrimethylammonium bromide (CTAB), which only physisorb to the surface [58]. In contrast, Guzelturk et al. have found a decreasing g upon changing the AuNP ligand from thiols (EDT and DDT) to oleylamine [83].

Moreover, the particle surface is frequently used to add new functionality to the pure core substance. One of the many promises of studying hot electron dynamics is the possibility for charge transfer to a semiconductor or other metal for photochemical reactions. There is an abundance of studies covering hybrid plasmonic systems and the reader is pointed to the review of Zhang et

al. for a comprehensive overview [90]. Generally, the transfer of hot electrons either follows a direct or indirect pathway. The direct route involves the excitation of electrons into excited states of the adjacent material, whereas the indirect route involves the excitation of electrons within the plasmonic material with a subsequent charge transfer across the interface. Recently, Tomko et al. have proposed an additional pathway of a "ballistic" energy transfer from hot electrons to conduction band electrons of a semiconductor [91]. In chapter 6, we support enhanced catalytic activity of Au-Pt hybrid superlattices by a time-resolved study of e-ph coupling. For reference, it has been shown that Au@Pt core-shell nanoparticles exhibit a faster decay of plasmon broadening, i.e. Au hot electron temperature, with increasing Pt amount. Here, e-e interactions between the thermalized hot electron distributions in Au and Pt occur faster than e-ph coupling in pure AuNP [92].

Chapter 3

Methods

3.1 Transient absorption spectroscopy

3.1.1 Introduction

Transient absorption spectroscopy is an experimental technique based on the pump-probe principle. Short laser pulses excite the sample (pump) and the absorbance of time-delayed pulses (probe) by the excited sample is measured. The absorbance in the excited state is referenced by the absorbance of the sample in its ground state. The resulting differential absorption map as a function of probe wavelength and delay time (see Fig. 3.2a) allows the investigation of excited charge carrier dynamics in optically active materials. The origin of the optical change varies depending on the type of material. For example, materials with discrete electronic transitions might show photoinduced absorption by enabling new excitation pathways and they show photoinduced bleaching of an absorption pathway due to Pauli blocking. AuNP show contrast in TA because of the LSPR's sensitivity to the electron temperature. As shown in

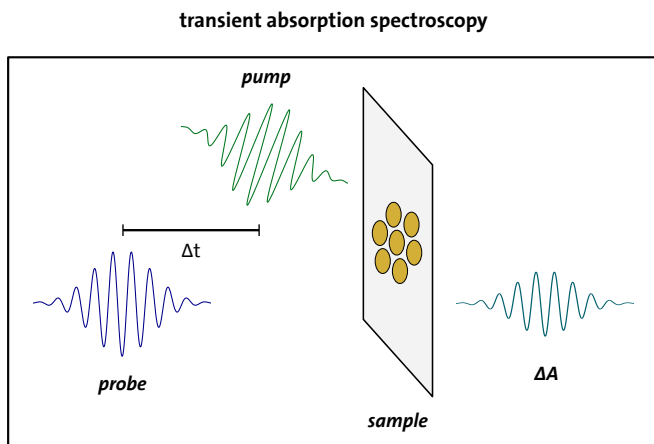


Figure 3.1: Schematic of transient absorption spectroscopy. An optical pump pulse excites the sample and the absorbance of a time-delayed probe pulse is determined. By referencing the absorbance in the excited state with the absorbance at ground state a differential absorption spectrum is determined per delay time. Scanning a delay time window allows to assess the dynamics of the differential absorption.

Fig. 3.2c-d, the LSPR bandwidth increases with temperature leading to the difference in absorption displayed there. Generally, the TA signal scales with the energy intake of the electron distribution. The absorbance characteristics of the sample thereby introduces a dependence of the signal on pump wavelength and power. Because the contrast will decrease with time (c.f. Fig. 3.2b), the relaxation dynamics of electrons in AuNP can be determined.

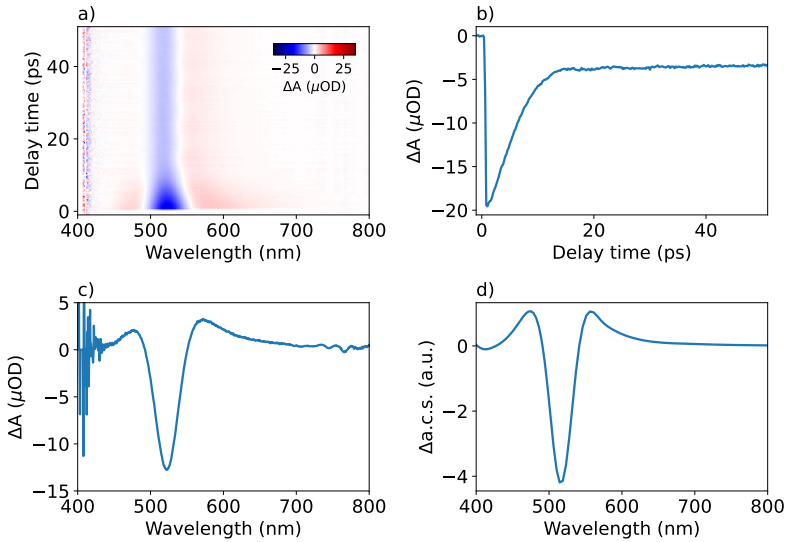


Figure 3.2: **a)** Typical TA map of an AuNP solution. **b)** Kinetic (ΔA vs. delay time) extracted at a probe wavelength of 525 nm. **c)** TA spectrum at a delay time of 1 ps. **d)** Difference of AuNP absorption cross section (a.c.s.) between 300 K and 1000 K from Fig. 2.7b.

Brown et al. have calculated the dielectric function of Au for electron temperatures between 300 K and 7000 K [22]. To support the commonly claimed linearity between the TA contrast and the electron temperature, these functions were used to calculate the extinction cross sections (Q_{ext}) of a 30 nm AuNP for

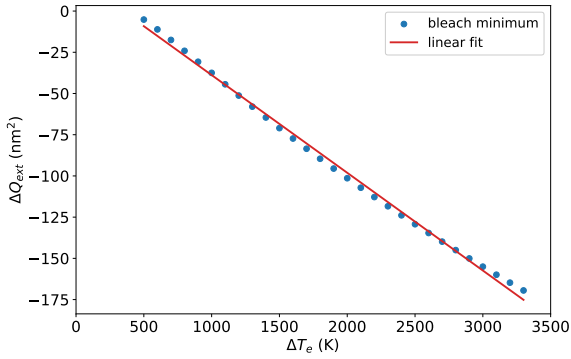


Figure 3.3: Minimum values of the difference in extinction cross section ΔQ_{ext} as a function of electron temperature differences ΔT_e .

the reported electron temperatures up to 3500 K using the Mie-solver PyMieScatt. Differential spectra of the extinction cross section (ΔQ_{ext}) were then calculated resulting in similar plots as displayed in Fig. 3.2d) for a given electron temperature difference (ΔT_e). The minimum value of the bleach feature is plotted against the electron temperature increase in Fig. 3.3. A linear regression of ΔQ_{ext} vs. ΔT_e confirms the common assumption, that the TA contrast is linearly dependent on the electron temperature increase with only minor deviations.

3.1.2 Technical Overview

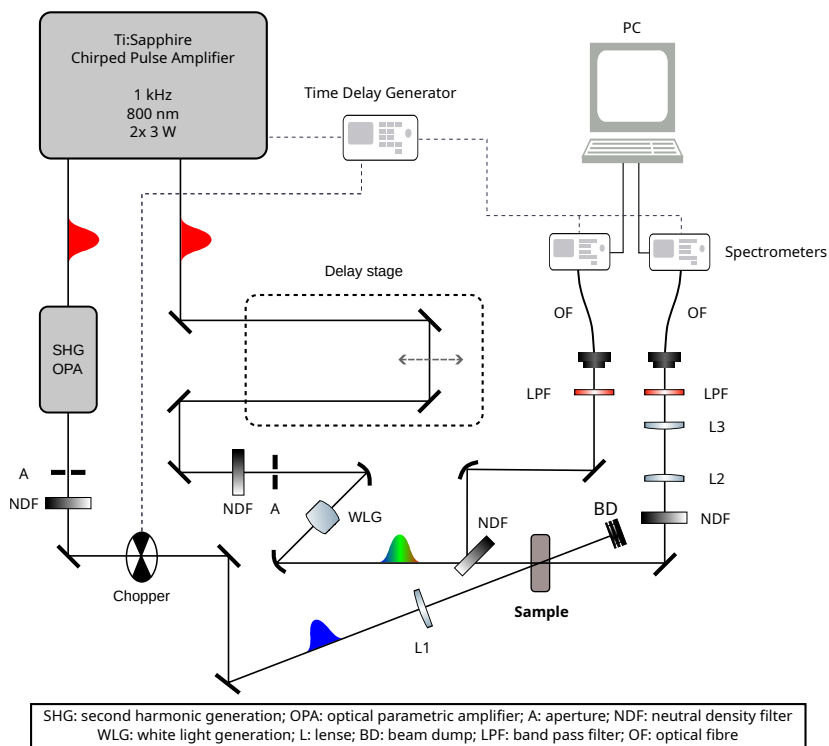


Figure 3.4: Schematic of the TA spectrometer used in this work.

The experimental TA setup used in throughout this work is a commercially available spectrometer (*Ultrafast Systems Helios*). Its layout is displayed in Fig. 3.4. The system is seeded by a pulsed laser system, a Ti:Sapphire mode locked laser with a 800 nm output (*Spectra Physics MaiTai*), which is then amplified by a regenerative, chirped pulse amplifier (*Spectra Physics Spitfire*, pumped by a *Spectra Physics Empower*) operating at 1 kHz. Its output

is split into two arms, which will serve as pump and probe, respectively. The wavelength of the pump pulses may be adjusted using frequency doubling in a barium borate (BBO) crystal or using optical parametric amplification (OPA, *Light Conversion TOPAS*) and their power is easily controlled using neutral density (ND) filters. A chopper wheel running at half the frequency of the laser system blocks every second pump pulse. The pulses are then focused onto the sample and dumped afterwards. The probe pulses are delayed with reference to the pump pulses using a motorized delay stage that increases the beam path. Then the 800 nm pulses are focused on a quartz or calcium fluoride crystal to produce a white-light continuum. For stable white-light generation (WLG), the power of the fundamental pulses must be carefully adjusted using an ND filter and aperture. The white-light pulses are focused on the sample ensuring a spatial overlap between pump and probe and the transmitted pulses are recorded by a spectrometer for a set range of delay times. The reflection of the white-light by a ND filter in front of the sample is recorded as well to correct intensity fluctuations in the white-light continuum (WLC).

Generation of femtosecond laser pulses

The measured signal in TA is a convolution of the sample response and an instrument response function (IRF), which is intrinsic to the experimental setup and usually limits the time-resolution. Therefore, TA requires laser pulses that are intense enough to produce a sufficient signal-to-noise ratio on the detector and short enough to resolve the physical processes in question. Laser pulses are routinely generated by mode-locked laser systems with various designs and output wavelengths. However, these pulses are usually not intense enough to drive the non-linear processes needed for manipulating the wavelength. In 2018, Gérard Mourou and Donna Strickland were awarded the Nobel prize in physics "for their method of generating high-intensity, ultra-short optical pulses" [30], which is *chirped-pulse amplification* [29]. To understand "chirp" let us quickly examine the form of laser pulses. In a frame moving with the laser pulse, these are expressed as a simple electromagnetic wave with an envelope multiplied with the amplitude:

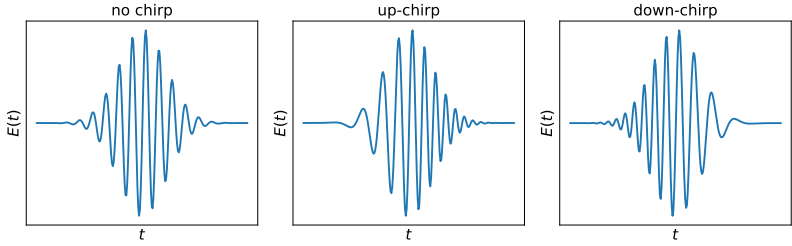


Figure 3.5: Illustration of chirped laser pulses in a frame moving with the pulse.

$$E(t) = E_0 e^{-\frac{t^2}{2\sigma^2}} \cos(\omega_0 t + \phi(t)) \quad (3.1)$$

Here, the envelope function has a Gaussian form. However, the envelope of real laser pulses might differ. Also note that the phase of the wave is generally time-dependent. Due to the time-bandwidth product $\Delta t \Delta \omega \geq \frac{1}{2}$, a very short laser pulse will contain more than one frequency and ω_0 in Eq. 3.1 is regarded as the center frequency [31].

While traveling through a medium other than vacuum, the phase velocity is determined by the speed of light and the refractive index of the medium, $v_{ph} = \frac{c_0}{n}$, while the group velocity, i.e. the velocity of the wave-packet envelope, is $v_{gr} = \frac{d\omega}{dk}$. A dispersion of the group velocity causes different speeds for the spectral components of the laser pulse and generally leads to a longer pulse duration. Normally, optical elements cause an "up-chirp" or positive chirp, i.e. lower frequencies travel faster through a medium than higher frequencies. However, by using either prism pairs or gratings, a "down-chirp" or negative chirp can be introduced (see Fig. 3.5).

Introducing positive and negative chirp is utilized in chirped-pulse amplification: First, a positive chirp is introduced that *stretches* the laser pulses, thereby lowering the peak intensity of the wave-packet before it is *amplified*. The

lowered peak intensity prevents damage to the gain medium of the amplifier, which limited the employable gain in the past. After amplification a negative chirp is introduced to *compress* the pulse back to its shortest duration of usually a few femtoseconds [29].

Manipulation of pump and probe wavelengths

The output of the laser system is modified utilizing non-linear optical effects. The processes used in this work were simple frequency doubling and OPA to control the pump beam wavelength and WLG for the probe beam. Two laser photons of the same frequency traveling through a material can turn into a single photon with a doubled frequency. This process is referred to as second-harmonic generation (SHG) and is an effect of the second-order electric susceptibility $\chi_{eff}^{(2)}$ of the material. The intensity of the second-harmonic radiation $I(2\omega)$ is further dependent on the incident intensity $I(\omega)$, the refractive index of the medium n , and the propagation distance through the material l :

$$I(2\omega) = \frac{2^7 \pi^3 \omega^2 \chi_{eff}^2 l^2}{n^3 c^2} I^2(\omega) \left(\frac{\sin \Delta k l / 2}{\Delta k l / 2} \right) \quad (3.2)$$

c is the speed of light and $\Delta k = k_2 - 2k_1$ is the dephasing quantity [31, pp. 39f.]. In order to maximize the intensity of SHG the *phase matching* condition must be satisfied, i.e. the fundamental (k_2) and second-harmonic radiation k_1 should interfere constructively. $\Delta k \rightarrow 0$ in this case. This is routinely achieved in birefringent materials, which have an ordinary and extraordinary refractive index for each frequency. At a certain crystal angle relative to $k_{1,2}$, where the refractive indices for fundamental and second-harmonic coincide, the phase matching condition is satisfied. This angle is therefore called the phase matching angle.

For the optical parametric generation of light (OPG), a photon with frequency ω_i and wavevector k_i incident on a birefringent material will produce two

photons with $\omega_{1,2}$ and $k_{1,2}$, conserving energy and momentum in the process: $\omega_i = \omega_1 + \omega_2$, $k_i = k_1 + k_2$. By adjusting the phase matching angle the outgoing frequencies are adjustable within a certain range. The higher frequency photon, produced in OPG is termed *signal* while the lower frequency photon is termed *idler*. Optical-parametric amplification of light (OPA) describes basically the same process, but with in an additional incident signal photon. In the setup used in this work (*Light Conversion TOPAS Prime*), the incident signal photon is produced using WLG prior to OPA. The probe pulses used for TA undergo a similar process in order to allow recording broadband spectra. WLG is a process based on several non-linear optical affects. Describing these in detail is beyond the scope of this work and the reader is referred to textbooks about non-linear optics [31, 93]. It should be noted, however, that WLG is very sensitive to the peak intensity of the incident pulses and therefore, the focusing, power and pulse length of the fundamental must be carefully adjusted.

Recording transient absorption spectra

With the wavelengths of the pump and probe pulses tuned to the required values, both beams are focused onto the same spot on the sample using simple spherical mirrors or lenses. Before the measurement, the spatial and temporal overlap between pump and probe pulses is ensured. By convention, the spot size of the pump beam is larger than the probe. This ensures that all the material probed by the WLC is excited, which is crucial for fluence-dependent measurements. The white-light transmitted through the sample is focused into an optical fiber that leads to the CMOS sensor of the spectrometer.

For the choice of pump power, several points need to be considered. The most obvious one is signal-to-noise ratio since a stronger excitation of the sample will lead to a bigger change in absorbance. Signal-to-noise ratio usually limits the pump power on the lower end. On the higher end, the intensity should not damage the sample or lead to significant structural changes. For example, the pump beam should not melt the AuNP or heat up the solution above the boil-

ing point. Additional limitations might be imposed by the physical properties of the material. For example, to relate the measured dynamics to the 2TM, the electron temperature should not be raised above ca. 3500 K, because the electron heat capacity becomes non-linear. All other parameters and settings are usually set to guarantee stability and good quality of the recorded signal. This usually includes an averaging time for each delay time and conducting multiple consecutive measurements for averaging as well to suppress noise. The proper delay time window and step size depend on the dynamics under investigation.

The result of a measurement is a ΔA map as a function of probe wavelength and delay time as shown in Fig. 3.2a. The data acquisition software automatically distinguishes between the recorded spectra of the excited (A_{exc}) and the unexcited sample (A_0), by synchronizing to a trigger signal sent out to the spectrometers and chopper wheel by the time delay generator of the laser system (c.f. Fig. 3.4). The two spectra are then subtracted to produce the differential absorption spectrum. The differential spectra are recorded for every step of the delay line. In contrast to steady-state UV-Vis spectroscopy no background correction spectrum (A_{inc}) is needed, if the probe pulses are stable:

$$A_{\text{exc},0} = \log_{10} \frac{I_{\text{inc}}}{I_{\text{exc},0}} \quad (3.3)$$

$$\Delta A = A_{\text{exc}} - A_0 = \log_{10} \frac{I_{\text{inc}}/I_{\text{exc}}}{I_{\text{inc}}/I_0} = \log_{10} \frac{I_0}{I_{\text{exc}}} \quad (3.4)$$

The commercial TA spectrometer used in this work underwent several upgrades, among which a reference channel for the white-light was installed. This provides an intensity reference for all the recorded spectra and the differential spectrum for a given delay becomes:

$$\Delta A = \log_{10} \left(\frac{I_0}{I_{\text{exc}}} \cdot \frac{I_{0,\text{ref}}}{I_{\text{exc,ref}}} \right) \quad (3.5)$$

Time resolution

The time resolution of the experiment depends on various factors, which include the pulse length at the laser output, the induced chirp by the optical elements that the pulses travel through until they eventually hit sample and detector, as well as other considerations regarding the experimental design such as the choice of detector or angle between pump and probe [94]. The pulse length at the laser output may be determined by autocorrelation measurements, while the time resolution in TA can be determined by analyzing the coherent artifact visible when pump and probe pulses convolve.

In this work, the pulse length of the laser output ($\lambda = 800$ nm) was monitored by recording the intensity autocorrelation. Autocorrelation measurements is an interferometric technique: The pulsed laser beam is split into two arms, which then overlap after one of the arms was directed through a variable delay stage. The overlap is measured either through two-photon absorption or SHG as a function of delay time. The employed commercial autocorrelator (MiniUSB, APE, Berlin) in this work was based on the latter. The measured signal is the second-order intensity autocorrelation function, which is fitted using a Gaussian or sech^2 function, as displayed in Fig. 3.6. Depending on the fit function different conversion factors need to be employed for calculating the pulse length (full width at half maximum, FWHM) Δt from the FWHM of the fit functions $\Delta\tau$: Gaussian: $\frac{\Delta\tau}{\Delta t} = 1.75$, sech^2 : $\frac{\Delta\tau}{\Delta t} = 1.54$ [31]. Usually, the laser system yielded a pulse length of ca. 35 fs (Gaussian fit). With the number of the following optical elements in mind, one can already assume a sub-ps time resolution from that.

In TA, another signal is commonly used to determine the time resolution: the "coherent artifact". The coherent artifact is a signal produced in the sample at the point of convolution between pump and probe. There are different sources for the artifact, which include two-photon absorption [95], stimulated Raman emission [96] and cross phase modulation [97]. Which of these effects dominate the artifact is dependent on various factors such as the employed wavelengths and type of sample, e.g. liquid in a cuvette or film on a glass sub-

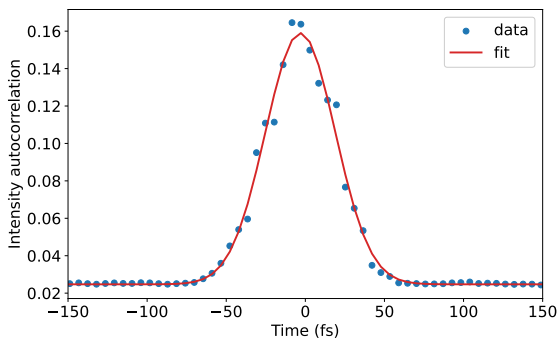


Figure 3.6: Example of an intensity autocorrelation measurement at the laser output. From the gaussian fit (red) a pulse length of 37 fs was determined.

strate [94]. Fig. 3.7a shows an exemplary artifact measured in a 2 mm glass cuvette filled with H_2O . The envelope of the absolute value of that artifact is then fitted with a Gaussian function, the FWHM of which is taken as the time-resolution of the experiment [98]. From the examples given in Fig. 3.7b) and c) for the two types of sample containers used in this work it can be concluded that the time resolution of the setup was ca. 100 fs, which is sufficient to analyze the few-ps dynamics measured throughout this work.

3.1.3 Data analysis

The first steps of analyzing TA spectra is correcting the measurement for chirp (c.f. Fig. 3.8) and subtracting the constant signal produced by scattering of the pump beam. The latter is only needed if the pump wavelength is within the range of the recorded WLC. For chirp correction, the first delay time showing contrast, time-zero, is manually selected at several (at least four) probe wavelengths. These points are then fitted with the function

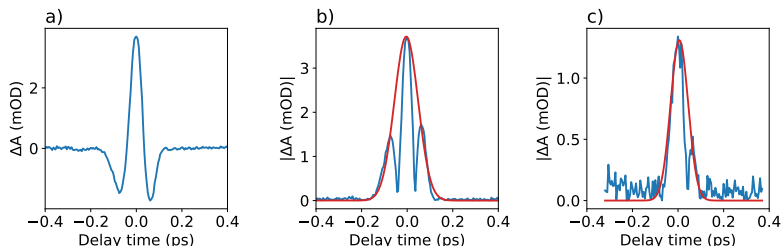


Figure 3.7: Analysis of the coherent artifact in TA to determine the time resolution. **a)** Coherent artifact measured in a 2 mm glass cuvette filled with H₂O, pump: 515 nm, probe: 550 nm. **b)** blue: absolute value of the coherent artifact shown in a). Red: Fit of the envelope of the absolute artifact. The FWHM of the Gaussian was 123 fs. **c)** Same as in b) but the artifact was measured in a glass slide mounted inside the cryostat used for temperature dependent TA in chapter 4. The determined FWHM of the gaussian fit was 91 fs.

$$t_0 = a \cdot \sqrt{\frac{b \cdot \lambda^2 - 1}{c \cdot \lambda^2 - 1}} + d \quad (3.6)$$

where t_0 is the delay time, λ is the probe wavelength and a, b, c, d are fit parameters. According to the resulting fit function, time-zero is then corrected for every probe wavelength.

Determining the e-ph coupling time

The main figure used to quantify e-ph coupling in AuNP using TA spectroscopy is the fast decay time of the signal (see Fig. 3.9). In particular, the decay of the signal is usually found to be biexponential, with the first, faster decay indicating the equilibration of the electron distribution and the lattice

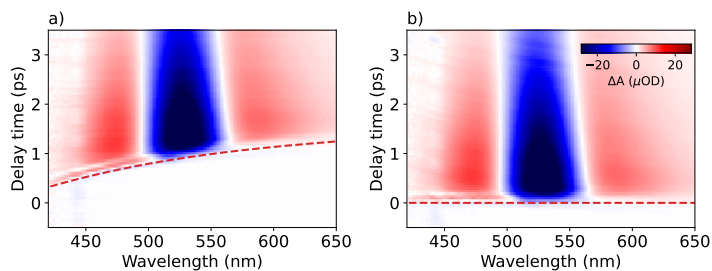


Figure 3.8: **a)** raw TA spectrum within the first picoseconds. The dotted line represents the fit of the wavelength-dependent time-zero. **b)** Corrected TA spectrum. For each wavelength, time-zero given by the fit function was set to $t = 0$ ps.

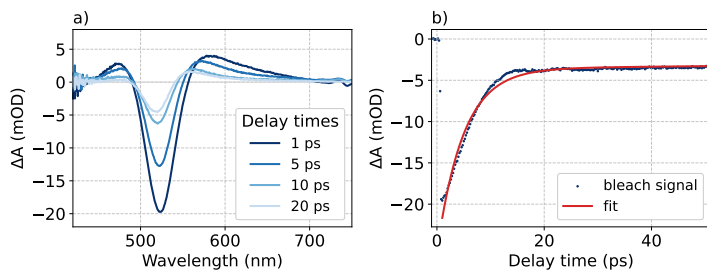


Figure 3.9: Data analysis of the bleach kinetic. **a)** TA spectra at increasing delay times. **b)** Bleach kinetic and fit function.

and the second, longer decay indicating phonon-phonon interactions with the environment, i.e. the cooling of the AuNP to the ambient temperature. Therefore, the decay is fitted using a biexponential function and the fast decay time is interpreted as the e-ph coupling time τ_{e-ph} .

$$\Delta A = a1 \cdot \exp\left(-\frac{t}{\tau_{e-ph}}\right) + a2 \cdot \exp\left(-\frac{t}{\tau_{ph-ph}}\right) \quad (3.7)$$

This function is sometimes multiplied with a heavyside function to include the rise of the signal. The rise - if it is determined to be longer than the IRF - is used to quantify e-e scattering, which is usually a faster process than e-ph coupling. Since e-e interactions were not the focus of this work and are ignored in the analysis of e-ph coupling, the heavyside function was omitted.

For precision, it is insufficient to analyze the decay kinetics at a single probe wavelength, because the signal is not only comprised of the LSPR broadening, but also a spectral shift of the resonance. Therefore, the minimum of the bleach component is determined for every delay time by fitting an inverted Gaussian or a polynomial function to the local minimum and taking the minimum value of that function as the ΔA value of that delay time. From there, the resulting kinetic is used to determine the e-ph coupling time.

Calculation of the e-ph coupling constant

As mentioned above, the change in absorbance by AuNP is the result of the increase in electron temperature upon excitation. Hence, the absorbed energy is a crucial parameter to interpret the e-ph time. Because of this power dependence, the e-ph coupling factor g is a better value to characterize a given material. Two strategies are commonly employed to determine the e-ph coupling constant. The first strategy is the excitation of the sample in a low perturbation regime. In that case, the electron temperature is only slightly increased by the pump ($\Delta T_e^{init.} \ll T_0$) and the general relationship between the coupling

time, the coupling constant and the electronic and ambient temperatures given in Eq. 2.20 would simplify to

$$\tau_{e-ph} = \frac{\gamma}{g} T_0. \quad (3.8)$$

The advantage of this strategy is the ability to determine g from a single measurement and the changes of the electron heat capacity with temperature can be ignored (although, they are still included in the equation above via the electron heat capacity coefficient, γ). However, in order to satisfy $\Delta T_e^{init.} \ll T_0$, the pump fluence has to be kept at a minimum and acquiring data with sufficient signal-to-noise becomes challenging.

Another strategy to reach this expression is measuring a series of kinetics with increasing excitation fluence and interpolating the determined e-ph coupling times to minimum power. This strategy allows more precise measurements, because the signal-to-noise ratio is much better. The drawback of this technique, however, is the uncertainty introduced by the linear regression of the obtained e-ph coupling times vs. power.

In this work, another method was chosen. Instead of trying to simplify Eq. 2.20, it is chosen as it is to determine g from a series of measurements at increasing excitation fluences. For that, the employed excitation fluence is translated to the increase in electron temperature. This has the advantage that instead of using the error prone intercept of the linear regression of τ_{e-ph} vs. P we use the more reliable slope of τ_{e-ph} vs. T_e . The only drawback of this technique is the uncertainty of the absorbed energy that is used to calculate the electron temperature. From experience, this uncertainty is lower than the standard deviation of the τ_{e-ph} vs. P intercept.

3.2 Sample preparation

The relationship between the size and shape of nanoparticles and the emerging chemical and physical properties is at the core of nanoscience. Additionally, collective effects of nanoparticle assemblies have gained significant attention in the scientific community as well. Therefore, techniques that allow precise control over size, shape and environment of nanostructures are under constant development. Even if this thesis deals with the physical properties of AuNP, the underlying principles of the nanoparticle preparation shall be briefly presented here - especially since all samples used in this work were synthesized in-house.

The basic principles of AuNP synthesis and assembly is the control of the nanoparticle surface. Gold atoms at the surface of a particle possess a higher chemical potential than their counterparts in bulk. Hence, without further manipulation AuNP would be unstable and agglomerate, because of their high surface-to-volume ratio [99]. The main strategy in a bottom-up, wet-chemical synthesis protocol is the surface passivation by adsorbed ligands [100]. There is a multitude of different suitable agents, ranging from lightly bonding citrate to covalently bonding thiolated polymers [8, 27]. The exact choice of ligand depends on the synthesis route, the size of the AuNP and the dispersion medium. For potential biomedical applications, further manipulation of the ligand shell is one of the main strategies under investigation in current research [101, 102].

3.2.1 Gold nanoparticle synthesis

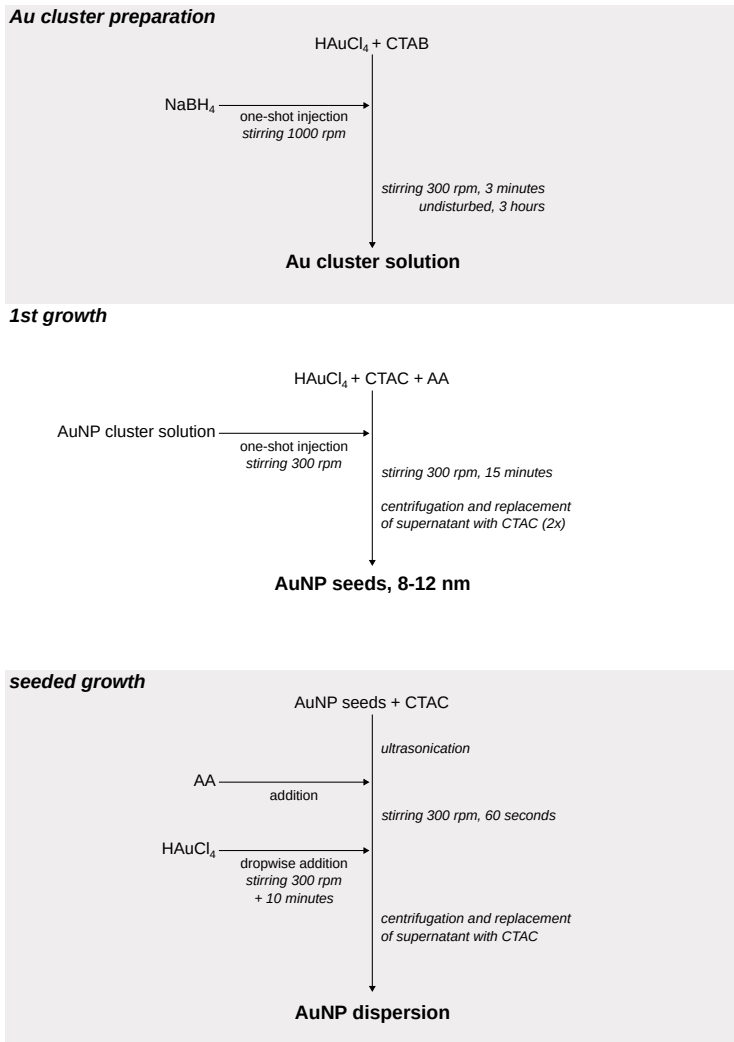
The synthesis of AuNP used in this study was introduced by Zheng et al. in 2013 [27] and slightly adapted to the needs of the experiments in this thesis and other studies in our group [12, 24]. An overview of the protocol is given in Fig. 3.10. It consists of at least two steps: The nucleation of Au clusters followed by the seed-mediated growth into AuNP in the size range of 5 nm to

12 nm. These AuNP can in turn function as seeds for additional growth steps, enabling the control of the AuNP size from 5 nm to 150 nm while producing highly spherical AuNP. In this work, AuNP between 20 nm to 40 nm were used as samples, hence two seed-mediated growth steps were applied. The protocol is "seed-mediated" since the relative quantities of Au clusters or seeds and Au precursor controls the size of the product.

In all stages, elemental Au is produced by reduction of tetrachloroauric acid (HAuCl₄) in an aqueous solution and cetyltrimethylammoniumbromide or -chloride (CTAB, CTAC) ligands stabilize the Au⁰ clusters or particles. The reactions take place under mild conditions: room temperature and atmospheric pressure. Slight heating to 30 °C helps for control of the temperature and reproducibility.

The first step of the protocol is the preparation of Au clusters. For that, HAuCl₄ is first mixed with the stabilizing ligand CTAB. Under rapid stirring the reductant sodium borohydride (NaBH₄) is added via one-shot injection. NaBH₄ is a strong reducing agent and its rapid addition ensures a low size distribution of the resulting Au clusters [103, 104]. Keeping the time window for nucleation as small as possible ("burst nucleation") is a common strategy in producing homogeneous nanoparticles. The solution is stirred for another 3 minutes to complete the growth of the Au clusters and is then kept undisturbed for 3 hours so excess NaBH₄ can react with water to form NaB(OH)₄ + H₂.

The CTAB stabilized Au clusters are only stable for a few hours and are therefore immediately used to grow larger, more stable AuNP in the first growth step: Here, HAuCl₄ is mixed with CTAC instead of CTAB and ascorbic acid (AA) as a weak reductant. Under stirring, the Au clusters are added to the solution via one-shot injection. Since gold has two common oxidation states, Au^{III} and Au^I, there is a chemical equilibrium in solution:
$$\text{Au}^{\text{III}} + 2 \text{Au}^0 \rightleftharpoons 3 \text{Au}^{\text{I}}$$
 with Au^I being most stable in solution. AA is used to reduce Au^{III} to Au^I and therefore avoid the oxidation of the Au⁰ clusters, by shifting this equilibrium. The added Au clusters then serve as catalysts for the reduction of Au^I to Au⁰. Hence, new elemental Au only forms on the surface of the clusters and not as new nuclei. Once again, the rapid injection of the clusters ensures homo-

**Figure 3.10:** AuNP seeded growth synthesis

geneous growth of the particles. After a reaction time of 15 minutes, stirring is stopped and the solution is washed by centrifugation and replacement of the supernatant with fresh CTAC solution. This first growth step results in CTAC-stabilized AuNP of roughly 10 nm, which can be used as seeds for further growth steps.

The following growth steps use the same ligand and reductant, but the small AuNP are used as seeds instead of the Au clusters. Another difference is the order and injection speed of the reactants. The AuNP-seeds are first thoroughly mixed with CTAC solution by ultrasonication. Then, AA is added and the solution is stirred for 60 seconds before the drop-wise addition of new Au precursor, HAuCl₄, starts. The size of the particles is controlled by the relative amounts of Au seeds to HAuCl₄. For the same amount of added HAuCl₄, more seeds lead to a smaller particle size. The shape of the resulting particles depends on three factors: the choice of ligand, the rate of atom deposition and surface diffusion on the particles. Using CTAC as ligand instead of CTAB favors the growth of spherical particles [28,100]. Additionally, HAuCl₄ is added slow and steady to the solution under stirring to guarantee a slow enough atom deposition rate for surface diffusion to shape the particles into spheres. After the addition of HAuCl₄ is completed and additional 10 minutes reaction time, the dispersion is washed by centrifugation and replacement of the supernatant with fresh CTAC solution. This process extracts Au precursor, which is has not yet reacted, and thereby stops the growth of the particles.

3.2.2 Quality assessment

UV-Vis spectroscopy

UV-Vis spectroscopy was used in this thesis to quickly assess the sample quality and to determine the particle concentration of a AuNP dispersion. According to the Lambert-Beer law the intensity of radiation transmitted through a sample I depends on the incident intensity I_0 , the path length through the

sample l , the molar concentration of the absorbing species c and the material-specific extinction coefficient ϵ [51]:

$$I = I_0 \cdot 10^{-\epsilon cl} \quad (3.9)$$

As presented in chapter 2, the LSPR is very sensitive towards the particle size, shape and environment. Generally, a red-shift and broadening of the LSPR indicates a deviation from an ensemble of individual, spherical AuNP. If the wavelength-dependent extinction coefficient is known, UV-Vis spectroscopy can be used to determine the concentration of Au in a solution. To obtain particle concentrations, two strategies are routinely used. For both protocols wavelengths corresponding to interband transitions are used. For AuNP sizes small enough to ignore scattering (cf. Fig. 2.6), Scarabelli et al. have determined an absorbance of 1.2 at 400 nm corresponds to 0.5 mM of elemental gold [28]. Accounting for the amount of gold in a single AuNP of a given size and shape determined by TEM yields the particle concentration. Thus, this method is suitable for non-spherical particles as well. Haiss et al. have reported extinction coefficients at 450 nm for spherical AuNP between 2 nm to 100 nm, which can be used to relate the measured absorbance at that wavelength to the particle concentration [105].

Unless otherwise specified, all UV-Vis measurements were conducted using a Varian Cary 50 spectrometer.

Transmission electron microscopy

Both methods for determining the particle concentration require the knowledge of the particle size and shape. While Haiss et al. also report a size determination based on the relative absorbance at the LSPR center wavelength to the absorbance at 450 nm, the method of Scarabelli et al. is fully reliant on the knowledge of the particle size and shape. Thus, the combination of UV-

Vis spectroscopy with TEM is the standard routine for characterizing newly synthesized AuNP.

Because of the Abbe-limit, the resolution of optical microscopy is too low to assess the AuNP size and shape. This resolution, however, is much higher if accelerated electrons are used instead of optical light (in the nm to pm range). Conventional electron microscopy is the recording of bright- or dark field images like in optical microscopy and electrons are absorbed or scatter of AuNP, leading to less intensity on the corresponding projection spot on the detector. This "mass-thickness" contrast increases with the atomic number. Hence, particle sizes of a "pure" AuNP, without its ligand shell can be determined [106]. Through image processing - performed in the software *imageJ* in this work - the AuNP images are analyzed to give the AuNP size distribution. For that, the images are converted into binary pictures and touching AuNP are artificially separated by a line, or deleted if the overlap is too big. For sufficiently spherical particles, the individual AuNP diameters are calculated from their circular areas in the image.

Unless otherwise specified, all TEM measurements shown in this work have been carried out using a Joel JEM-1011 Transmission electron-microscope operating at 100 kV. Prior, the nanoparticles were deposited on carbon coated copper grids and then dried either at air overnight, or in vacuum for 1 h.

Chapter 4

Temperature-dependent electron-phonon coupling

Despite its simplicity the two-temperature model serves as an excellent model to understand the e-ph dynamics in AuNP and it is therefore widely used for the interpretation of time-resolved experiments. One of the assumptions of the model is the coupling factor's independence on the electron and lattice temperatures. However, whether or not that is the case is debatable:

According to the classic e-ph coupling used to describe the temperature-dependent resistance of metals, one would expect the e-ph coupling constant to increase with T_e [77]. Mueller and Rethfeld calculated the e-ph coupling constant depending on the electron temperature of 2000 K and above. While the value is only slightly changing between 2000 K to 3500 K, it increases with higher T_e , indicating an almost constant g for the temperature range usually employed in optical pump probe studies [23]. These results are in line with recent experimental work on hybrid AuNP-semiconductor systems by Hattori et al. and Ghorai et al. [107, 108]. Their observations might indicate a difference in g 's

temperature dependence between Au films and AuNP. However, Hattoria et al. and Ghorai et al. focused on energy transfer between AuNP and semiconductors and the latter did not analyze g at all, but argued based on changes in τ_{e-ph} .

For laser-heated electrons in gold, several studies aimed at determining the ambient temperature dependence of e-ph coupling. Giri et al. performed time-domain thermorefectance on a Au film depending on the ambient temperature between 77 K to 300 K at two different excitation fluences. In the low fluence regime (0.1 J/m^2), the coupling factor was given by the product in equation 2.20, i.e. τ_{e-ph} is proportional to the ambient temperature and the e-ph coupling constant. At the higher fluence (3.52 J/m^2) the coupling factor g didn't change significantly for ambient temperatures above 100 K and slightly decreased below 100 K – reproducing the prediction from the 2TM, which included the temperature-dependence of the lattice heat capacity below the Debye temperature [109]. These results were in line with thermal transport measurements from Pt to Au by Wang and Cahill [110]: Their observations were interpreted by accounting for the role of non-thermal electrons in e-ph coupling. As mentioned in chapter 2, the e-e scattering rate scales with electron temperature. Hence, at low effective electron temperatures the non-thermal electrons contribute to e-ph to a larger extent, compared to high temperature electrons, which thermalize quickly. This interpretation is supported by theoretical work of Mueller and Rethfeld [23]. Furthermore, Zhou et al. have used time-dependent density functional theory and molecular dynamics simulations to calculate e-ph coupling constants and times in Au films [111]. They have found an increase in the e-ph relaxation time with increasing temperature from 100 K to 300 K and also an increase in g with temperature. However, they yield constants an order of magnitude higher than the previously mentioned studies.

Hence, for AuNP the question remains how the e-ph coupling constant depends on the environmental temperature, i.e. the temperature of the system at the start of the hot electron dynamics. In particular for temperatures below gold's Debye temperature of 170 K the decrease in phonon modes might affect e-ph coupling. Thus, the study presented in this chapter aims at systematically

exploring the dependency of g in AuNP on the environmental temperature at low temperatures ($100 \text{ K} \leq T_{env} \leq 350 \text{ K}$). For this study, e-ph coupling in a spin-coated film of AuNP was examined. The film was placed inside a cryostat that allows to control the environmental temperature down to the temperature of liquid nitrogen ($\approx 78 \text{ K}$). A series of power-dependent TA experiments ($50 \mu\text{J}/\text{cm}^2$ to $200 \mu\text{J}/\text{cm}^2$) were conducted for a temperature range between 100 K and 350 K . The e-ph coupling time was determined from the experiments and by comparing these results to the predictions made by the 2TM the temperature-dependence of the e-ph coupling factor was tested.

4.1 Two temperature model simulations

In order to predict the e-ph coupling time using the 2TM, three initial parameters are needed: the initial temperatures of the electron and lattice given by the environmental temperature T_{env} , the initial temperature increase of the electronic system, $\Delta T_{e,0}$ and the e-ph coupling constant g . e-e scattering will be ignored and the initial electron temperature was calculated as described in Eqs. 2.16 and 2.19. With that, the 2TM was implemented as:

$$\gamma_e T_e \frac{\partial T_e}{\partial t} = -g(T_e - T_L) \quad (4.1)$$

$$C_L \frac{\partial T_L}{\partial t} = g(T_e - T_L) \quad (4.2)$$

As mentioned previously, the change of the lattice and electron temperatures through e-ph coupling is governed by their respective heat capacities, C_e ; C_L . In the temperature range employed in this study the electronic heat capacity increases linearly with electron temperature according to $C_e = \gamma_e T_e$, with the electronic heat capacity coefficient $\gamma_e = 61.76 \text{ Jm}^{-3}\text{K}^{-2}$ [77]. The lattice heat capacity is described by the Debye model and is shown in Fig. 4.1 for gold. At low temperature - below the material specific Debye temperature -

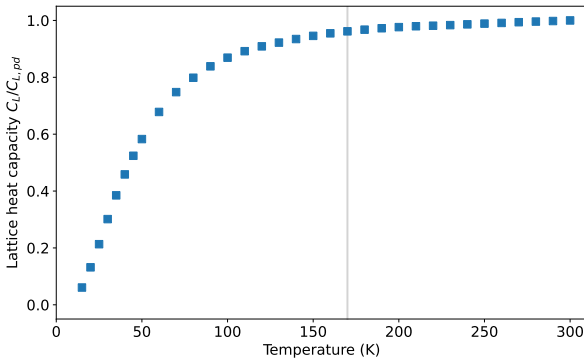


Figure 4.1: Lattice heat capacity normalized to the Dulong-Petit value ($C_{L,pd} = 2.4 \times 10^5 \text{ W/m}^3\text{K}$). The data were reported by Geballe & Giauque and converted to the units used in this study [112]. The grey line indicates gold's Debye temperature of 170 K.

the number of phonon modes and therefore the lattice heat capacity decreases. For temperatures above the Debye temperature, the lattice heat capacity approaches the limit described by the Dulong-Petit law [77].

For the environmental temperatures and electron-temperatures deployed in this study, one expects the change in lattice heat capacity to have the most effect at the lowest T_{env} of 100 K ($T_{L,0} < T_{\Theta}$) and highest $\Delta T_{e,0}$ of 2009 K, because that induces the biggest change in C_L throughout the measurement. Fig. 4.2 shows the calculated electron and lattice temperatures over time according to the 2TM for two cases: In one case, a constant lattice heat capacity was chosen according to the reported value at room temperature, i.e. the Dulong-Petit value. In the second case, the lattice heat capacity was treated as a function of lattice temperature. For that, data measured by Geballe & Giauque was taken and converted to similar units [112]. These data follow the behaviour according to the Debye model with minor deviations. The e-ph cou-

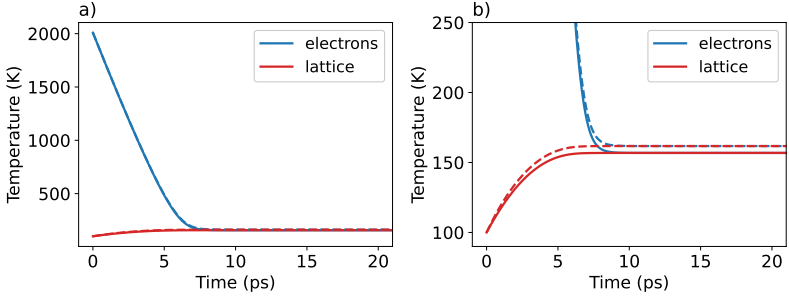


Figure 4.2: Electron and lattice temperatures calculated according to Eqs. 4.2. Solid lines: constant C_L ; dashed lines: interpolated C_L from values displayed in Fig. 4.1, g was taken from Ref. [24] for 27 nm AuNP.

pling constant was taken from an earlier study on 27 nm AuNP ($g = 2.4 \times 10^{16} \text{ W/m}^3\text{K}$, [24]).

For both temperatures, the differences between the two cases are very minor. Even without heat transfer to the environment implemented into the 2TM, the difference in equilibrium temperature is only 4.9 K (ΔT_L : 56.8 K vs. 61.7 K). Therefore, the expected differences in e-ph coupling time should be governed only by the temperature difference between electrons and lattice. From the 2TM, the e-ph coupling times were determined by fitting a single exponential decay to the electron temperature. They are displayed in the discussion section of this chapter (see Fig. 4.9).

4.2 Temperature-dependent transient absorption

The sample investigated in this study consisted of a AuNP film, which partially covers a borosilicate glass substrate. The AuNP were prepared using the synthesis route described in chapter 3, yielding highly uniform, spherical par-

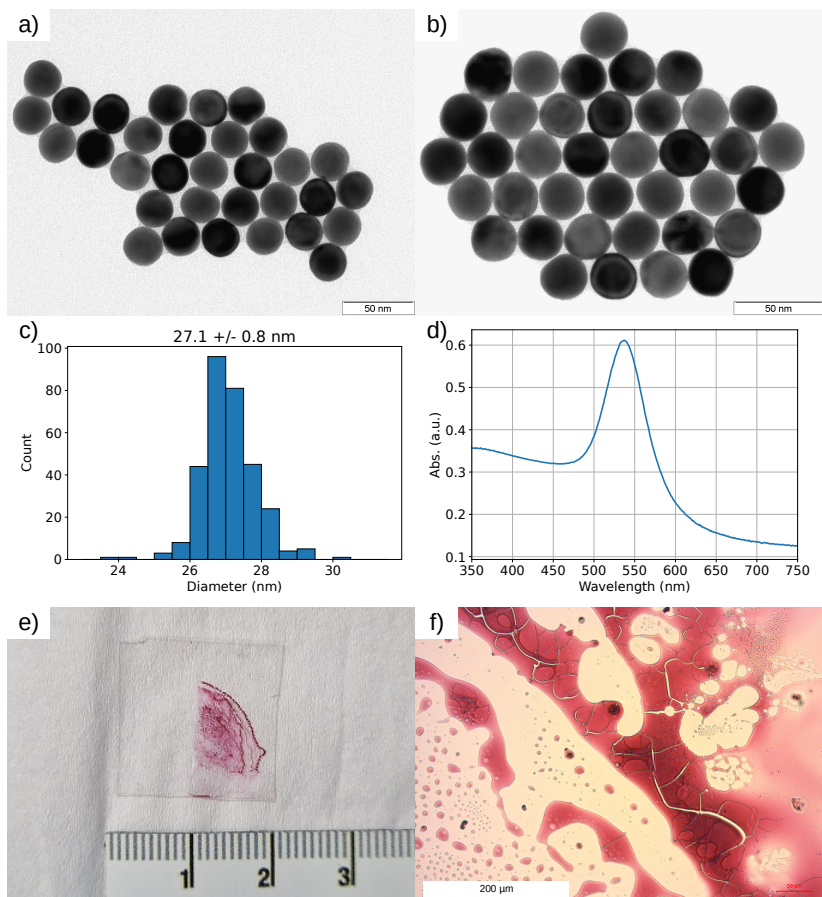


Figure 4.3: Characterization of the sample. **a)-b)** Representative TEM images of the AuNP@CTAC after synthesis. The white bars measure 50 nm. **c)** Size histogram obtained from analysis of the TEM images. **d)** Absorption spectrum of the AuNP@PSSH25k. **e)** Photograph of the film. The scale bar measures in units of cm. **f)** Optical microscopy image of the film.

ticles with 27.1 nm diameter as shown in the TEM images, c.f. Fig. 4.3a-c. To prepare the solution for spin-coating, a ligand exchange from CTAC to thiolated polystyrene (PSSH, $M_n = 25 \times 10^3$ g/mol) was conducted, changing the dispersion medium from water to toluene. For that, 1 mL of AuNP@CTAC in water were injected rapidly into a mixture of 0.5 mL of PSSH and 1 mL tetrahydrofuran (THF) and the mixture was stirred for another 3 min, resulting in two separate phases. The glass container was then shaken by hand and the AuNP-containing phase stuck to the wall of the vial. This allowed for the remaining liquids to be removed - first by pipette and then by drying over nitrogen for 30 min. Afterwards, the AuNP were redispersed and washed in a PSSH-toluene solution (0.1 mM) by centrifugation and replacement of the supernatant with fresh PSSH solution. The resulting absorption spectrum of the AuNP@PSSH dispersion is shown in Fig. 4.3d. 30 μ L of particle dispersion were then spin-coated onto the substrate at 50 rpm for 10 min. The high volume of dispersion in combination with the low rotation speed ensured that the film showed enough optical contrast in TA at the expense of sample homogeneity (cf. Fig. 4.3e-f). To fit the sample into the cryostat, parts of the substrate had to be cut off and for other tests, which will not be part of this study, half of the film was washed off using a solution of PSSH in toluene.

The TA experiments were conducted using the TA spectrometer described in chapter 3 in reference mode with the exception that the sample was placed in a cryostat chamber. Six temperatures were applied by the cryostat: 50, 100, 150, 200, 250, 300 and 350 K. For each temperature TA measurements with a pump wavelength of 400 nm and the following pump powers were conducted: 50, 100, 150, 200 $\frac{\mu\text{J}}{\text{cm}^2}$. Each measurement consisted of 2 scans with an averaging time of 1 s per delay time.

The data were corrected for chirp and scattering and time-zero was set to the delay time of maximum bleach contrast. The bleach kinetic was obtained for each measurement by fitting a polynomial function to the bleach and saving the minimum value of that fit for each delay time. The resulting kinetic was then normalized and fitted with an (bi) exponential function to obtain the e-ph coupling time.

Two challenges had to be overcome up to this point: For some of the applied temperatures, the measured data did not show the expected behavior within one series. Fig. 4.4 shows a comparison between a typical and a-typical power series. As mentioned before, the contrast in TA scales with the deposited energy and while there is always a small spectral shift of the bleach wavelength the features usually do not deviate too much except from an increasing intensity with increasing power. Fig. 4.4b however shows both a-typical spectral and intensity shifts of the bleach. These measurements also yielded much lower overall contrast. Hence, the measurement series for some temperatures (200 K, 250 K and 300 K) were repeated. The 300 K series was repeated to test the robustness of the experiment. Within the whole data set, the comparison of the results will thus be affected by the fact that not all measurements were taken on the same spot of the sample. Because of imperfect coating of the substrate with AuNP, sample inhomogeneity from spot to spot has to be taken into account.

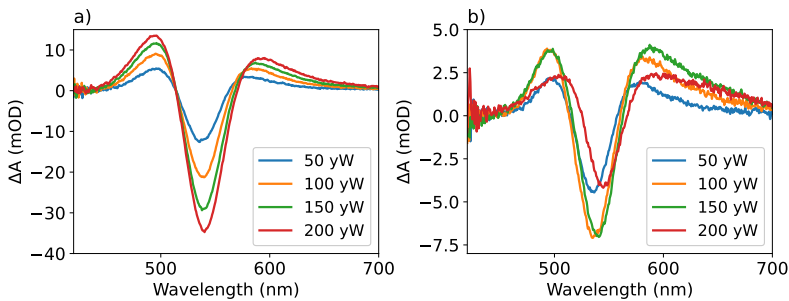


Figure 4.4: Comparison of **a)** good quality power series and **b)** bad quality power series.

The second challenge was the fitting of the bleach kinetic. Usually, a kinetic is fitted using a biexponential function, because the signal decays via two processes: e-ph coupling and heat transfer to the environment. Thus, the time-constants of the fit can be directly related to these processes. However, the measured kinetics have shown artifacts at 7 ps and 23 ps, which could not be

avoided experimentally. Two options of the fit function were tested: Either only the first 6 ps were fitted using only a single exponential decay, or the whole kinetic was fitted using a bi-exponential function. An exemplary comparison of the fits is displayed in Fig. 4.5. For the calculation of the e-ph coupling constant, the precision of the e-ph coupling time is more important than the fitting of both e-ph coupling and heat transfer to the surroundings. Fig. 4.5 shows that especially the artifact at 7 ps leads to an underestimation of the e-ph coupling time with respect to the better quality fit of the first 6 ps by a single exponential decay.

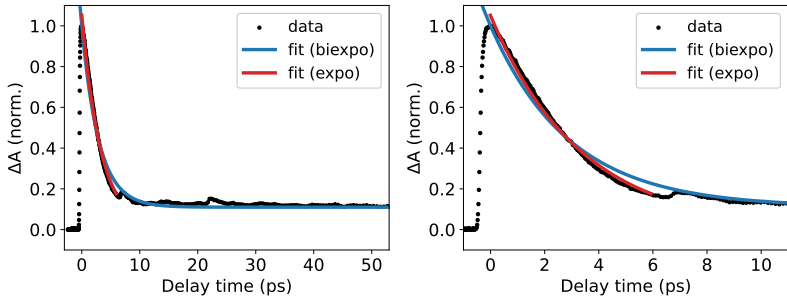


Figure 4.5: Bleach kinetics and fits for TA measurements taken at $T_{env} = 300$ K and fluence of $300 \mu\text{J}/\text{cm}^2$

Fig. 4.6a shows the determined e-ph coupling times using the two fit routines for both measurement series taken at $T_{env} = 300$ K. The e-ph coupling times determined using the biexponential fit are about 10 % lower than the values determined from the single exponential fit. Both fit routines lead to consistent values for repeated measurements up to a pump fluence of $150 \mu\text{J}/\text{cm}^2$ - showing the robustness of the data acquisition and analysis. The root-mean-square-error and R^2 values of the fits confirm the higher fit quality of the single exponential fit, cf. Fig. 4.6b-c. Hence, the e-ph coupling times determined from a single exponential decay of the first 6 ps were used for further analysis. Since the first few picoseconds of the TA dynamic are dominated by e-ph coupling and phonon-phonon coupling is a much slower

process, it can be assumed that treating this as a single process and not as a superposition of two processes is accurate.

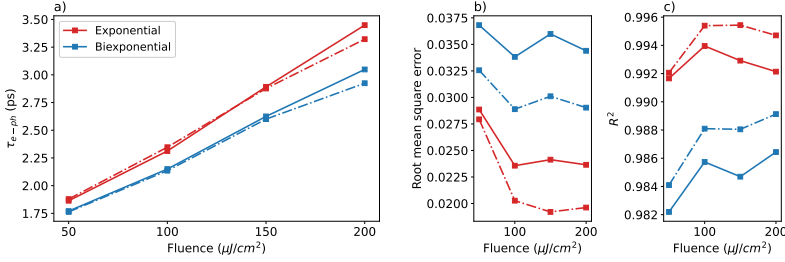


Figure 4.6: **a)** e-ph coupling times determined from exponential (red) and biexponential (blue) fits of the data taken at $T_{env} = 300$ K (solid: first measurement, dashed: second measurement). **b)** Root-mean-square-error and **c)** R^2 values of the fits.

Measuring TA at low temperatures requires to put the sample in a vacuum. This might reduce the heat transfer to the environment and in turn affect the measurements by constantly heating the sample. To ensure that this is not an issue, two measurements were performed at room temperature and two pressures: atmospheric pressure and the vacuum pressure employed in this study. The kinetics and spectra displayed in Fig. 4.7 show the same results for both cases. Hence, it can be assumed that the e-ph coupling times are not affected by the low-pressure environment.

The resulting e-ph coupling times were related not to the employed pump power, but to the increase in electron temperature $\Delta T_{e,0}$, which is related to the absorbed energy per unit volume of Au, U , via:

$$U = \frac{1}{2}\gamma \left((\Delta T_{e,0} + T_{env})^2 - T_{env}^2 \right) \quad (4.3)$$

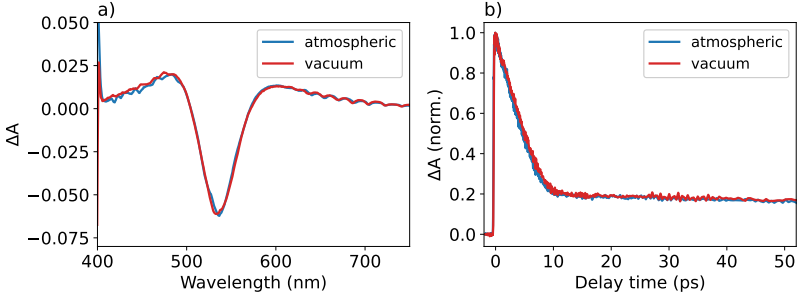


Figure 4.7: a) TA-spectra at maximum contrast and b) bleach kinetics measured at atmospheric pressure ($>1 \times 10^3$ hPa) and vacuum (4×10^{-5} hPa).

where γ is the electron heat capacity coefficient for bulk gold [21, 83]. The exact volume of Au excited by the pump could not be determined experimentally, because of the inhomogeneity of the AuNP film. Hence, U was calculated by multiplying the employed pump power per pulse, P , with the absorption cross section of 27 nm AuNP at a pump wavelength of 400 nm, σ , and divided by the volume of AuNP of that size, V :

$$U = \sigma \frac{P}{V}. \quad (4.4)$$

$\sigma = 7.78 \cdot 10^{-16} \text{ m}^2$ was calculated using Mie-theory with the refractive index taken from the data by Johnson and Christy [53] and the refractive index of the polystyrene ligand as the medium ($n_{\text{medium}} = 1.625$, [113]). Figure 4.8 shows the resulting increase of the electron temperature as a function of pump fluence for each environment temperature.

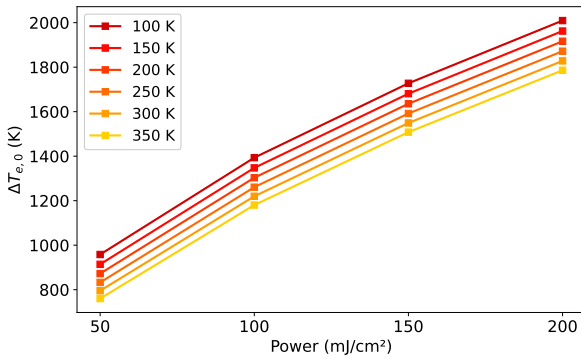


Figure 4.8: Increase in electron temperature calculated as described in Eqs. 4.3 and 4.4.

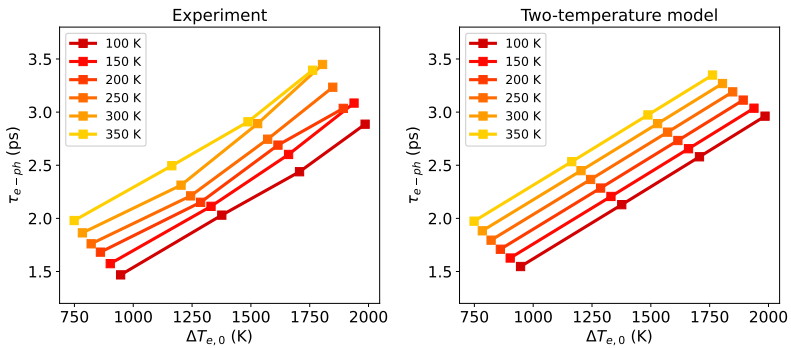


Figure 4.9: E-ph coupling times obtained from TA and the 2TM vs. increase in electron temperature after optical excitation.

4.3 Discussion

Figure 4.9 shows a comparison of the e-ph coupling times obtained from TA with the e-ph coupling times simulated by the 2TM under the assumption of a temperature-independent g . The experimental values of the e-ph coupling times reproduce the simulated values of the 2TM very well. Therefore, the results of this study indicate that the e-ph coupling constant g is indeed independent of the environmental temperature in the range employed here including temperatures below the Debye temperature. However, the experimentally determined e-ph coupling constant ($g_{\text{exp.}} = (4.8 \pm 0.3) \times 10^{16} \text{ W/m}^3\text{K}$) is on average twice as high as the value used for the 2TM simulation ($g_{\text{sim.}} = 2.4 \times 10^{16} \text{ W/m}^3\text{K}$), which was measured in an earlier study on the same particles in solution [24]. If the e-ph coupling times were determined using a biexponential instead of a single exponential fit, the e-ph coupling constant was even higher ($g_{\text{exp.}} = (5.7 \pm 0.3) \times 10^{16} \text{ W/m}^3\text{K}$). The reason that the simulated values are this close despite the difference in g is probably a systematic error in fitting the electron temperature as an exponential decay. As shown in Fig. 4.10a-b, the 2TM does not predict a purely exponential behavior of T_e . The error in the fit then probably compensates for the differences in g - leading to similar τ_{e-ph} in the end. Directly fitting the electron temperature simulated by the 2TM to the data was not successful for every measurement, c.f. Fig. 4.10c-d. For these fits, g was used as the only fit parameter and the good fit results yield values ranging from $3.3 \times 10^{16} \text{ W/m}^3\text{K}$ to $3.9 \times 10^{16} \text{ W/m}^3\text{K}$, which is in between the value obtained from the standard analysis and the literature value. In general, the absolute value of g has to be interpreted and used with care, because of the differences in the methodology of its determination, and the multitude of material parameters that influence it - as outlined in chapter 2.2.4.

Another difference between the experiment and simulation that could affect g is the calculation of the energy intake. In this study, the energy intake of the electrons had to be calculated based on the refractive index reported by Johnson and Christy, which was experimentally determined from bulk gold at room temperature [53]. The absorbed energy by a single AuNP was then

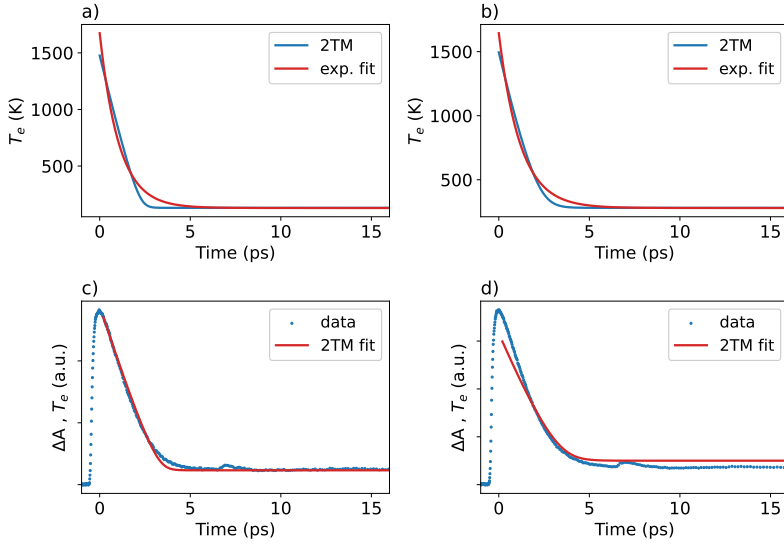


Figure 4.10: **a)-b)** Electron temperature T_e simulated by the 2TM (blue) and the exponential fit (red) that was used to determine τ_{e-ph} . **c)-d)** Bleach kinetics measured in TA (blue), fitted with the electron temperature in the 2TM (red). **a)-c):** $T_{env} = 100$ K. **b)-d):** $T_{env} = 250$ K. Pump fluence in all pictures: $100 \mu\text{J}/\text{cm}^2$.

calculated using Mie-theory as described above. The value of g used for the simulation was determined from particles in a dispersion. There, the energy intake was calculated from the employed fluence and the amount of particles in the illuminated volume determined by the particle concentration. Both routines are based on well established theories. Hence it is hard to assess, which one is preferable over the other. A study of the steady-state absorbance of the sample at low temperatures, which would allow a more precise assessment of the energy intake, could not be concluded by the time of this thesis. However, for ambient temperatures of 298 K and above by Ferrera et al. show an increase in absorbance with temperature, further increasing the uncertainty of the calculated absorbed energy [114]. Using not only g , but also $\Delta T_{e,0}$ as parameters for fitting the electron temperature given by the 2TM directly to the TA data did not result in sensible values, which deviated by sometimes multiple orders of magnitude from literature values.

Regardless of the exact value of g , both the experiment and the 2TM do not show a change in g with ambient temperatures between 100 K and 350 K. Changes in e-ph coupling due to the environmental temperature are fully covered by the temperature-dependent heat capacities of electrons and lattice. Hence, the main hypothesis, that g is indeed a constant with regards to the environmental temperature, is supported by these results. Comparing this study to the work of Giri et al. on Au films at comparable temperatures, a visible effect by the temperature-dependence of the lattice heat capacity below the Debye temperature on e-ph coupling can not be observed here. However, this effect is minimal to begin with - both here (c.f. Figs. 4.2 and 4.9) and in the work of Giri et al. at high fluences. The lowest excitation fluence employed in this study is probably too high to be comparable to their low-fluence results, which show a linear relationship between g and T_{env} in accordance with the low-fluence limit of the τ_{e-ph} vs. T_{env} relationship given in Eq. 3.8.

To summarize, the temperature dependence of the lattice heat capacity below the Debye temperature only has a small effect on the hot electron dynamics. Despite differences in the absolute value of the e-ph coupling constant, the 2TM is able to describe these dynamics and the underlying assumption of the independence of g on electron- and lattice temperatures seem to hold true.

Hence, the valid parameter space of the 2TM could be expanded to temperatures down to 100 K.

Chapter 5

Excitation mechanism of coherent acoustic phonon modes

This study has already been published in the two following articles:

D. Hoeing, R. Salzwedel, L. Worbs, Y. Zhuang, A.K. Samanta, J. Lübke, A.D. Estillore, K. Dlugolecki, C. Passow, B. Erk, N. Ekanayake, D. Ramm, J. Correa, C.C. Papadopoulou, A.T. Noor, F. Schulz, M. Selig, A. Knorr, K. Ayer, J. Küpper, H. Lange, Time-Resolved Single-Particle X-ray Scattering Reveals Electron-Density Gradients As Coherent Plasmonic-Nanoparticle-Oscillation Source. *Nano Letters*, **23**, 13, 5943-5950, (2023) <https://doi.org/10.1021/acs.nanolett.3c00920>

R. Salzwedel, A. Knorr, **D. Hoeing**, H. Lange, M. Selig, Theory of radial oscillations in metal nanoparticles driven by optically induced electron density gradients. *Journal of Chemical Physics*, **158**, 064107 (12 pp) (2023) <https://doi.org/10.1063/5.0139629>

This work is a result of a collaboration of our group with the groups of Prof. Jochen Küpper at the Centre of Free-electron laser science (CFEL), who were mainly responsible for the design and performance of the SPI experiment, the group of Dr. Kartik Ayyer at the Max-Planck Institute for the Structure and Dynamics of Matter (MPI-MPSD), who analyzed the SPI results, and the group of Prof. Andreas Knorr at Technische Universität Berlin, who have developed and simulated the new theoretical framework. My contribution was in the conceptual design of the study, sample preparation and TA experiments as well as assisting the SPI experiment and development of the theory through all phases.

5.1 Introduction

A striking feature observable in TA spectroscopy on AuNP is the oscillation of the signal on the edges of the bleach, c.f. Fig. 5.2. This is an effect of coherent phonon mode excitations, "breathing modes". Breathing modes describe the oscillation of the particle size and shape [44–46, 49, 115–119]. In case of spherical particles the fundamental, most dominant mode is the radial size oscillation [26, 120]. Since the LSPR center frequency is dependent on the electron density, the size oscillation leads to an oscillating red-shift. The work presented in this chapter aims at studying the breathing mode excitation mechanism. The main tool that was previously utilized to observe breathing modes is TA spectroscopy. However, the TA signal at the delay times of the breathing mode onset is dominated by the increased electron temperature and the excitation mechanism is therefore hard to assess. With the development of ultrafast x-ray techniques at free-electron laser (FEL) facilities,

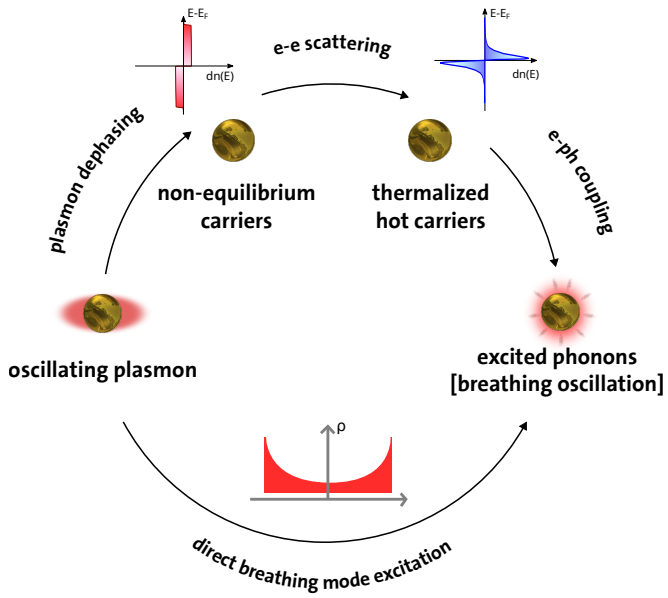


Figure 5.1: Updated overview of the hot electron dynamics, including the new direct breathing mode excitation.

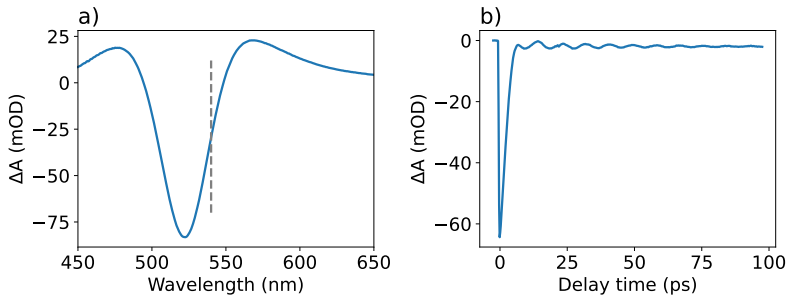


Figure 5.2: Example of breathing mode observation in TA spectroscopy. **a)** TA spectrum of AuNP. The dashed line marks the probe wavelength displayed in **b)**. **b)** Kinetic at a probe wavelength of 545 nm. The breathing mode is observable as an oscillation of the signal after hot electron relaxation.

more possibilities to study the structural dynamics of AuNP emerged over the last decades. This includes the transient small angle x-ray scattering technique "single particle imaging" (SPI) [33, 34]. Small-angle x-ray scattering (SAXS) gives information about the size and shape of a particle ensemble by fitting the measured x-ray diffraction patterns with well known size and form-functions [121]. Utilizing the ultrashort duration of x-ray pulses produced by FELs allows to design a pump-probe SAXS experiment, that includes exciting the sample by optical pulses and probing it by small angle x-ray diffraction. In principle, this technique should allow observing the breathing mode onset without contribution from hot electrons.

Hence, the following study included two experiments: SPI was used to gain insight into the breathing mode onset and TA spectroscopy was performed on the same particles as a reference for the SPI data and to increase the number of applied parameters. Preceding these experiments was the preparation of the samples using established protocols, that needed to be slightly adjusted to meet the requirements of the SPI experiment. For interpretation of the results, they

are compared to predictions made by the newly developed theory presented in the following section.

5.2 Theoretical descriptions of breathing modes

Breathing modes were observed in TA experiments on colloidal AuNP as an oscillation of the LSPR frequency with a period of several ps. According to equation 2.12 the frequency of the LSPR maximum is proportional to the plasma frequency of gold. The plasma frequency in turn, depends on the electron density (c.f. Eq. 2.5). Since a breathing oscillation is basically an oscillation of the particle size, the electron density and thus the LSPR frequency will oscillate accordingly [48, 122, 123].

Breathing modes are usually described using a damped harmonic oscillator:

$$\frac{d^2 R}{dt^2} + \frac{2}{\tau_D} \frac{dR}{dt} + \left(\frac{2\pi}{T}\right)^2 \left[R - \left(R_0 + \frac{R_0 \alpha}{3} \right) \right] = 0 \quad (5.1)$$

where R is the particle radius, R_0 is the equilibrium radius, τ_D is a phenomenological damping term, and T is the period of the oscillation [124], which can be well described using the mechanistic model of an elastic sphere introduced by Horace Lamb [125]:

$$T = \frac{2\pi R c}{\eta c_l}. \quad (5.2)$$

Here, c is the speed of light, c_l is the longitudinal speed of sound and η is an eigenvalue of $\eta \cot \eta = 1 - \frac{\eta^2}{4\delta^2}$ with $\delta = \frac{c_l}{c_t}$ (c_t is the transverse speed of sound). α is a thermal expansion coefficient that can be expressed as

$$\alpha = \frac{1}{B} \left(\gamma C_L + \frac{2}{3} C_e(T_e) \right) \quad (5.3)$$

with the bulk modulus B and the Grüneisen parameter γ . The form of this parameter already indicates the importance of an electronic contribution to the excitation of breathing modes. First attempts modeled the excitation mechanism of the breathing mode as a result of rapid lattice heating. As a result, the phase of the modeled oscillation always lagged behind the experimentally observed oscillation. However, since the temperature of hot electrons is very high for a few ps, the usually large difference between the electron and lattice heat capacity is compensated for a short amount of time and both the electron and lattice have to be accounted for. Among a few works, which aimed at resolving this phase difference [48, 49, 124], Perner et al. have adapted the formalism of hot electron pressure by V.E. Gusev to explain the electronic contribution to the breathing mode excitation [45, 126]. In their work, the thermal stress on the lattice has the form $\sigma = \sigma_L + \sigma_e$ and the lattice and electronic contributions are given by

$$\sigma_{L,e} = -\gamma_{L,e} \int_{T_0}^{T_{L,e}} C_{L,e} dT_{L,e} \quad (5.4)$$

Under the assumption of an isotropic electron distribution in k -space, the electronic term can be interpreted as the pressure of the electron gas. The sudden increase in electronic temperature leads to a high "pressure" of the electron gas that exerts a force on the atomic lattice, adding to the thermal expansion due to the lattice temperature rise. Including this factor allowed for modeling the breathing oscillation with an exact phase by solving an equation of motion for the deviation from the equilibrium size of the particle Δx :

$$\frac{d^2}{dt^2} \Delta x + 2\rho \frac{d}{dt} \Delta x + \omega_0^2 \Delta x = A\sigma/m \quad (5.5)$$

where ρ is a damping of the oscillation through interaction with the surrounding medium, ω_0 is the eigenfrequency of the fundamental size oscillation along a particular axis, A is the surface area and m is the mass of the particle. This model of the breathing oscillation was successfully expanded for other materials and particle shapes and the reader is referred to a review by G. Hartland that summarizes additional effects for non-spherical particles [46].

Microscopic theory for the excitation of breathing oscillations

In the context of our combined TA and SPI study, we have taken a close look at the onset of the breathing oscillations and in collaboration with our partners, we present an alternative theory of the breathing mode onset [47]. The framework is based on a Heisenberg equation of motion. We use the following Hamiltonian:

$$H = H_e + H_p + H_{inter} + H_{ep} + H_{ee} + H_{pp} \quad (5.6)$$

with

$$H_e = \sum_{\mathbf{k}, \lambda} \epsilon_{\mathbf{k}}^{\lambda} \lambda_{\mathbf{k}}^{\dagger} \lambda_{\mathbf{k}} \quad (5.7)$$

$$H_p = \sum_{\mathbf{q}} \hbar \omega_{\mathbf{q}} b_{\mathbf{q}}^{\dagger} b_{\mathbf{q}} \quad (5.8)$$

$$H_{inter} = - \sum_{\mathbf{k}, \mathbf{K}, \lambda} \mathbf{d}^{\lambda \bar{\lambda}} \cdot \mathbf{E}_{-\mathbf{K}} \lambda_{\mathbf{k}}^{\dagger} \bar{\lambda}_{\mathbf{k}+\mathbf{K}} \quad (5.9)$$

$$H_{ep} = \sum_{\mathbf{q}, \mathbf{k}, \lambda} g_{\mathbf{q}}^{\lambda} \lambda_{\mathbf{k}+\mathbf{q}}^{\dagger} \lambda_{\mathbf{k}} \left(b_{\mathbf{q}} + b_{-\mathbf{q}}^{\dagger} \right) \quad (5.10)$$

$$H_{ee} = \frac{1}{2} \sum_{\substack{\mathbf{k}, \mathbf{k}', \mathbf{q} \\ \lambda \lambda'}} V_{\mathbf{q}} \lambda_{\mathbf{k}+\mathbf{q}}^{\dagger} \lambda'_{\mathbf{k}'-\mathbf{q}} \lambda'_{\mathbf{k}'} \lambda_{\mathbf{k}} \quad (5.11)$$

$$H_{pp} = \sum_{\mathbf{q}_1 \mathbf{q}_2 \mathbf{q}_3} h_{\mathbf{q}_1 \mathbf{q}_2 \mathbf{q}_3} \left(b_{\mathbf{q}_1} + b_{-\mathbf{q}_1}^{\dagger} \right) \left(b_{\mathbf{q}_2} + b_{-\mathbf{q}_2}^{\dagger} \right) \left(b_{\mathbf{q}_3} + b_{-\mathbf{q}_3}^{\dagger} \right) \quad (5.12)$$

$H_e(H_p)$ includes the electron (phonon) dispersion with respective annihilation and creation operators, H_{inter} accounts for direct interband transitions, H_{ep} describes e-ph coupling, H_{ee} the carrier-carrier Coulomb interaction and H_{pp} the phonon-phonon interactions resulting from the lattice anharmonicity.

We also define the microscopic phonon mode amplitude $s_{\mathbf{q}}$, which will determine the macroscopic lattice displacement, as

$$s_{\mathbf{q}}(t) = \frac{1}{2} \left(\langle b_{\mathbf{q}} \rangle (t) + \langle b_{-\mathbf{q}}^{\dagger} \rangle (t) \right) \quad (5.13)$$

with the phonon annihilation (creation) operators $b_{(-)\mathbf{q}}^{(\dagger)}(t)$. In gold, interband transitions occur from the 5d to the 6sp-band [127]. We therefore arrive at the equation of motion for the phonon mode amplitude in a two-band system (denoted \mathbf{c} for conduction band and \mathbf{v} for valence band):

$$\begin{aligned} \left(\partial_t^2 + 2\gamma_{\text{ph}}^{\mathbf{q}} \partial_t + \omega_{\mathbf{q}}^2 \right) s_{\mathbf{q}}(t) = & -\frac{\omega_{\mathbf{q}}}{\hbar} \sum_{\mathbf{k}} (g_{-\mathbf{q}}^c - g_{-\mathbf{q}}^v) \tilde{f}_{\mathbf{k}}^c(\mathbf{q}, t) \\ & - \frac{3\omega_{\mathbf{q}}}{\hbar} \sum_{\mathbf{k}} \tilde{h}_{-\mathbf{q}, \mathbf{k}, \mathbf{q}-\mathbf{k}} \delta \tilde{n}_{\mathbf{k}}(\mathbf{q}, t). \end{aligned} \quad (5.14)$$

The left hand side of Eq. 5.14 describes a damped harmonic oscillator with the damping factor $\gamma_{\text{ph}}^{\mathbf{q}}$ resulting from phonon-phonon interactions and the phonon dispersion $\omega_{\mathbf{q}}$. On the right hand side we notice two source terms, that arise from this framework: The first term includes the Fourier transformed Wigner-functions for the band occupations $\tilde{f}_{\mathbf{k}}^c(\mathbf{q}, t) = \langle \lambda_{\mathbf{k}-\mathbf{q}}^\dagger - \lambda_{\mathbf{k}} \rangle$. Therefore, a spatial inhomogeneous electron distribution drives the phonon amplitude $s_{\mathbf{q}}(t)$ [128], which scales with the difference of the e-ph coupling element of valence and conduction band ($g_{-\mathbf{q}}^c - g_{-\mathbf{q}}^v$). The second term describes the change in phonon occupation by phonon-phonon interactions, caused by the heat transfer from electrons to phonons with $\tilde{n}_{\mathbf{k}}(\mathbf{q}, t) = \langle b_{\mathbf{k}-\mathbf{q}}^\dagger b_{\mathbf{k}} \rangle(t)$ and $\delta \tilde{n}_{\mathbf{k}}(\mathbf{q}, t) = \tilde{n}_{\mathbf{k}}(\mathbf{q}, t) - \tilde{n}_{\mathbf{k}}(\mathbf{q}, t \rightarrow -\infty)$.

From there we further investigate the Wigner functions via (1) deriving an equation of motion with individual Wigner occupations for valence and conduction band, (2) expanding the Wigner functions in orders of the electric field and applying a rotating wave approximation, (3) deriving equations for the time-dependent Wigner occupations. Applying a coarse-graining procedure with the lattice displacement given in Eq. 5.16 and a momentum expansion of the Wigner occupations $\rho^\lambda(\mathbf{r}, t) \equiv e\Omega^{-1} \sum_{\mathbf{k}} f_{\mathbf{k}}^\lambda(\mathbf{r}, t)$ lets us write macroscopic equations for the carrier densities in the two-level system $\partial_t \rho_2^v(\mathbf{r}, t)$ and $\partial_t \rho_2^c(\mathbf{r}, t)$. Via the macroscopic susceptibility $\chi^{\text{inter}}(\omega_{\text{opt}})$, the contribution of the interband transitions can be identified and the macroscopic description of the carrier densities in the respective bands read:

$$\partial_t \rho_2^{c,v}(\mathbf{r}, t) = \frac{2e\epsilon_0}{\hbar} |\mathbf{E}(\mathbf{r}, t)|^2 \text{Im} \{ \chi^{\text{inter}}(\omega_{\text{opt}}) \} - \frac{1}{\tau} \rho_2^{c,v}(\mathbf{r}, t) \quad (5.15)$$

with the elementary charge e , the vacuum dielectric function ϵ_0 , and the electric field $\mathbf{E}(\mathbf{r}, t)$. The last term includes the radiative lifetime τ of the electrons in the conduction band, which was added phenomenologically to the Wigner occupations.

The lattice displacement \mathbf{u}_β at position \mathbf{r} and time t is defined as

$$\mathbf{u}_\beta(\mathbf{r}, t) = \sum_{\mathbf{q}} \sqrt{\frac{\hbar}{2mN\omega_{\beta,\mathbf{q}}}} \mathbf{A}_{\beta,\mathbf{q}} e^{i\mathbf{q}\cdot\mathbf{r}} \langle b_{\beta,-\mathbf{q}}^\dagger(t) + b_{\beta,\mathbf{q}}(t) \rangle \quad (5.16)$$

with the reduced Planck constant \hbar , effective mass of the unit cell m , the number of unit cells in the crystal N , phonon dispersion $\omega_{\beta,\mathbf{q}}$ with momentum \mathbf{q} and branch $\beta = LA$, and phonon annihilation (creation) operators $b_{\beta,\mathbf{q}}^{(\dagger)}$. With that, we finally arrive at the equation of motion for the lattice displacement:

$$[\partial_t^2 + 2\gamma_{\text{ph}}\partial_t - c_{LA}^2\nabla_{\mathbf{r}}^2] \mathbf{u}(\mathbf{r}, t) = \zeta \nabla \rho_2^c(\mathbf{r}, t) + \xi [T(t) - T_0]. \quad (5.17)$$

For the equation of motion of the phonon amplitude, we identify two source terms, which scale with their respective prefactors ζ, ξ . The first source term results from an optically induced gradient in the spatial electron distribution, while the second term accounts for the classic thermal excitation, with temperatures given by the two-temperature model. A numerical solution, that allows to switch the individual source terms on and off, reveals the phase difference resulting from the two excitations:

Figure 5.3 displays three predictions of the breathing mode onset depending on the source terms used for the numerical simulation. The source term involving the electron density gradient leads to a more rapid lattice displacement than the purely thermal source term. The resulting phase difference is in line with the studies mentioned above, which have also introduced additional

source terms, e.g. hot electron pressure, to model a faster breathing mode onset [45, 48, 49, 124]. As this simulation was performed for a fixed excitation fluence of the particles, we can also determine that for a given energy influx and at short time scales, the electron density gradient dominates the overall amplitude of the lattice displacement when both source terms are employed. Furthermore, the theory predicts differences in the excitation fluence dependency of the two source terms. While the $\nabla\rho_2^e(\mathbf{r}, t)$ contribution does not include any power-dependent phase, the thermal contribution does. The initial electron temperature - and thereby the initial temperature difference in the thermal source term - is proportional to the excitation fluence (cf. Eq. 2.16), which introduces a time-difference for the energy transfer from electrons to phonons and a resulting phase difference with excitation fluence.

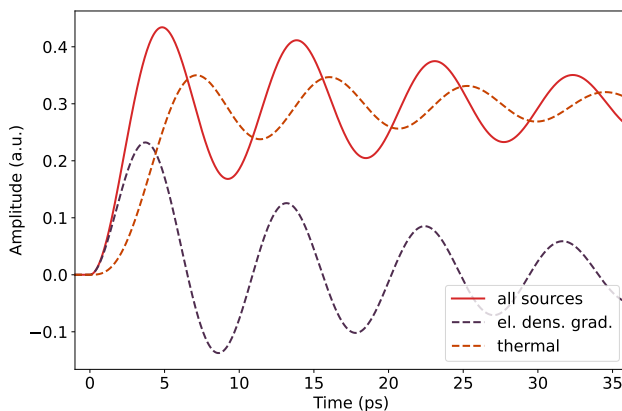


Figure 5.3: Predictions of the breathing mode onset by our microscopic theory. The solid curve displays the breathing amplitude of all source terms are used, while the dashed lines are the expected breathing amplitudes based on the individual source terms only. The simulation was performed for a spherical AuNP of 27 nm diameter, excitation wavelength of 400 nm and excitation fluence of 1.8 mJ/cm². Reprinted with permission from Ref. [129]. Copyright 2023 American Chemical Society.

5.3 Experiments and data analysis

5.3.1 Particle synthesis

The synthesis of the sample for SPI and TA followed the protocols introduced in chapter 3. The aim was to produce AuNP with the lowest possible size distribution, because the predicted size changes during breathing oscillations were expected to be smaller than the standard deviation of a typical ensemble produced by our approaches [46]. SPI imposed an additional criterion: To maximize the number of recorded diffraction patterns during the experiment, the AuNP dispersion had to be of the maximum possible particle concentration - especially since it would eventually be mixed with ammonium acetate prior to electrospraying.

The best synthesis route at that time to produce highly uniform, spherical particles was the modified protocol by Zheng et al. introduced in chapter 3 [27]. After synthesizing the particles and cleaning the dispersion, additional centrifugation steps were introduced to achieve the maximum possible concentration. In order to obtain a sufficient sample volume - given the predicted rate of usage during SPI - the initial synthesis had to be scaled up in comparison to the usual protocols developed in our group. The scaling was limited by two factors: (1) The sample preparation was conducted during the early COVID-19 pandemic, which limited the available time for producing a single batch. For organizational matters this meant, that a single synthesis should be completed within a day of work. (2) This in turn led to the second limit: the maximum capacity of the centrifuges. The reaction of particle growth is stopped by ending the precursor input and then quickly washing the dispersion to discard unreacted precursor. To avoid differences in the reaction time within a batch, the whole dispersion therefore had to be washed simultaneously. Within these limits, the protocol by Zheng et al, which results in ca. 4 mL of AuNP solution after the complete addition of all precursors, was successfully up-scaled to yield 240 mL at that point. As described below, this

volume was reduced by centrifugation and redispersion of the AuNP to 6 mL, thereby increasing the particle concentration.

Procedure

All chemicals were purchased from Sigma-Aldrich (USA), and used as received. Ultrapure water was used for all procedures and the reactions were conducted at room temperature and pressure. The procedure included 3 steps: (1) Preparation of a cluster solution, which was (2) directly converted to 10.6 nm AuNP. This solution served as seeds for (3) the seeded growth of the particles to the final size of roughly 30 nm.

The Au clusters were produced by mixing 0.1 ml HAuCl₄ (0.25 mM) with 10 ml CTAB (100 mM) and adding 600 μ L of an aqueous solution of NaBH₄ (10 mM) via one-shot injection. The solution was stirred during mixing, injection and an additional 3 minutes. The solution was then kept undisturbed for 3 hours. The clusters were grown to 10.6 nm AuNP by first mixing 2 ml, 0.5 mM HAuCl₄ with 2 ml, 200 mM CTAC and 1.5 ml, 100 mM AA. While stirring at 300 rpm 50 μ L of the cluster solution was added to the mixture by one-shot injection. The solution was stirred for additional 15 minutes before it was washed twice by centrifugation (20 000 G, 90 minutes each time) and replacement of the supernatant with fresh 10 ml, 20 mM CTAC.

The final particles were prepared by another seeded growth step: 3.6 ml of the 10.6 nm AuNP dispersion was mixed with 120 ml, 100 mM CTAC. AA (780 μ L, 100 mM) was added and after 1 minute of mixing, 120 ml, 0.5 mM HAuCl₄ was added drop-wise within 1 hour. During addition of AA and HAuCl₄ and an additional 10 minutes, the solution was stirred at 300 rpm. A total of five centrifugation steps followed in order to wash the dispersion and sequentially increase the concentration by replacing the supernatant with less CTAC (20 mM) each time: 5000 G, 2x 40 min in 40 ml tubes, 3x 20 min in 1.5 ml tubes. The final pelet was redispersed in 6 ml, 20 mM CTAC.

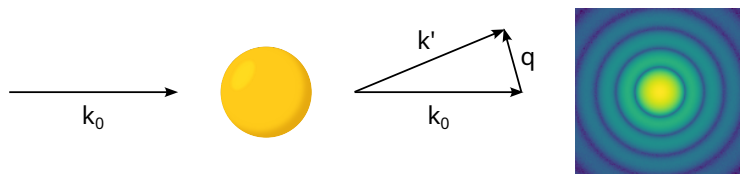


Figure 5.4: Illustration of SAXS on AuNP. Incident x-rays with wave vector k_0 are scattered by the particle. k' denotes the wave vector of the scattered light at a given deviation from the incident x-rays. The deviation is described by the scattering vector q .

The resulting particles were characterized via UV-Vis spectroscopy for a quick assessment of the particle quality and to calculate the particle concentration and by TEM for assessment of the particle shape and size distribution. For UV-Vis the sample was diluted by a factor of 1:100 with 20 mM CTAC solution, which also served as background. To record TEM images a carbon-coated copper grid was covered with a 8 μL droplet of the AuNP dispersion, which dried overnight.

5.3.2 Single-particle imaging

Overview

Single particle imaging is a time-resolved x-ray scattering technique that utilizes ultrashort x-ray pulses with high brilliance produced by FELs. The technique is described in two parts here: First, the basic principles of SAXS are introduced. Afterwards the special considerations of conducting SAXS as single particle imaging (SPI) are explained.

Small-angle x-ray scattering

X-rays are electromagnetic radiation with wavelengths between 10 nm and 10 pm or photon energy between 100 eV to 100 keV. X-rays on the lower energy side of the spectrum are referred to as *soft* x-rays and the high energy radiation as *hard* x-rays. Many experimental techniques have been developed since Wilhelm Conrad Röntgen discovered the radiation in 1896 [130]. Among the x-ray diffraction techniques, SAXS has been widely applied in studying the size, shape and morphology of nanomaterials. As illustrated in Fig. 5.4, the diffracted x-rays are projected onto a screen resulting in 2D scattering patterns. The x-y-dependent intensity $I(\mathbf{q})$ depends on the scattering vector \mathbf{q} , which describes the deviation of the scattered light relative to the incident x-rays:

$$\mathbf{k}' = \mathbf{k}_0 + \mathbf{q} \quad (5.18)$$

where \mathbf{k}_0 and \mathbf{k}' are the wave vectors of the incident and scattered light, respectively. For a spherical, uniform object the background subtracted intensity on the screen is the product of a form factor $P(q)$ and a structure factor $S(q)$:

$$I(q) = P(q) \cdot S(q) \quad (5.19)$$

with $I(q) = I(\mathbf{q})$ because of the spherical symmetry. The form factor is given by the electron density difference between object and background and a shape function, while the structure factor describes the interference between the scattered light of objects in close proximity. For a single object, the form factor amplitude is basically the Fourier transform of the electron density difference [121].

Hence, x-ray diffraction is sensitive to the electron density, with high density materials scattering at larger \mathbf{q} than low density materials. Additionally, the scattering vector is inverse to the size of the probed object. For example, the

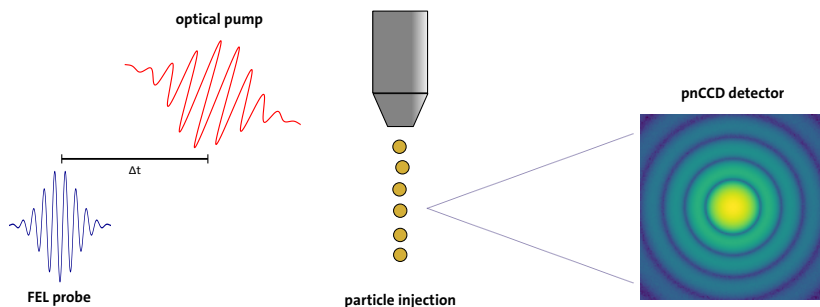


Figure 5.5: Illustration of single-particle imaging. AuNP are continuously injected into a vacuum chamber by an "Uppsala injector". These are individually excited by an optical, femtosecond laser system and time-delayed x-ray pulses produced by a FEL probe the sample. The diffracted x-rays are projected onto a pnCCD detector. From the resulting scattering patterns, the size and shape of the particles can be determined.

high-density atomic cores lead to Bragg diffraction with large \mathbf{q} , while metallic nanoparticles dispersed in a dielectric scatter at smaller \mathbf{q} . The recorded patterns not only contain information about the dimension of an object, but also on its shape. Crystalline materials scatter in different directions depending on the type and orientation of the crystal. The orientation and form of nanoparticle ensembles or nanoporous materials can be assessed by fitting the patterns to well known form- and structure factors.

Single-particle imaging

Single particle x-ray diffractive imaging is a pump-probe technique based on SAXS, illustrated in Fig. 5.5. The pump is a femtosecond (optical) laser pulse and the sample is probed by time-delayed x-ray pulses. The technique was made possible by the development of FELs, which are able to produce very bright, femtosecond x-ray pulses with low bandwidth. To further develop the

technique towards studying biomolecules, substrate-free sampling methods are routinely applied. Instead of mounting the sample on a substrate and dealing with a large background signal, aerosolized particles are streamed into the x-ray focus and discarded in a sample dump. This design is based on a measure-before-destruct principle, which is very useful for measuring easily damaged biomolecules. Additionally, it allows to sort the measured single-particle diffraction patterns, such that the signal from non-spherical particles or the interference between adjacent particles can be eliminated from the combined sample signal.

The particle stream is routinely produced at FEL facilities by an "Uppsala injector", which is a combination of an aerosolizer, a skimmer and a stack of aerodynamic lenses, that focus the particles into the x-ray beam. Aerosolizing is first achieved by electrospraying and the particles are subsequently accelerated and focused by the skimmer and aerodynamic lens stack [131, 132]. Under optimal conditions this results in single particles streaming through the focus with a constant rate. For AuNP the focus spot and rate of particle delivery can be easily monitored by elastic scattering of an optical laser.

The focus of the particle beam is where they interact with the pump and probe radiation. While the pump pulses are easily produced in the same way as introduced in chapter 3, the probe pulses must be delivered by FELs to achieve enough contrast and time resolution. FELs use similar processes as synchrotrons: they produce electromagnetic radiation emitted from accelerated electrons [133]. If electrons have relativistic speeds and are accelerated on a curved trajectory, they emit light tangential to the trajectory. The difference between FELs and synchrotron sources is that FELs are linear light sources that make use of undulators. First, electrons are produced and accelerated in a linear accelerator. Then they pass through an undulator, which is an array of magnets with alternating pole-directions. The electrons are thereby forced on an sinusoidal trajectory. The interaction between the electrons and the emitted undulator radiation leads to a self-modulation of the electrons into microbunches and the resulting radiation is coherent, has a narrow bandwidth and high brilliance. After the undulator, the particle and x-ray beam are sep-

arated by diverting the electrons into a dump and the x-ray beam is focused into the reaction chamber [133].

At this point, the usual principles of pump-probe techniques apply: The delay between pump and probe is controlled by a delay stage and for each delay time, a series of single-particle diffraction patterns are measured by the detector. The analysis of individual diffraction patterns follow the same principles as in conventional SAXS, but the analysis method of the whole data set collected at FEL experiments is continuously developed. In this work, the recently published technique by Ayer et al. [34] was applied, which includes a sorting algorithm (EMC, [111], implemented in Dragonfly), which categorizes each diffraction pattern into automatically generated models. For spherical AuNP, the resulting models are based on size and ellipticity of the particles in addition to noise-producing patterns like hits by aggregates, or scattering by different species such as ligand micelles. Other types of noise from artifacts or cosmic rays are included as well. The combination of recording single-particle patterns with this analysis method allows to subtract unwanted contributions from the overall data set and thereby delete the noise produced by sample heterogeneity, contamination and other sources.

Procedure and data analysis

The experiment was conducted at the BL1 (CAMP) endstation at the FEL *FLASH* at the Deutsches Elektronen-Synchrotron (DESY) [134]. The experimental devices included KBr mirrors for incoupling of the FEL radiation, a spherical holed mirror for incoupling of the optical pump beam, the 3D and angle adjustable interaction chamber with the pnCCD detectors [135, 136] as well as several apertures to block stray light. From user side, the setup was complemented with the particle injection system and the motorized focusing screens including a photodiode for detection of the reflection. A sketch of the experimental setup is shown in Fig. 5.6.

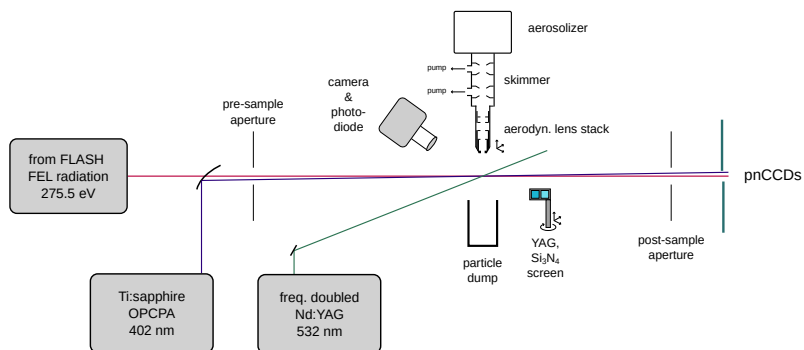


Figure 5.6: Sketch of the experimental setup at the BL1 endstation for the SPI experiment. Except the optical lasers, all devices shown in this figure were either placed within or attached to a vacuum chamber. The 3D adjustable YAG and Si₃N₄ screen was used to define the focus position within the chamber. All three laser sources were focused onto that point. The injector system was motorized as well in order to deliver the AuNP to the focus position.

The FEL delivered x-ray bursts of 100 pulses per train at a photon energy of 275.5 eV with an intratrain repetition rate of 250 kHz. The average fluence per pulse at the focus position was 6×10^9 photons/mm². The pulse length of 120 fs was determined indirectly from the electron bunches. The optical pump was delivered by a optical-parametric chirped pulse amplified Ti:sapphire laser system. The output was frequency doubled by a BBO crystal resulting in a center wavelength of (402.0 ± 3.3) nm at a repetition rate of 500 kHz and 80 fs pulse length as determined from autocorrelation measurements before the beam time [137].

For the pump, probe and particle beam to interact, all systems had to be focused onto the same point in the vacuum chamber. To achieve that, a screen was developed, which could be controlled by a 3D motorized translation stage and that contained two areas: One area was coated with yttrium aluminium garnet (YAG, $Y_3Al_5O_{12}$) and the second area was coated with silicon nitride (Si_3N_4). The screens were monitored using a camera based system and a photodiode. YAG was used to determine the spatial overlap between the x-rays, optical pump beam and a third optical laser (frequency doubled Nd:YAG, Inolas Spotlight), which served as a particle detection laser [138]. Once the spacial overlap was ensured, the particle detection laser was turned off and the screen was moved so that the x-ray and optical pulses hit the silicon nitride thin film. These films are known to change their reflectivity in the optical regime upon excitation with x-rays. The change in reflection is on the time-scale of the convolution of x-ray and optical pulses [139]. Thus, a transient reflectivity measurement was conducted to determine the temporal overlap between x-ray pulses and optical pulses. This time was set as time-zero for SPI.

At this point, the interaction position and time-zero were defined, the control screen was moved out of the interaction position and the particles could be delivered to measure SPI. For delivery of the AuNP the dispersion was mixed with ammonium acetate (5 mM). An aerosol was produced using a commercial electrospray system (TSI Advanced Electrospray 3482) and the aerosolized particles were accelerated and focused onto the interaction point by an aerodynamics lens stack with helium as the carrier gas. Proper sample injection was

ensured by observing the particle detection laser scattering off the particles and monitoring the Taylor cone of the electrospray [132].

Once a sufficient particle flow to the interaction point was established, the detection laser was shut off in order to minimize noise on the x-ray scattering detector. The detector was a two-part large-area pnCCD detector, with individual adjustability of the positioning for each of the two halves. Several apertures were used to minimize the influence of stray light onto the detectors. Unfortunately, it was necessary to block large parts of the detector with the post-sample aperture, because of a signal from an unidentified radiation source within the chamber.

For data collection, the pnCCDs were read out at 10 Hz. The delay stage oscillated between -3 ps and 22 ps with a 0.1 ps/s rate. Once a minimum total signal threshold on the detector was determined, the signal was saved with the current delay time. The resulting data sets for each employed excitation fluence were analyzed as follows: First, the patterns were classified into class averages in *Dragonfly*. Only patterns belonging to spherical particle classes were kept for further analysis. Detected hits of elongated particles, species other than AuNP or other sources of noise that superseded the total signal threshold during the experiment were discarded. Exemplary patterns of these four classes are displayed in Fig. 5.7. The remaining patterns were assigned particle diameters according to the class average and then assigned to the delay time at recording.

The analysis of the resulting data set suffered from a low number of hits per delay time and potential experimental drift, since the delay time oscillated within -3 ps and 22 ps and data was collected at random times. Thus, in order to obtain meaningful results from the resulting data set, the diameters of patterns in a bin of ± 1 ps from the central delay time were averaged. This binning size ensured sufficient statistics while allowing to observe and analyze the breathing oscillation properly. However, because the particle size changes within the time frame of a single bin, the amplitude of the breathing oscillation is not determined precisely, with longer time-per-bin leading to a lower amplitude.

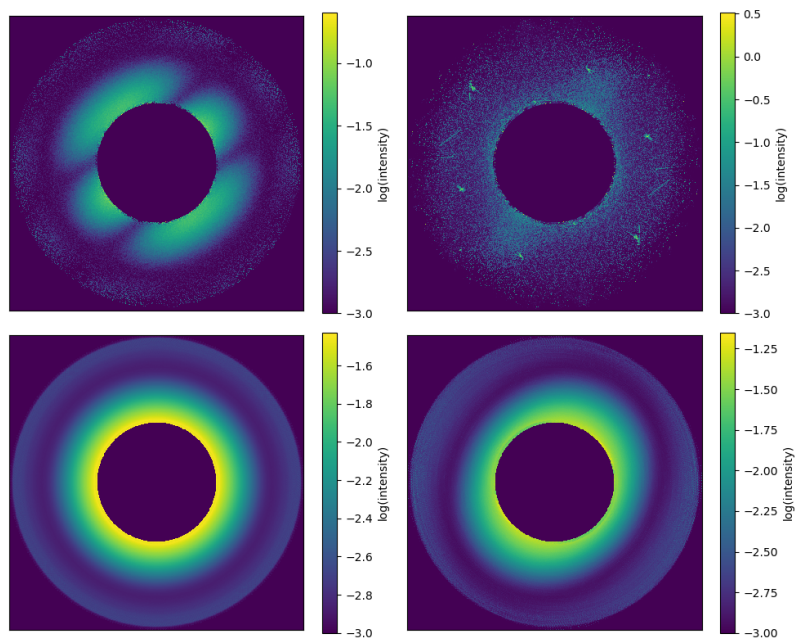


Figure 5.7: Model diffraction patterns for analysis of the SPI data. Top left: Pattern by a AuNP dimer. Top right: scattering from contamination. Bottom left: diffraction pattern of a spherical AuNP. Bottom right: diffraction pattern of an elongated AuNP. Reprinted with permission from Ref. [129]. Copyright 2023 American Chemical Society.

5.3.3 Transient absorption spectroscopy

The TA data were collected using the system described in chapter 3. AuNP from the same batch that was used at the SPI experiment were used as samples. The only differences between the samples (simple AuNP dispersion in a quartz cuvette for TA vs. aerosolized single particles injected into a vacuum chamber for SPI) were the addition of ammonium acetate to the dispersion in SPI, which was not necessary in TA, and a lower concentration of the sample in TA.

For the pump beam, the second harmonic of the fundamental laser output was created in a BBO crystal, resulting in a center wavelength of 400 nm. The WLC was created by focusing the fundamental on a CaF₂ crystal. Spacial overlap was ensured by coarse alignment on an aperture fixed in the sample holder and fine tuning through signal maximizing with the sample. The data were collected using the commercial software of the TA spectrometer manufacturer *Ultrafast Systems Helios*. For each delay time, the TA spectra were averaged within 1 s.

Data analysis

For data analysis, each recording was corrected for scattering of the pump beam and chirp using the commercial software *Ultrafast System SurfaceXplorer*. Finally, the corrected data were exported and all further data analysis was completed using self-written Python scripts. The excitation of coherent phonon modes, aka *breathing* modes, leads to an oscillation of the nanoparticle size and shape. As described in section 5.2 the fundamental breathing mode of spherical AuNP is the oscillation of the size only. This size oscillation leads to the periodic red-shift of the LSPR and is therefore observable in TA data as a modulation of the hot electron dynamics, most prominent on the high gradient sides of the bleach (c.f. Fig. 5.8a). To extract the breathing oscillation from the data, a single $\Delta A(t)$ trace (from here on out called "kinetic") at a probe wavelength of 545 nm was chosen and analyzed. Even though the breathing mode leads to an oscillating red-shift of the LSPR, not the whole ΔA

bleach signal was fitted, but a single kinetic. This analysis requires less fitting of the signal, leading to more robust parameters, but it also complicates the analysis of the breathing mode amplitude. However, the main goal of the analysis is to obtain the frequency and phase of the oscillation. Since the breathing leads to an oscillating red-shift, the only probe-wavelength dependent phase shift is with respect to the LSPR center wavelength and in principle, any probe wavelength to one side of the LSPR center wavelength shows the same phase behavior [46]. 545 nm was therefore chosen for further analysis because of the amplitude of the oscillation in the data: at the point of highest gradient of the ΔA spectrum, a red-shift causes the biggest relative change of the signal. As is obvious in the representative data shown in Fig. 5.8 the oscillation is still superimposed with the hot electron dynamics, which are usually subtracted from the kinetic first as done here, or simply fitted simultaneously.

$$\Delta A = \Delta A_0 \cdot \exp(-t/\tau_D) \cdot \sin(\omega_b t + \phi) \quad (5.20)$$

To determine the basic parameters of the oscillation it is fitted as a damped harmonic oscillator (ref. Eq. 5.20) and since the fundamental Lamb mode of the particles is the most dominant, it describes the oscillation quite well without including higher-order modes. As mentioned in Eq. 5.2 the obtained period of the oscillation is dependent on the particle radius. Phase information are also indicative of the onset of the breathing oscillation and thereby on the excitation mechanism - as will be shown later in this chapter. Lastly, it has been shown, that the main dephasing mechanism of the breathing signal is due to the standard size distribution of the measured particle ensemble, which as a result can be calculated from the dephasing time τ_D via $\sigma = \frac{R_0 T}{\sqrt{2\pi\tau_D}}$ (with mean particle radius, R_0 , and period of the breathing oscillation, $T = (2\pi\omega_b)^{-1}$) [13].

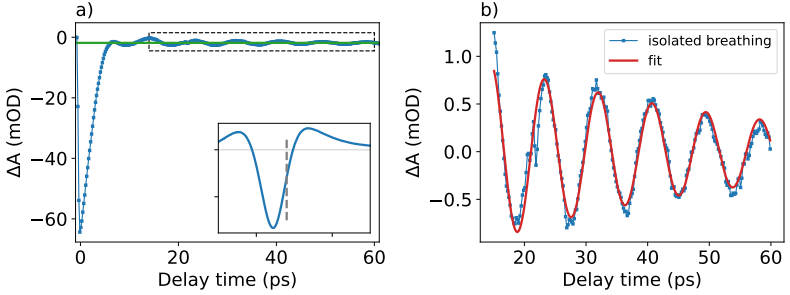


Figure 5.8: Exemplary breathing mode fitting. **a)** blue line: TA kinetic extracted from the long wavelength side of the bleach signal (c.f. dashed line in the inset). Green line: hot electron contribution after e-ph thermalization is fitted to the data and then subtracted from the data. The subset within the dashed box is used for further analysis: **b)** The corrected data (blue) is fitted with a damped harmonic oscillator (red).

5.3.4 Two-temperature model simulations

For the discussion of the results from SPI and TA, the time-dependent electron- and lattice temperatures $T_{e,l}$ had to be known for the given particle system. The model, which was introduced in chapter 2, was implemented here as

$$C_e(T_e) \frac{\partial T_e}{\partial t} = -g(T_e - T_l) + \frac{W_0}{\sqrt{\pi}\sigma} \exp\{-t^2/\sigma^2\}, \quad (5.21)$$

$$C_l \frac{\partial T_l}{\partial t} = g(T_e - T_l) - (T_l - 298)/\tau_s, \quad (5.22)$$

where C_e and C_l are the electron and lattice heat capacities, respectively, taken from literature [22, 140]. g is the e-ph coupling constant and was taken from a previous study on a similar sample [24]. W_0 and σ were the amplitude and

width of the optical pump pulse, respectively. Lastly, τ_s is the heat transfer time constant from particle to the surrounding (taken from literature [13]), which was assumed to be room temperature.

The last missing parameter for the numerical calculation of $T_{e,l}$ is the initial jump in electron temperature $\Delta T_{el}^{\text{initial}}$, which was calculated from the absorbed energy per pump pulse and unit volume of Au:

$$\frac{I_{\text{abs}}}{N_{\text{AuNP}} \cdot V_{\text{AuNP}}} = \frac{1}{2} \gamma ((\Delta T_{el}^{\text{initial}} + T_{\text{RT}})^2 + (T_{\text{RT}})^2), \quad (5.23)$$

where I_{abs} is the absorbed energy per pump pulse according to Lambert-Beer's Law, N_{AuNP} is the number of AuNPs in the pump beam, V_{AuNP} is the volume of a AuNP, γ is the electron heat capacity for bulk gold and T_{RT} is the room temperature [83].

5.4 Results and discussion

The quality of the AuNP sample used for this study was investigated by UV-Vis spectroscopy and TEM. The UV-Vis spectrum shows a typical form for spherical AuNP with the LSPR center wavelength of 525 nm indicating no aggregation. As described in chapter 3, the particle concentration of the dispersion was determined to be 7.76×10^{12} particles/ml (12.9 nM) from the absorbance at 450 nm. The necessary particle size for this analysis was determined from TEM images as described in chapter 3: (26.9 ± 1.3) nm. Even though the AuNP on the representative TEM images shown in Fig. 5.10 do not appear to be perfectly spherical, the particle size standard deviation indicates a high quality of the sample. Since the preparation of the sample included scaling up the usual protocols by a factor of 6 and multiple centrifugation steps to increase the concentration to an unusual value, particle aggregation and a deteriorating AuNP shape could be expected. In fact, the protocol resulted in multiple failed attempts with AuNP aggregating beyond the possibility of redispersion. How-

ever, considering these difficulties in sample preparation, the sample quality of the batch shown in Figures 5.9 and 5.10 was decided to be sufficient for the SPI and TA experiments.

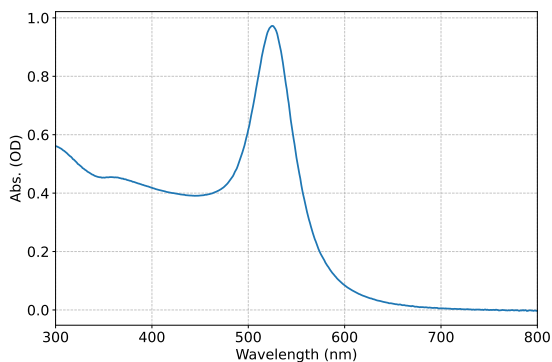


Figure 5.9: UV-Vis spectrum of the AuNP-batch used for this study. Reprinted with permission from Ref. [129]. Copyright 2023 American Chemical Society.

As described in the previous section, the SPI experiment and data analysis resulted in two data sets of particle diameter vs. delay time between optical pump and x-ray probe for different applied fluences (0.7 mJ/cm^2 and 1.8 mJ/cm^2) displayed in Fig. 5.11. The particle diameter transients show an increase in size starting immediately with the optical pulse. However, a breathing oscillation is only observable at a pump fluence of 1.8 mJ/cm^2 . At a fluence of 0.7 mJ/cm^2 only a size increase by roughly 0.02 nm (0.07%) is observed. Generally, the size increases by a maximum of 0.05 nm , which is smaller than gold's atomic radius (0.135 nm , [141]) and much smaller than the diameter standard deviation obtained from TEM (0.8 nm) or the FWHM of the size distribution of the corrected SPI data set (0.62 nm). This speaks to the sensitivity of the experiment, but also commands a certain degree of skepticism about the amplitude of the breathing oscillation. As mentioned above, the binning of particle diameters within 1 ps for each delay time has reduced

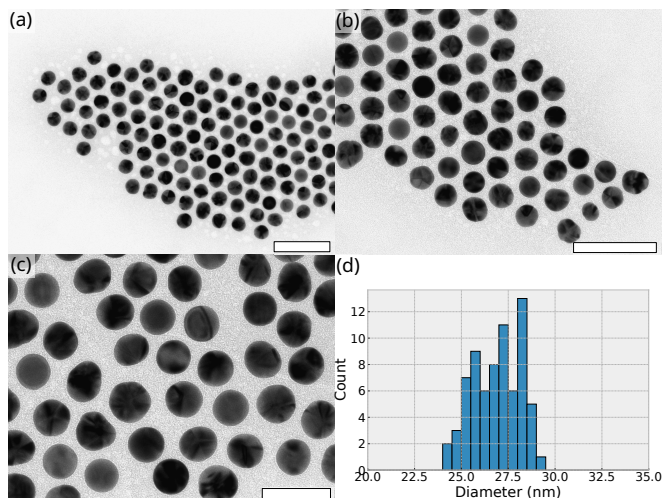


Figure 5.10: a)-c) Representative TEM images of the AuNP-batch used for this study. The white bars indicate 100 nm. d) Size histogram obtained by image analysis of TEM results. Particle diameter: (26.9 ± 1.3) nm. Reprinted with permission from Ref. [129]. Copyright 2023 American Chemical Society.

the amplitude of the resulting diameter-vs-time data and the real increase in size is probably bigger. Calculations by G. Hartland or Bonafé et al. suggest size oscillations in the range of just under 1 % [118, 124]. The reason of the absence of any breathing at low fluence might therefore be the low amplitude of the breathing oscillation in combination with insufficient number of hits during the experiment. However, the data obtained at 1.8 mJ/cm^2 pump fluence clearly shows a full oscillation and will be further analyzed in the rest of this chapter.

Two additional values were plotted in Fig. 5.11: The dotted line is a Gaussian curve indicating the estimated x-ray pulse duration of 120 fs. In combination with the measured optical pulse duration of 80 fs, the time-resolution of the experiment can be estimated to be below 1 ps, which is sufficient to measure the changes observed here. The red line indicates the rise in lattice temperature calculated from the 2TM. The comparison between the diameter and lattice temperature vs. time shows that the first maximum of the diameter is reached well before the maximum lattice temperature as predicted from the 2TM. The observed rise even for the low-fluence SPI data is therefore not a strict thermal expansion of the particle.

We referenced the SPI data with TA studies at the same excitation conditions (wavelength and fluences) to establish the robustness of the SPI data. The results are displayed in Fig. 5.12. Subfigure a) shows TA spectra at the delay time of maximum contrast (0.5 ps). The spectra show the usual form for spherical AuNP, with a bleach signal at the LSPR center wavelength of 525 nm (cf, UV-Vis spectrum in Fig. 5.9) and two positive sidebands. The electron- and lattice temperature were simulated using the 2TM (Fig. 5.12d). Comparing the bleach kinetics (Fig. 5.12c) to the electron temperatures confirms the established picture of the TA contrast's origin. By fitting the breathing oscillation shown in Fig. 5.12b as described in the previous section, the period of the breathing oscillation was determined to be 8.8 ps. The analysis of the breathing mode dephasing yields a standard size deviation of 1.78 nm, which is about 1 nm higher than what was determined from TEM and SPI, but in the same order of magnitude. Especially, the SPI determined size distribution is expected to be smaller, because slightly elliptical particles, which would

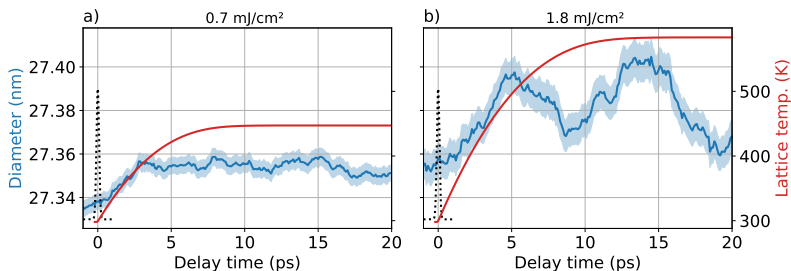


Figure 5.11: Particle diameter obtained from SPI (blue) and lattice temperature calculated from 2TM (red) vs. delay time for the applied fluences of a) 0.7 mJ/cm^2 and b) 1.8 mJ/cm^2 . The blue shadow is the particle diameter standard deviation and the dotted lines the envelope of the optical pulses. Reprinted with permission from Ref. [129]. Copyright 2023 American Chemical Society.

increase the size distribution of the ensemble, were sorted out during data analysis.

Given that SPI is a fairly new technique to study breathing oscillations, we relate the results to the TA kinetics in Fig. 5.13a). Even without adjusting time-zero, the second maximum of the oscillation measured in SPI matches the first resolvable maximum of the breathing oscillation in TA spectroscopy. This confirms the similarity of the underlying effect that leads to the oscillation of the signals and shows the robustness of SPI for studying dynamic structural changes of nanoparticles upon optical excitation.

In order to discuss the breathing mode excitation mechanism, the combined SPI and TA data are compared with the prediction of our newly developed theory presented in section 5.2 (cf. Fig. 5.13a) as well. The theory exactly predicts the excitation behavior of our combined observations, matching both frequency and - more importantly - the phase of the oscillations. Fig. 5.13b shows the prediction of the breathing oscillation if only one of the source terms

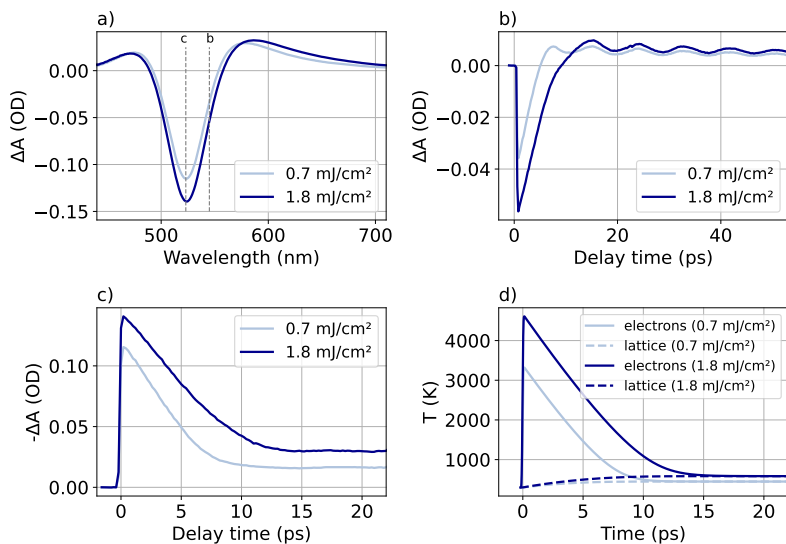


Figure 5.12: TA results for two pump fluences. a) TA spectra at delay time of maximum contrast (ca. 0.5 ps after excitation). Dashed lines mark the probe wavelengths shown in b)-c). b) TA kinetics at probe wavelength of 545 nm. c) TA kinetic obtained by tracing the bleach minimum. d) Electron and lattice temperatures calculated from 2TM. Reprinted with permission from Ref. [129]. Copyright 2023 American Chemical Society.

is used with the respective prefactors of the combined calculation. The comparison between the purely thermal and purely electron density gradient produced oscillations show the importance of the new excitation source, which dominates over the $[T(t) - T_0]$ -sourced oscillation at the onset, thereby shifting the overall phase.

To further investigate the phase behaviour of the newly developed theory, fluence dependent TA measurements are compared to the predicted breathing oscillations in Fig. 5.14. Once again the theory predicts the fluence dependency of the breathing oscillation very well. Both the TA results and the overall theoretical breathing oscillation lack a strong fluence dependence of the breathing mode phase. Distinguishing between the contributions of the two source term reveals a key difference in this regard. The $\nabla\rho_2^e(\mathbf{r}, t)$ -sourced oscillations lack any fluence dependence as they depend on the square of the electric field (cf. Eq. 5.15). In contrast, the $[T(t) - T_0]$ -sourced predicted oscillation very clearly shows a fluence dependence, because the initial electron temperature after excitation depends on the deposited energy. This comparison supports the dominant role of the electron density gradient in the breathing mode excitation again.

Overall, we have successfully measured the breathing mode of AuNP after optical excitation using SPI, thereby providing critical information about the onset of the oscillation, that is inaccessible by TA. This technique - pending further improvements to increase the number of recorded patterns - will be useful to further investigate breathing oscillations in nanoparticles - in particular anisotropic structures, which show more complicated modes. Theoretically, the inclusion of the electron density gradient in describing the onset of the breathing oscillation contributes a source term, which accelerates the initial rise of the particle expansion during the first breathing mode period. Simply describing the excitation of breathing modes excitation as an ultra-fast heating of the lattice is insufficient. This problem was solved in previous studies only by using the phenomenological hot-electron pressure [45] or other direct interactions between electrons and lattice [48, 49, 124]. In contrast, the influence of the electron density gradient on the excitation of the breathing oscillation evolved naturally from our calculations. Therefore, one might think

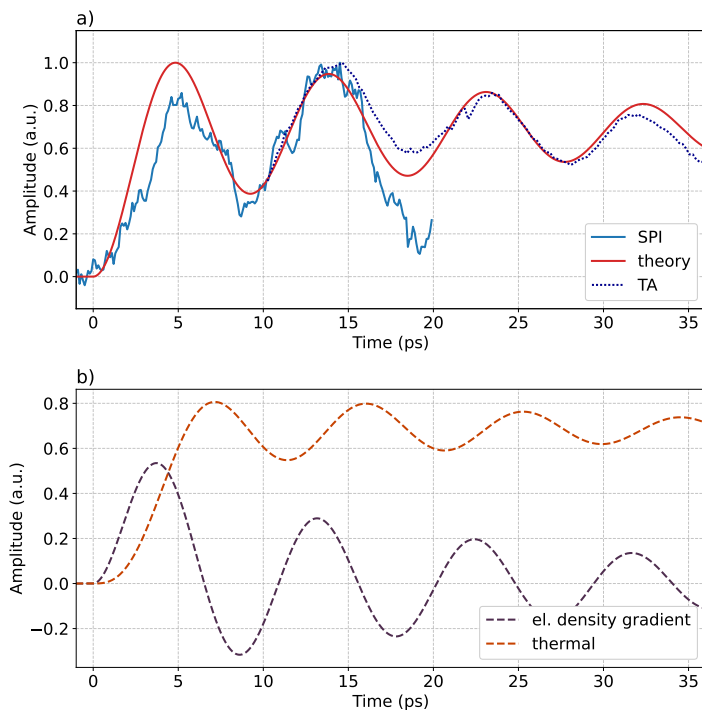


Figure 5.13: a) Experiments-theory comparison. The TA kinetic was only plotted starting at a delay time of 10 ps for clarity (the first 10 ps of the kinetic are dominated by the hot-electron dynamics). b) Comparison of expected breathing oscillation from theory if only the electron density gradient or thermal energy transfer are used as sources, respectively. Reprinted with permission from Ref. [129]. Copyright 2023 American Chemical Society.

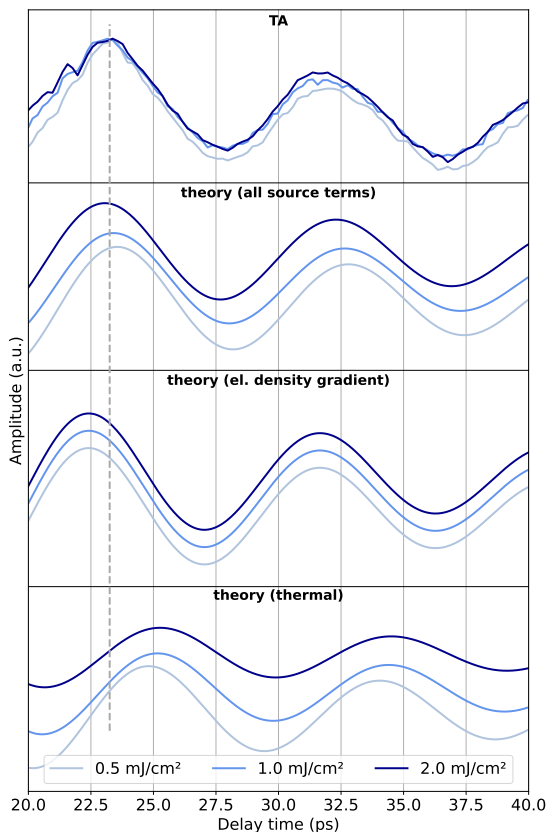


Figure 5.14: Comparison of fluence-dependent phase behavior of the breathing oscillation. Top row: TA results. Bottom three rows: theoretical predictions (2nd row: all source term used. 3rd row: only electron density gradient used as source term. The amplitude offset was artificially implemented for clarity. 4th row: only thermal contribution used as source term.) Reprinted with permission from Ref. [129]. Copyright 2023 American Chemical Society.

of the new source term as a new microscopic description of the direct excitation mechanism.

Chapter 6

Hot electron dynamics of hybrid Au-Pt superlattices

The work presented in this chapter was a collaborative effort by the groups of Emiliano Cortés at Ludwig-Maximilians-Universität Munich, Germany (), Stephanie Reich at Freie Universität Berlin (§) and Holger Lange at Universität Hamburg (&). Florian Schulz (&) synthesized the nanoparticles, produced the superlattices and recorded the TEM images. Sabrina Jürgensen (§) was responsible for the characterization of the sample by optical microscopy and micro-transmission/-reflection spectroscopy and conducted the FDTD simulations. Matias Herran (*) conducted and analyzed the photocatalysis experiments. The TA experiments and analysis are my contribution.*

Between submission and publication of this work the study has been published in the following article:

M. Herran, S. Juergensen, M. Kessens, **D. Hoening**, A. Köppen, A. Sousa-Castillo, W.J. Parak, H. Lange, S. Reich, F. Schulz, E. Cortés, Plasmonic

Bimetallic Two-Dimensional Supercrystals for H₂ Generation, *Nature Catalysis*, **6**, 1205-1214, (2023),
<https://doi.org/10.1038/s41929-023-01053-9>

A key motivation of studying the plasmonic properties of AuNPs is the sensitivity of the LSPR to its surroundings. For analytics, SERS comes to mind as an established experimental method that utilizes this property. Techniques like SERS profit from the extremely high local electric fields produced by the LSPR. The plasmonic near-field scales with $1/\text{distance}^3$ [1], which localizes the SERS enhancement to the particle's surface.

The plasmonic near-field also influences other AuNP, if they are in close proximity to each other. This results in plasmon coupling, observable as a red-shift of the LSPR [99]. A straight-forward model to explain plasmon coupling is analogous to the linear combination of atomic orbitals. Just like hybrid molecular orbitals form upon bringing two atoms close to each other, plasmon coupling can be described as the formation of a hybridized plasmon state, which is lower in energy than the LSPR of individual particles. In this case, both plasmon resonances oscillate in phase and produce a highly intense electric field localized at the particle gap [1], called a 'hot spot'. Theoretically, a higher-energy antiparallel plasmon mode exists as well, however due to the vanishing dipole moment it can not couple to the far field and is thus termed a "dark" state [142].

In principle, this should also apply to multiple layers of AuNP within the quasi-static approximation. If, however, there is a gradient in the electric field across the multilayers, new plasmon-polariton modes emerge, which have properties exclusive to AuNP superlattices. These new plasmon modes were studied and described by Mueller et al. and a first study on the hot-electron dynamics of these systems has been published by myself as well [11, 12, 50, 143].

Currently, the development of hybrid AuNP superlattices is in progress - incorporating other species with additional functionality. Combining the plasmonic and hot-electron properties of AuNP superlattices with catalytic materials is a promising pathway for bridging the gap between fundamentals and appli-

cations. The study presented in this chapter seeks to explore the hot-electron dynamics of a hybrid AuNP-PtNP ('Au-Pt') superlattice in the context of photocatalysis. Our collaborators studying the photocatalytic properties of this system, have found a peak in activity at the excitation wavelength leading to the highest electric field intensities in the particle gaps. The goal of this work is to explore the electron dynamics of the hybrid superlattice and contribute to the understanding of the enhancement's origin. For that, the hot electron dynamics were determined using TA spectroscopy. The results were compared to the dynamics in a pure AuNP superlattice and a solution of PtNP.

First, the AuNP superlattice's properties will be summarized followed by additional background on hybrid plasmonic systems and their hot-electron dynamics. Afterwards we turn to the preparation of such hybrid superlattices and finally the TA study on the hybrid Au-Pt superlattice will be presented.

6.1 Properties of AuNP superlattices

6.1.1 Plasmon-polariton modes and ultrastrong light-matter coupling

The preparation of AuNP superlattices using the wet-chemical approach described later in this chapter yields a face-centered cubic assembly, which was studied by means of optical and NIR transmission and reflection spectroscopy by Mueller et al. [11, 143]. The spectra revealed new absorption bands in the near-IR in addition to the interband absorption starting at 520 nm, with high reflectance in between. The number and position of the new absorption bands depended on the number of layers (cf. Fig. 6.1c). The results were then rationalized by a theoretical model that includes a quantum-mechanical formalism to obtain the dielectric function of the supercrystal and a microscopic theory, which yields the dispersion relation of the plasmon-polariton modes [11, 144].

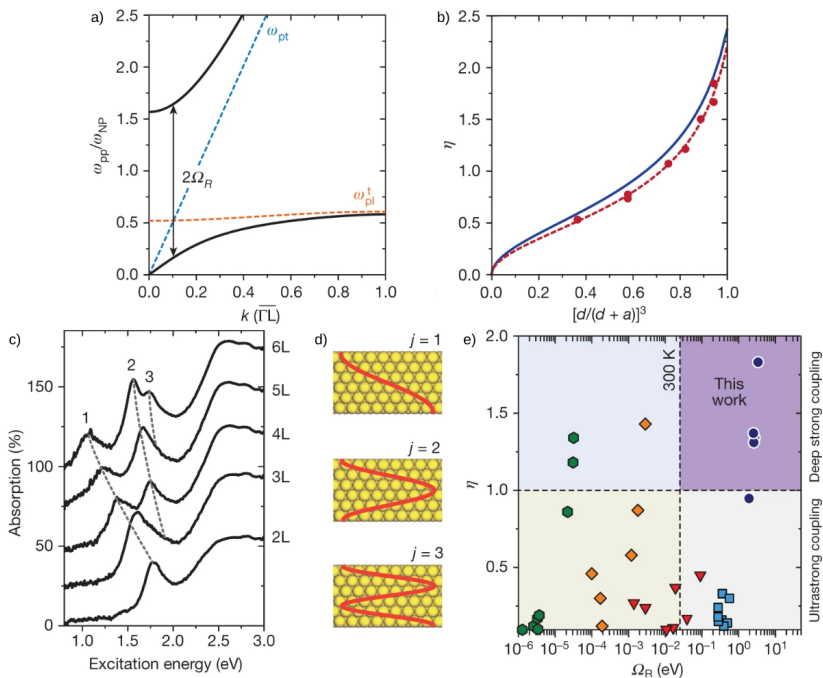


Figure 6.1: Optical properties of AuNP superlattices. **a)** Plasmon-polariton dispersion. **b)** Normalized light-matter coupling factor depending on the fill factor. **c)** Absorption features resulting from increasing number of AuNP layers. **d)** Illustration of plasmon-polariton excitations as standing waves within the layers. **e)** Normalized light-matter coupling factor vs. Rabi frequency reveals deep strong coupling. Reprinted from [11] with permission from Springer Nature.

The formalism models the supercrystal as an infinite array of spheres, which interact through dipole-dipole interactions - the dipole moment of an individual sphere being in its center coordinate. Based on these models and simulations the special optical properties of the superlattices could be explained. These are governed by transverse plasmon-polariton modes, which are unique to this type of platform and reveal a couple of interesting phenomena.

From the level of anti-crossing in the dispersion relation shown in Fig. 6.1a it was determined, that the superlattices exhibit deep-strong light-matter coupling with a normalized coupling factor η exceeding previously reported values for various systems (Fig. 6.1e). The coupling factor depends on the fill factor in the lattice and thus on the particle size-to-gap ratio $\left(\frac{d}{d+a}\right)^3$ with higher values leading to stronger coupling (Fig. 6.1b). One of the effects of ultra-strong light matter coupling is the breakdown of the Purcell effect [145]. The Purcell effect describes the increased spontaneous emission of an emitter in a cavity due to light-matter coupling. However, as light-matter coupling increases this effect reverses. As a result, the deep-strong light-matter coupling leads to narrowing and increased intensity of the absorption bands.

The plasmon-polariton modes form standing waves across the crystal, which acts as an open cavity. With increasing thickness of the material, i.e. increasing number of AuNP layers, higher-order modes are possible leading to additional absorption peaks (Fig. 6.1c-d). The position of these peaks could be successfully modeled as simple dipole-dipole interactions even though the large fill factor would contradict the underlying quasi-static approximation [11].

Because the superlattice's properties depend on numerous controllable parameters such as particle size, gap between the particles and the dielectric medium, it may serve as an excellent, tunable platform for applications utilizing plasmonic materials. In a following publication, Mueller et al. have shown a manifold enhancement in SERS, which can be attributed to the high density of hot spots within the superlattice [41].

Principle of superlattice assembly

The preparation of nanoparticle superlattices throughout this work is based on evaporation-induced self-assembly on a liquid sub-phase as demonstrated by Dong et al., who have prepared binary superlattices consisting of Fe₃O₄ and FePt nanoparticles [146]. The protocol was further adapted for the preparation of AuNP and AuNP-PtNP superlattices by Schulz et al. in the context of studying the emerging plasmon-polariton modes described above [12, 147]. The straight-forward principle is illustrated in Fig. 6.2. A nanoparticle solution in a volatile solvent is pipetted onto a liquid sub-phase, which is not miscible with the particle solution, in a Teflon well. The solvent of the nanoparticle phase then slowly evaporates, which induces the self-assembly of the particles into a superlattice sitting on top of the liquid sub-phase. The assembly into well ordered lattices is aided by slowing down the evaporation rate of the solvent through covering the well with a glass slide. Once the solvent has completely evaporated, the superlattice can be transferred onto a substrate of choice.

As mentioned in the previous section, the properties of the superlattices depend on the fill fraction of the AuNP. Hence, careful control of the particle-to-particle gap in the lattice is crucial. For that, grafted polymers - in this work PSSH - are used as stabilizing agents. By choice of the molecular weight of the polymer in relation to the particle size, the gap size can be adjusted. Schulz and Lange have shown, that the model to describe the gap scaling with molecular weight depends on the particle size: For AuNP up to about 50 nm in diameter the gap scales with molecular weight of the polymer, i.e. longer polymer chains lead to larger gaps. For larger particles, however, the polymer acts more like soft matter and their volumetric density as well as the grafting density controls the gap size [147]. To date, the number of nanoparticle layers is only rudimentarily controlled through the number of particles in the solution. While single and bilayers can be routinely obtained, ≥ 3 layered superlattices often yield a mix of multiple domains with varying layer number [12].

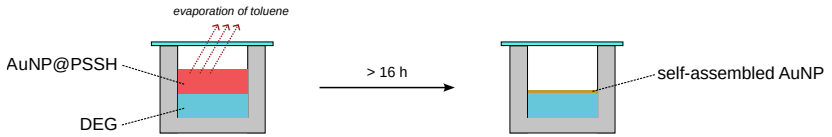


Figure 6.2: Illustration of the evaporation induced self-assembly of AuNP at a liquid-liquid interface.

To prepare binary lattices, a mixture containing both nanoparticle species is pipetted onto the liquid subphase. To avoid phase-separation of the particles during evaporation, the relative sizes of the species are adjusted. For the Au-Pt superlattice studied in this work, the PtNP sit in the particle gaps of a AuNP lattice and thus have to be much smaller in size.

6.1.2 Hot-electron dynamics of AuNP superlattices

Previous to the work conducted for this thesis, we have investigated the hot electron dynamics of a AuNP superlattice (particle diameter: 42 nm, gaps: 4 nm) with varying number of layers. The results were published in my Master thesis as well as a research paper in the Journal of Chemical Physics [50]. As the hot electron dynamics of a pure AuNP superlattice will serve as a benchmark for the hybrid lattice later in this chapter, this study shall be briefly revisited here.

A series of TA measurements were performed on three spots with varying number of AuNP layers. One spot consisted only of a monolayer and therefore did not exhibit the plasmon-polariton modes presented in the previous section while the two other spots contained an increasing number of layers. While the excitation power was held constant, the excitation wavelength was varied to screen the visible-to-NIR spectrum of the films. The e-ph coupling time at these spots was determined from fitting the bleach dynamics in the visible spectrum with a bi-exponential function. The fast decay constant was interpreted as the e-ph coupling time. The results were related to the absorbance

spectra of the different number of layers simulated using FDTD, which were in turn verified by NIR microabsorbance measurements on the same film.

The resulting e-ph coupling times displayed in Fig. 6.3a show an increase at those wavelengths where plasmon-polaritons are excited in the multilayers in comparison to the monolayer ($\lambda_{\text{pump}} > 700 \text{ nm}$). Therefore, the e-ph coupling times follow the differences in absorbance between the layers (cf. 6.3b). Note that the plasmon resonance in the visible was analyzed.

The simulated spectra displayed in Fig. 6.3b did not show a “single-particle” mode that would lie in the visible. The fact that a LSPR in the visible could be measured in TA was probably the result of sample inhomogeneity within the illuminated superlattices, but the reason why these can be routinely observed in TA on superlattices (as we will see later in this chapter) could not be fully resolved to this day.

Exciting the different layers at the wavelength at which the bleach dynamics were measured (ca. 600–650 nm), yielded the same e-ph coupling times for all spots with values similar to those obtained for exciting the plasmon-polariton modes in multilayers. There might be a slight increase in e-ph coupling times upon excitation of the plasmon-polariton modes, but these differences are within the expected uncertainties of the measurements. The e-ph coupling times thus follow the absorbance of the respective superlattices. The occurrence of additional absorption bands due to the formation of plasmon-polariton in the near-IR translates to increased hot-electron generation.

One could expect the excitation of plasmon-polariton modes to yield increased e-ph coupling times relative to the excitation of the LSPR in single AuNP, because the breakdown of the Purcell effect suppresses their radiative damping and for a given excitation fluence per Au volume, more energy would be deposited into the hot electron distribution as a result. Within the accuracy of the TA measurements, however, the difference might not be significant enough to be observed. Since the exact illuminated unit volume of Au in a superlattice is difficult to ascertain, a direct comparison of the hot electron dynamics be-

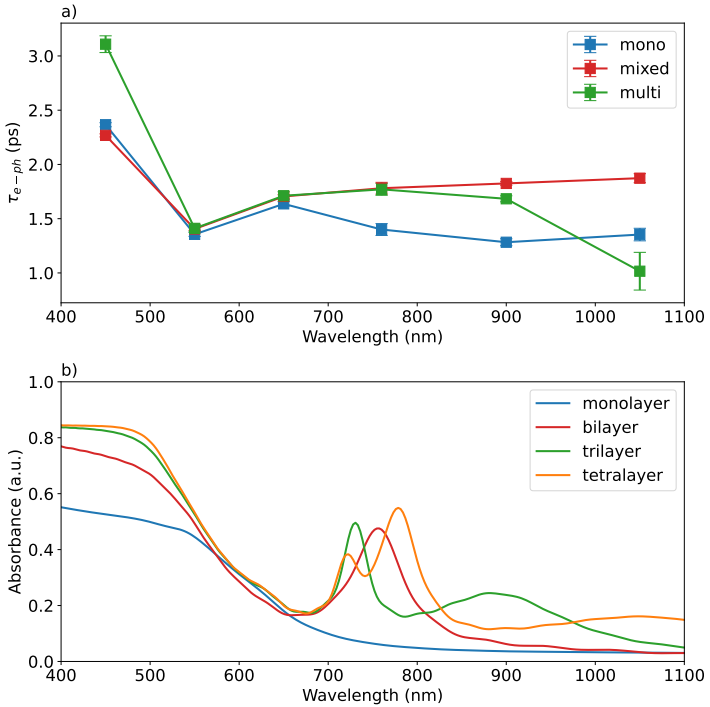


Figure 6.3: **a)** E-ph coupling times in AuNP superlattices depending on the excitation wavelength for different spots with varying amount of multilayers. Spot "mono" consisted of a single AuNP layer. Spot "mixed" consisted of 67 % monolayers, 23 % bilayers and 10 % of ≥ 3 layers. Spot "multi" consisted of 21 % monolayers, 16 % bilayers and 63 % of ≥ 3 layers. **b)** Simulated absorbance spectra of superlattices of 42 nm AuNP with 4 nm gaps. Reprinted from [50] with the permission of AIP Publishing.

tween the excitation mechanisms LSPR and plasmon-polaritons remains challenging.

6.2 Hot electrons and hybrid systems for photocatalysis

One of the main motivations in studying the hot-electron dynamics of plasmonic systems is the possible utilization of the charge carriers in photocatalysis. Since noble metal nanoparticles are usually inert, many strategies have been developed to aid the photochemical reactivity by combining plasmonic materials with more reactive agents like adsorbates, semiconductors or other metals. A wide variety of combinations have been proposed both in terms of materials and how intimately they are connected, ranging from metal alloys, to core-shell nanoparticles, connected nanoparticle combinations and disconnected, but proximate materials. For a comprehensive overview, the reader is referred to a review by Zhang et al. and the references therein [90].

The type of materials and connection also govern the electron dynamics of these systems. Energy might be transferred from a plasmonic to a catalytically active material or directly into an adsorbate via the plasmonic near-field, direct or indirect transfer of hot electrons, or local heating. For example, Seemala et al. have demonstrated for silver nanoparticles, that the strong and highly localized plasmonic near-field affects the energy of antibonding states in an adsorbed molecule, leading to its dissociation [148]. Furthermore, Rodio et al. have studied the photocatalytic activity of AuNP for a glucose oxidation and have found evidence for the contribution by non-thermal electrons to the reaction [149]. In a recent publication Vanzan et al. have used real-time time-dependent density functional theory to calculate the energy transfer from hot electrons to vibrational states of adsorbed molecules. The exact modes excited by the hot electrons were specific to the type of plasmonic material and adsorbed molecule [150]. Using TA spectroscopy Cushing et al. have found a resonant energy transfer from the plasmonic excitation in AgNP to the ab-

sorption in a TiO₂ shell, which leads to photocatalytic enhancement [151]. The group of Naomi Halas has introduced the idea of antenna-reactor geometries, which combine the light-harvesting properties of plasmonic nanoparticles with the catalytic properties of typical transition metals [36, 152]. The transfer of hot electrons from the plasmonic to the catalytic material can in principle occur via a direct or indirect mechanism: either hot electrons are generated within the plasmonic material and due to their increased energy overcome the energy barrier into the catalyst, or they are directly excited from the plasmonic into the catalytic material [153].

The role of hot electrons can be determined using TA spectroscopy. In particular the transfer of hot electrons to an adjacent material would alter the ultrafast optical dynamics. The employment of hot electrons in photocatalysis is limited by their fast relaxation time. Hot electron injection into other materials would have to be faster than the relaxation in order to contribute significantly to the electron dynamics. Hence, one would expect a faster relaxation time of the hot electron signature in TA. For example, Engelbrekt et al. have found a faster decay of the plasmon broadening upon loading AuNP surfaces with smaller PtNP, which was attributed to the energy transfer between hot electron distributions in Au and Pt [92]. Nezemi et al. have attributed the faster decay of ΔA in a AuNR-Pd hybrid system to increased hot-electron transfer from Au to Pd after redistribution of Pd on the AuNR surface [154]. Zhang et al. found the same for spherical Au-Pd core-shell particles [155]. The same principles can be applied to AuNP-semiconductor combinations as well: Ghorai et al. have studied AuNP-SiO₂-TiO₂ using TA. Here, increasing the relative amount of the electron accepting TiO₂ in a mixed SiO₂-TiO₂ shell led to a decreasing decay time of the TA signal - suggesting an electron transfer from the light-harvesting AuNP to the semiconductor [108]. In an earlier study of AuNP-TiO₂ by IR-probe TA spectroscopy, Furube et al. found a hot electron injection time of a few hundred femtoseconds, which is one order of magnitude faster than e-ph coupling times in AuNP [156].

From these considerations of the hot electron dynamics in antenna-reactor geometries, one could expect hot-electron transfer from AuNP to PtNP to occur in the hybrid superlattices studied in this work. These charge carriers could

then contribute to the catalytic properties of the PtNP. In that case, the TA dynamics would reveal an accelerated decay of the AuNP bleach signal. In contrast, photocatalytic enhancement due to the influence of hot spots in the gaps of the hybrid lattice would not alter the electron dynamics in the AuNP.

6.3 Experiments

As mentioned at the beginning of this chapter, the study presented here was not yet published by the time of submission and hence contains descriptions of all the experimental procedures that led to the results presented afterwards - not just the work done by myself - to ensure reproducibility of the results regardless of the publication status of the study.

6.3.1 Transient absorption spectroscopy

TA spectra were recorded using the setup described in chapter 3. Three samples were investigated: The AuNP-PtNP superlattice, a AuNP superlattice - both deposited on borosilicate glass (BSG) substrates - and a PtNP solution in a 2 mm quartz cuvette. Three pump wavelengths were chosen for the films: 400 nm, 500 nm and 650 nm and two wavelengths for the solution: 300 nm and 650 nm. For all measurements, a single pump power of $150 \mu\text{J}/\text{cm}^2$ was selected. All samples were probed in the visible spectrum. The delay times were chosen between -1 ps and 20 ps and for each delay time, the spectrum was averaged for 1 s. Each measurement consisted of 3 scans, which were averaged to yield the raw data. These were corrected for chirp and scattered light.

For data analysis, the TA spectra at time of maximum contrast (delay time = 0 ps) were extracted. In case of the films, these were normalized to their bleach signal. To study the hot electron dynamics, kinetics at two probe wavelengths were analyzed: 420 nm and the wavelength of the bleach.

Additionally, a single NIR-probe TA measurement was performed on the AuNP superlattice. The pump wavelength was 450 nm, a delay time window of -1 ps to 51 ps was scanned with an averaging time of 1 s per delay time. Only a single scan was measured. The data were used for further analysis without chirp correction. In contrast to visible-probe TA measurements presented in this work, differential spectra were not recorded in reference mode, i.e. there was no correction of the white-light intensity.

6.3.2 Superlattice assembly

AuNP@PSSH preparation: PSSH-stabilized AuNP were prepared by synthesizing AuNP@CTAC as described in chapter 3 and a subsequent ligand exchange from CTAC to PSSH. Before ligand exchange, excess CTAC was removed from the AuNP@CTAC solution by centrifugation and the volume of the solution was thereby reduced to $\leq 100 \mu\text{L}$. This solution was then added drop-wise to a PSSH in THF solution (2 ml, 0.5 mM), which was rapidly stirred at 1000 rpm. The mixture was further stirred at 300 rpm overnight for replacement of CTAC with PSSH. This led to the transfer of the AuNP into the THF phase, which was then dried in a rotary evaporator. The remaining AuNP@PSSH were redispersed in toluene and excess PSSH was removed by two centrifugation steps. Remaining CTAC was removed by washing the solution with water and ethanol in a 1:1:1 mixture with addition of sodium chloride to aid phase separation. The AuNP in toluene phase was removed and centrifugated to obtain the final concentration needed for self-assembly [12].

PtNP@PSSH preparation: PtNP@citrate were prepared based on a protocol from Ref. [157]: Ultrapure water (8.6 ml) and hexachloroplatinic acid H_2PtCl_6 (500 μL , 0.05 mM) were mixed and sodium citrate (500 μL , 0.1 mM) was added for stabilization of the nanoparticles. These were formed by reduction of the Pt precursor with NaBH_4 (500 μL , 0.015 mM). The solution was stirred throughout at 500 rpm and left undisturbed for 10 minutes. 1000 μL of this solution was then directly used for a ligand exchange by mixing it with 1100 μL PSSH-2k (0.18 mM, in toluene) and 1000 μL ethanol. The solution

was thoroughly shaken and a few mg of sodium chloride was added to aid phase separation [158]. The PtNP-containing toluene phase was removed and used for assembly as is.

Self-assembly: For self-assembly of the AuNP and AuNP-PtNP superlattices, a solution of

AuNP@PSSH or a mixture of AuNP@PSSH and PtNP@PSSH was pipetted onto a DEG phase in a Teflon well. The well was covered with a glass slide to slow down the evaporation of toluene. Within 16-24 hours all toluene has evaporated and the lattices have formed on the DEG phase. These were then transferred for further experiments and characterization onto different substrates (indium tin oxide (ITO) for photocatalysis, copper grid for TEM and BSG slide for TA).

6.3.3 Photocatalysis

The catalytic reactions were carried out in a 1 ml reactor with a flat quartz window and a water jacket for temperature control ($dT = \pm 0.5\text{ }^{\circ}\text{C}$). The reaction time was 1 h and the mixture was stirred at 550 rpm using a magnetic bar. Prior to the reactions, the H_2O was degassed using N_2 for 30 min. As an excitation source a commercial broadband arc lamp (Newport 66921) was used and bandpass filters were employed to block UV and IR radiation (broadband excitation) or to select narrow bands (450 nm, 550 nm, 650 nm, 750 nm and 800 nm with 20 nm bandwidth). The excitation power was set to 5 mW and corrected accordingly for all employed wavelengths. The H_2 production was measured via gas chromatography using a Perkin Elmer Clarus 590 GC equipped with a thermal conductivity detector (TCD) for H_2 detection and a flame ionization detector (FID) for detection of organic traces. The FID was also coupled to a H_2 generator from Perkin Elmer (NM plus H2 100).

For normalization of the H_2 production, the catalyst masses were measured via Inductively Coupled Plasma - Mass Spectrometry (ICP-MS) using an Agilent 7700. Calibration curves were obtained using elemental standards from Carl

Roth, Germany. The lattices on ITO were dissolved in 200 μl freshly prepared aqua regia overnight and then diluted to 4000 μl with 2% hydrochloric acid. The platinum concentration was obtained by drying 50 μl of the dispersion on an ITO substrate and then dissolving it in 240 μl aqua regia with subsequent dilution to 2500 μl using 2% hydrochloric acid. From the determined concentrations of the species, the catalyst and Pt masses were calculated.

6.3.4 Optical micro-transmission and -reflection spectroscopy

Transmission and reflection spectra of the lattices were recorded using a home-built setup as described in Ref. [159]. A supercontinuum laser (NKT - FIU15) produced broadband visible light, which was guided into an inverse microscope (Olympus IX71). The light was focused onto the sample with a 100x objective (NA = 0.9). The transmitted light was collected using another 100x objective (NA = 0.8) and guided to a spectrometer (Avantes - AvaSpec 3648) via optical fiber. The reflected light passed two beamsplitters before it was collected by a lens and guided to the spectrometer via optical fiber as well. From the transmitted (T) and reflected (R) light, the absorbance was calculated as $A = 100\% - R - T$.

6.3.5 Finite-difference time-domain simulations

Finite-difference time-domain (FDTD) simulations were carried out using the commercial Lumerical FDTD Solutions software package, implemented similarly as in Refs. [11, 159]. A hexagonal lattice of 22 nm AuNP with 2 nm was simulated. For the hybrid lattice the gap size was increased to 3.5 nm and 3 nm PtNP were placed in the gaps. Calculations were performed for 1-3 layers stacked in "abc" configuration. The cell size of the mesh was set to 0.2 nm. The dielectric function for gold and platinum were obtained by fitting the data reported in [160] and [161], respectively, and for the dielectric medium (polystyrene) a dielectric constant of $n = 1.4$ was set. The simula-

tions were performed for a lattice unit cell with periodic boundary conditions. As excitation source, a broadband plane wave traveling along the z-coordinate was employed and to simulate unpolarized light, two measurement with linear polarization along x and y were performed and averaged. For the electric field enhancement presented below, the average field of the top layer was taken.

6.3.6 Materials

Tetrachloroauric(III) acid ($\geq 99.9\%$ trace metals basis), hexadecyltrimethylammonium bromide (CTAB, $\geq 98\%$) and chloride (CTAC, $\geq 98\%$), L-ascorbic acid (reagent grade), chloroplatinic acid solution (8% wt. in H₂O), sodium citrate trihydrate ($\geq 99\%$), sodium borohydride ($\geq 98\%$) and indium tin oxide (ITO) coated glass slides (surface resistivity $8 \Omega/\text{cm}^2$ to $12 \Omega/\text{cm}^2$) were purchased from Sigma-Aldrich (USA). Toluene ($\geq 99.5\%$), tetrahydrofuran ($\geq 99.5\%$) and ethanol (denat., $> 98\%$) were purchased from VWR (USA). Diethylene glycol (DEG, reagent grade) was purchased from Merck (Germany). Thiolated polystyrenes (PSSH, PSSH2k: $M_N = 2000 \text{ g/mol}$, $M_W = 2300 \text{ g/mol}$; PSSH5k: $M_N = 5300 \text{ g/mol}$, $M_W = 5800 \text{ g/mol}$; PSSH10k: $M_N = 11\,500 \text{ g/mol}$, $M_W = 12\,400 \text{ g/mol}$) were purchased from Polymer Source (Canada). All reagents were used without further treatment. H₂ standards (100 ppm, 500 ppm and 1000 ppm) were purchased from Linde Gas. Ultrapure water with resistivity of $18 \text{ M}\Omega\text{cm}$ was used in all experiments.

6.4 Results

6.4.1 Samples

Three samples were prepared: A AuNP supercrystal, a Au-Pt supercrystal and a Pt control. These were deposited on ITO for the measurements of the catalytic performance, copper grids for TEM analysis or BSG substrates for TA

spectroscopy. Fig. 6.4 shows representative TEM images of the superlattices employed for photocatalysis. The AuNP were highly spherical and had a diameter of (22.0 ± 1.0) nm. The PtNP were spherical, but less uniform than the AuNP, and had a diameter of (2.7 ± 0.6) nm. The absorbance of PtNP in solution and the AuNP-PtNP mixture used for self-assembly are displayed in Fig. 6.5a. Taking TEM images on different sites of the hybrid lattice confirmed that the PtNP were homogeneously distributed in the gaps between the AuNP and did not form separate phases. Their introduction into the AuNP lattice increased the AuNP-AuNP gaps from 3.0 nm to 3.5 nm.

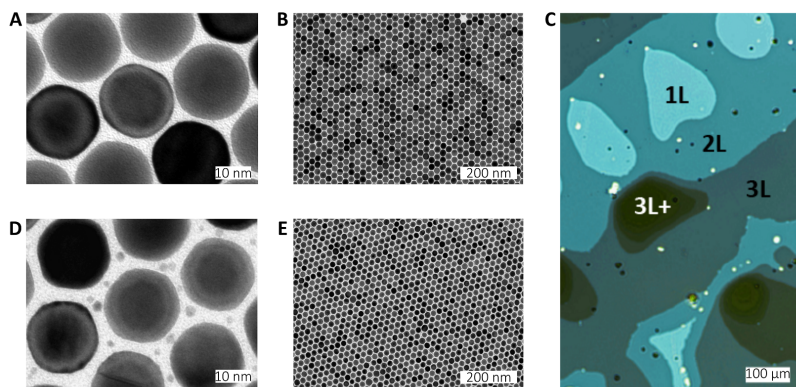


Figure 6.4: **A-B** TEM images of the AuNP superlattice used for photocatalysis measurements. The AuNP are (22.0 ± 1.0) nm in diameter and assembled into a hexagonal superlattice with 3 nm distance between the particle surfaces. **C** Representative optical microscopy images of the AuNP superlattice. The differences in transmission can be used to identify the layer numbers (1L, 2L, 3L, 3L+ indicate mono-, bi-, tri- and multi-layers, respectively). **D-E** TEM images of a hybrid AuNP-PtNP superlattice. The same 22 nm AuNP were used to produce the hexagonal lattice and the (2.7 ± 0.6) nm PtNPs assemble in the AuNP gaps [162].

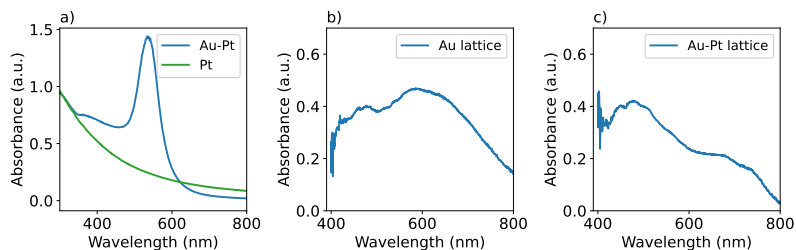


Figure 6.5: Absorbance spectra of **a)** AuNP-PtNP mixture used for self-assembly (blue) and PtNP in solution (green), **b)** the AuNP superlattice (weighted according to occurrence of layers), **c)** the Au-Pt superlattice (weighted according to occurrence of layers) [162].

In addition to electron- and optical microscopy, the lattices were also characterized by means of optical micro-transmission and -reflection spectroscopy. From the transmission and reflection spectra, the absorbance was calculated. The setup allowed characterizing the optical behavior of different layer numbers, which were then weighted according to the occurrence of the layer numbers within the whole sample. These weighted spectra are displayed in Fig. 6.5b-c. While the pure AuNP superlattice absorbed more light throughout the visible spectrum, both Au and Au-Pt superlattices display broad absorption features due to the mix of layer numbers shifting the plasmonic absorption bands towards longer wavelengths. While the absorbance of the pure AuNP lattice shows a broad peak centered around 600 nm, the Au-Pt superlattice absorbs most around 500 nm with decreasing absorbance towards longer wavelengths.

6.4.2 Photocatalytic properties

The Au-Pt superlattice forms an antenna-reactor geometry. Its catalytic properties were tested for a formaldehyde (HCOOH, FA) decomposition reaction: $\text{HCOOH} \longrightarrow \text{H}_2 + \text{CO}_2$. For a dark-vs-illuminated comparison, the samples

were excited using a broadband lamp with bandpass filters blocking any UV and IR radiation. The temperature of the reaction body was set to 25 °C and the reaction yield was determined by gas chromatography.

Figure 6.6 shows the hydrogen production of the samples normalized to the amount of catalyst and time. The Au-Pt superlattice clearly shows an increased hydrogen production upon illumination, which is not the case for the Au lattice. Upon illumination, the Au-Pt superlattice also shows superior hydrogen production compared to only platinum. Temperature-dependent measurements of the reaction yield, which were analyzed to give the activation barrier according to the Arrhenius equation, show a similar trend: The Au lattice without illumination has the highest activation barrier (40.7 kJ/mol) followed by the hybrid lattice without illumination (34.4 kJ/mol) and the hybrid lattice with illumination (29.8 kJ/mol). These results demonstrate the importance of the interaction of AuNP and PtNP since no single component reaches the same catalytic activity under illumination as the hybrid system.

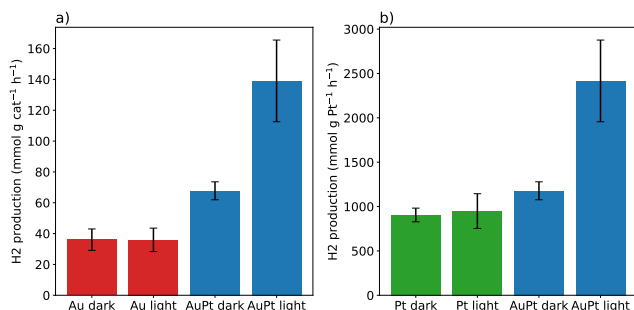


Figure 6.6: Comparison of the hydrogen yield in the photocatalytic reaction between the samples and illumination levels. **a)** and **b)** differ in their normalization: The yield in **a)** was normalized to the mass of Au and Au/Pt (“catalyst”), respectively, while in **b)** it was normalized to the Pt mass [162].

AuNP absorb visible light much better than PtNP. The local electric field produced by the optical excitation of the AuNP then excites the PtNP, which serve

as the catalytic sites. To seek further evidence for this catalytic mechanism, wavelength dependent measurements of the catalytic activity were conducted. According to FDTD simulations, the intensity of the electric hot spots forming in the gaps of the AuNP superlattice is wavelength dependent (cf. Fig. 6.8) and limited to the top-most layer. Figure 6.7 shows that although the absorbance dominated by the AuNP is highest on the short-wavelength side of the visible spectrum the field enhancement by the plasmonic near-field is strongest at 650 nm. The wavelength dependent reaction yield follows the wavelength dependence of the local field enhancement.

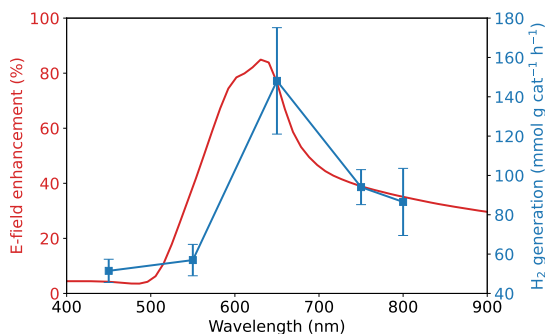


Figure 6.7: Measured hydrogen yield depending on the excitation wavelength related to the local E-field enhancement simulated by FDTD simulations [162].

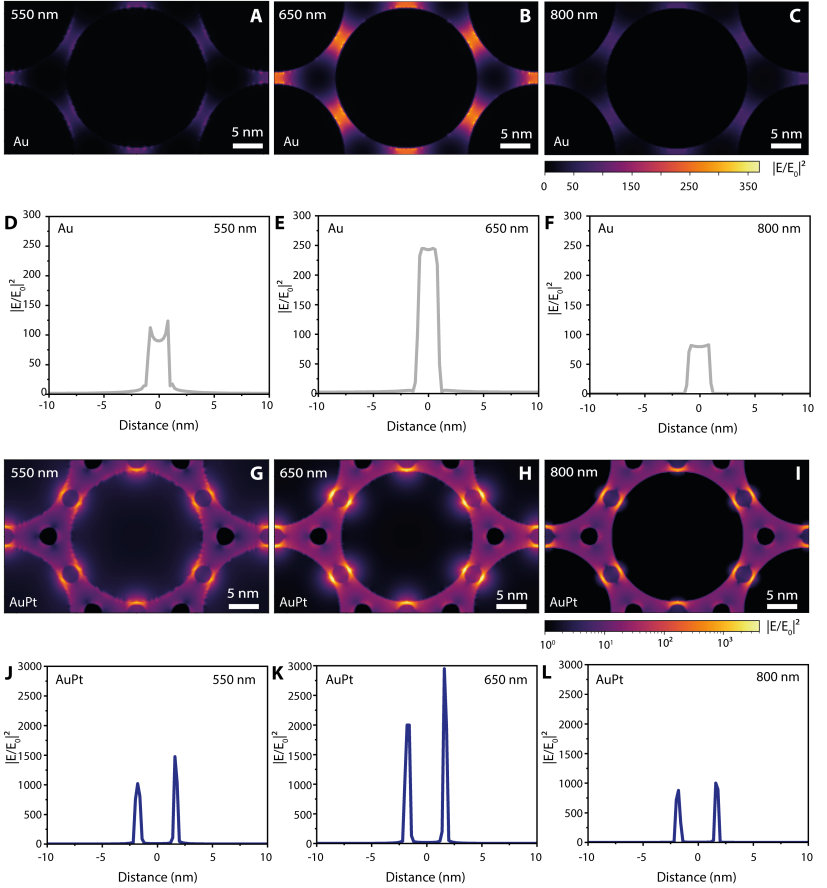


Figure 6.8: Characterization of the E-field enhancement $|E/E_0|^2$ in AuNP (A-F) and Au-Pt superlattices (G-L) according FDTD simulations with three different wavelengths of E_0 : 550 nm, 650 nm and 800 nm. A-C and G-I show simulated maps of the E-field enhancement in the particle gaps of the AuNP and Au-Pt superlattices, respectively. D-F and J-L show line scans of the E-field enhancement across the AuNP-AuNP particle gaps. Because the PtNP is not placed in the center of the AuNP-gap, the intensity profiles appear asymmetric [162].

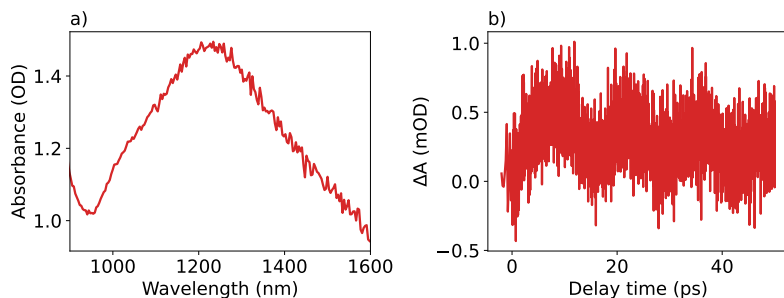


Figure 6.9: a) Steady state NIR absorbance spectrum of a AuNP superlattice. b) NIR probe TA measurement of a AuNP superlattice. The excitation wavelength was 450 nm.

6.4.3 Hot electron dynamics

Since the first study of the hot electron dynamics in AuNP superlattices has been published, the TA setup underwent an upgrade, which included a NIR continuum source and spectrometer. This allowed to test if the hot electron dynamics affect the plasmon-polariton of AuNP superlattices in the same way as the single-particle LSPR. Fig. 6.9a) shows a steady-state absorbance spectrum displaying a broad resonance feature centered around 1250 nm as one could expect from a multilayer AuNP superlattice (cf. Fig. 6.3). A TA measurement, however, did not yield any bleach signal in the NIR. Only a weak oscillation of the signal was observed (cf. Fig. 6.9b), which can be interpreted as the breathing oscillation of the strongly red-shifted single particle LSPR. Hence, it may be concluded that the electron temperature of hot electrons does not affect the absorption due to plasmon-polariton modes in AuNP superlattices in the same way as the single particle LSPR. Because this is only a single measurement, however, a comprehensive study on this topic is still needed to confirm this interpretation.

In order to further confirm that the local field enhancement within the Au-Pt superlattice leads to the increased catalytic performance of the hybrid structure without any contribution by hot electron transfer, the hot electron dynamics were studied using TA spectroscopy. The excitation wavelengths were chosen in accordance with some of the values employed in the wavelength-dependent photocatalysis experiment presented above: 400 nm was chosen to test interband excitations, and 500 nm and 650 nm were chosen to test different scalings of the absorption and field enhancement. The hybrid superlattice exhibits more absorbance at 500 nm than at 650 nm, but the E-field enhancement is much stronger at 650 nm. Like in the catalytic experiments, the differential absorption behavior of a hybrid Au-Pt superlattice was compared to an Au superlattice and to a PtNP dispersion with the same particle sizes and gaps.

Figure 6.10a-c show the TA spectra at maximum contrast for the three samples. The spectra show the same basic features, indicating that the TA signal is dominated by the optical activity of the AuNP. Comparing static absorbance spectra of the superlattices with the absorption behavior of PtNP this is hardly surprising, because AuNP are much more optically active in the visible spectrum as shown in Fig. 6.5. Additionally, within a given volume of the hybrid lattice there is much more Au mass than Pt contributing to the optical properties of the sample.

While keeping the excitation power constant ($150 \mu\text{J}/\text{cm}^2$), the bleach kinetics depending on the excitation wavelength are compared in Fig. 6.10d-f. Only the kinetics recorded at a pump wavelength of 500 nm differ slightly between the two superlattices with the hybrid lattice displaying a longer e-ph coupling time (5.0 ps vs. 4.1 ps), whereas at 400 nm and 650 nm excitation wavelengths, the bleach kinetics of the lattices coincide.

To evaluate the influence of the PtNP on the TA signal of the hybrid lattice, measurements were taken of a PtNP dispersion as well. The results are compared to the hybrid lattice in Fig. 6.11. The TA spectra of PtNP show photoinduced absorption (positive ΔA signal) at 300 nm (cf. Fig. 6.5). A pump wavelength of 300 nm instead of 400 nm was employed, because the absorbance of PtNP increases towards shorter wavelengths (cf. Fig. 6.5) and thus a stronger

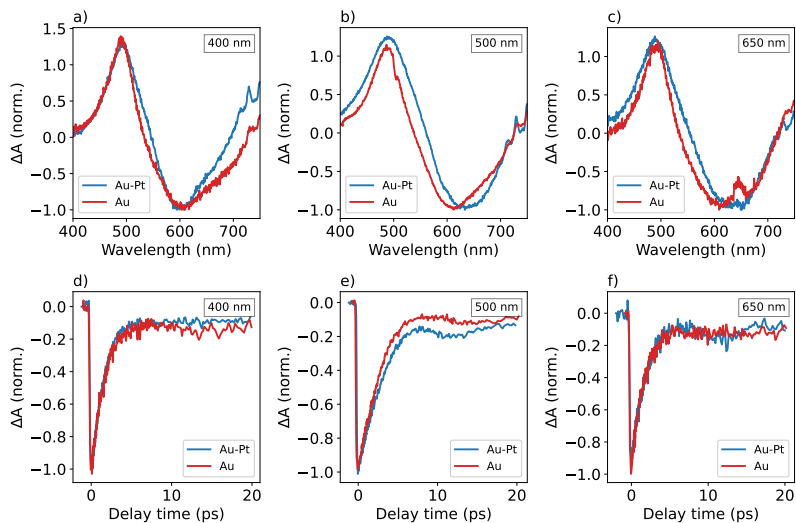


Figure 6.10: TA results of the AuNP and Au-Pt superlattice. **a)-c)** TA spectra at delay time of maximum bleach contrast for pump wavelengths of **a)** 400 nm, **b)** 500 nm and **c)** 650 nm. The spectra were normalized to the bleach minimum. **d)-f)** Normalized TA bleach kinetics for pump wavelengths of **d)** 400 nm, **e)** 500 nm and **f)** 650 nm [162].

TA signal was expected. The dynamics of the photoinduced absorption displayed in Fig. 6.11c show a quick exponential decay of the signal within 2 ps. At the wavelength of the highest E-field enhancement within the Au-Pt superlattice (650 nm) the PtNP do not show any TA signal (cf. Fig. 6.11b and d), as expected from their vanishing absorbance. Like the PtNP dispersion, the hybrid superlattice displays photoinduced absorption at 400 nm probe wavelength as well, which might indicate a contribution of the PtNP to the overall measured kinetics at those wavelengths. However, it is doubtful that the signal originates from PtNP, because of the differences in decay time, the generally higher width of the positive TA signal produced by the hybrid lattice, and the higher Au mass compared to Pt within the sample. Hence, it is much more likely, that the signatures of the hybrid lattice at short probe wavelengths are dominated by the AuNP as well. It can be concluded that the measured TA signals of the hybrid lattice originate only from the hot electron dynamics in the AuNP.

From previous studies on the hot electron dynamics in hybrid systems it can be established that any hot charge transfer would result in an acceleration of the bleach dynamics [92, 108, 154, 155]. This signature is not observable in the data shown here. In fact, the only observable difference in bleach kinetics between the pure and hybrid lattice shows the opposite trend. Thus, there is no evidence for any charge transfer in the hybrid system. In contrast to previous studies on hot electron dynamics in hybrid materials, which have shown evidence of hot electron transfer, the AuNP and PtNP are disconnected, separated materials here. Hence, for any charge transfer to occur, these would need to tunnel from the AuNP to PtNP. The likelihood of tunneling decreases with distance between the two species. With the average PtNP diameter (2.7 nm) and AuNP-to-AuNP gaps (3.5 nm) one can estimate an average distance from AuNP to PtNP of 0.4 nm, which is a distance at which tunneling could theoretically occur, but with very low probability [163, p. 28]. However, the TA results presented here indicate that for the type of material combination and excitation conditions, this process is too unlikely to compete with the hot electron relaxation within the AuNP. One should keep in mind, however, that the relative amount of Pt is very low relative to Au within the hybrid lattice. Hence, even if hot electron transfer may be unlikely because of the physical

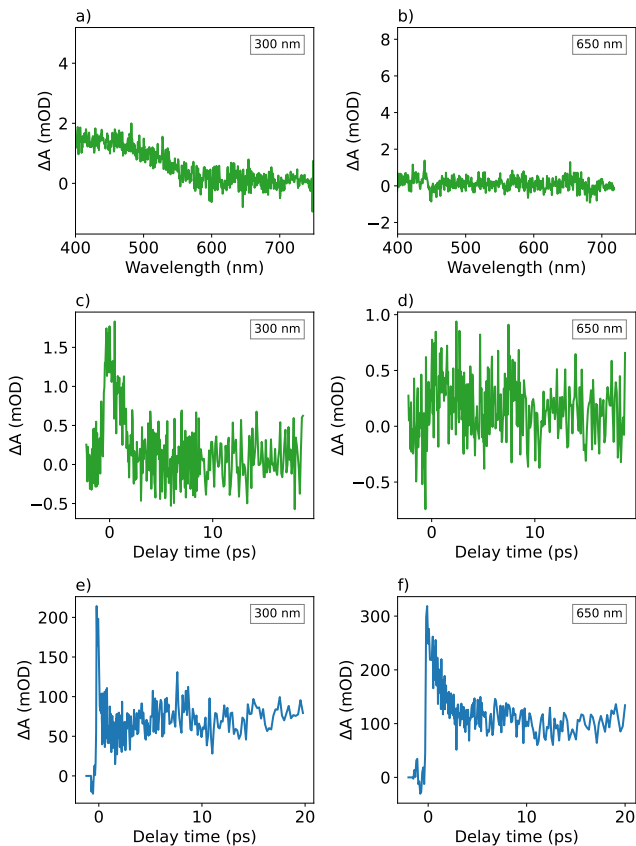


Figure 6.11: Influence of PtNP on the TA signal. **a)-b)** TA spectra of PtNP dispersion at the delay time of maximum contrast. **c)-d)** PtNP TA kinetics extracted at a *probe* wavelength of 400 nm. **e)-f)** For comparison: TA kinetics at the same probe wavelength as in c) and d) of the Au-Pt hybrid lattice. The text boxes indicate the pump wavelength [162].

separation between AuNP and PtNP and the TA results show no signatures of the effect, charge transfer can not be completely ruled out.

All in all, this interpretation of the TA data is consistent the photocatalytic mechanism proposed in the previous section. The AuNP superlattice serves as an antenna and concentrates the electromagnetic energy into the particle gaps, which increases the catalytic activity of the PtNP. This results in a superior H₂ production compared to the individual species. The results are the first study of the hot electron dynamics in a hybrid AuNP-PtNP superlattice. The parameter space scanned here was limited to provide information on the study of its photocatalytic properties and can be further expanded in the future to obtain a more complete picture of the ultrafast dynamics in hybrid lattices. Furthermore, an advantage of the hybrid superlattice system is the opportunity for customization. For example, other catalytic materials such as palladium could be incorporated in the future instead of Pt. Another interesting material to incorporate would be TiO₂, which was a popular material in previous studies of hybrid plasmonic systems [108, 164] and would therefore allow to put the TA results into a broader context.

Chapter 7

Summary and outlook

Plasmonic nanoparticles have become building blocks for exciting new materials and applications utilizing the plasmonic near-field. The dynamic properties of hot electrons remain mostly in the realm of fundamental research in solid-state physics, but are gradually explored for applications in light-energy conversion as well.

The goal of the work presented in this thesis was to gain a deeper understanding of the hot-electron dynamics in plasmonic Au nanostructures. The established picture of hot electron dynamics included a four-step process. Excitation of non-thermal hot electrons by Landau damping or direct optical excitation, energy redistribution among the electrons via electron-electron scattering, energy transfer from electrons to phonons via electron-phonon coupling and heat dissipation to the surroundings. Electron-phonon coupling in particular is modeled as a heat transfer from the electron- to phonon distribution using the two-temperature model, which includes a characteristic coupling factor.

Three studies have been presented to test this established picture. First, the validity of the widely employed two-temperature model was systematically investigated for environmental temperatures between 100 K and 350 K. While most studies of e-ph coupling in AuNP are conducted at room temperature, only few results on the hot electron dynamics at low temperatures were published yet - most with a different focus than the ambient temperature dependence of the two-temperature model. Since the two-temperature model includes the electron- and lattice heat capacities, cooling down the nanoparticle to temperatures below Au's Debye temperature of 170 K might necessitate to include a temperature-dependent lattice heat capacity according to Debye's law or treating the e-ph coupling constant as a function of temperature. However, both the simulations of the two-temperature model and the temperature dependent transient absorption results indicate a negligible impact of the decreasing heat capacity and the results are well reproduced employing a coupling constant independent of temperature. This confirms the robustness of the two-temperature model at low temperatures and thereby expanded the valid parameter space of the model.

The second study dealt with the excitation mechanism of the nanoparticle breathing oscillations that result from ultrashort optical excitation. For the first time single-particle imaging was utilized to study the transient of the particle diameter of AuNP in this context, which further establishes this technique for studying the dynamic structural behavior of nanoparticles. The results reproduced the phase disparity of the breathing oscillation observable in transient-absorption measurements by displaying a faster onset than expected from an ultrafast heat transfer according to the two-temperature model. This confirmed the need to include an additional source term to the excitation of the oscillation. While this term was previously conceptualized as "hot-electron pressure" our new theoretical framework may serve as a detailed microscopic description of the excitation mechanism. In context of the established series of energy transformation within plasmonic AuNP, the excitation of phonon modes based on the electron-density gradient, that emerged from the new theory, has to be included for a full description of e-ph coupling.

In the last study, mechanistic insight into the photocatalytic properties of newly developed hybrid nanoparticle superlattices was obtained. The unique optical properties of this new type of metamaterial and robust preparation techniques have been recently established. At the moment, the platform is further developed towards incorporating additional materials with new functionality. Among that, including catalytic nanoparticles such as PtNP might provide a new platform for photocatalysis. Our collaborators have rationalized the photocatalytic property of the hybrid structure by an antenna-reactor geometry and proposed that the catalytic enhancement was the result of plasmonic hot-spots in the AuNP gaps of the superlattice, which concentrate electromagnetic energy into the PtNP and thereby amplify their catalytic enhancement. By determining the hot-electron dynamics of AuNP and AuNP-PtNP superlattices using TA spectroscopy, no evidence for a competing mechanism aided by hot-electron transfer was found. Hence, the field enhancement mechanism proposed by our collaborators could be further confirmed. Hybrid superlattices comprising of plasmonic AuNP and catalytic nanoparticles thus prove to be a promising, customizable platform for photocatalysis.

To summarize, by utilizing ultrafast optical and x-ray techniques to study plasmonic AuNP-based systems, new knowledge on their hot-electron dynamics could be obtained: The widely applied two-temperature model seems to be valid also at low temperatures without introducing a temperature-dependent coupling factor; the excitation of breathing modes in AuNP can be studied using single-particle imaging and the excitation mechanism could be explained by a new source term based on an electron-density gradient; and hot-electron transfer does not seem to occur in AuNP-PtNP hybrid superlattices, which further indicates a field-enhancement based photocatalytic mechanism. While the two-temperature model remains a useful, easy-to-understand and surprisingly robust way to understand e-ph coupling, it does find its limit in explaining the energy transfer from electrons to radial breathing modes. An even deeper understanding of the breathing mode excitation can be acquired by conducting excitation wavelength dependent single-particle imaging, because the new theory implies differences in the relative importance between the source terms. Furthermore, the experimental procedure and theoretical framework can be expanded towards anisotropic particles such as gold nanorods,

which display more complicated breathing oscillations. The possibility to resolve their structural changes upon optical excitation highlights the potential of single-particle imaging. Besides the fundamental hot electron dynamics in AuNP, their employment in applications such as photocatalysis is an exciting prospect as well. Marrying the plasmonic properties of AuNP with catalytic properties of other nanostructures has shown great potential in this regard and more types of interactions like plexitons [165] or plasmons-dye [166, 167] interactions are interesting to explore. The prospect of directly utilizing hot electrons generated in AuNP for light-energy conversion remains as a promising endeavor for future research.

Bibliography

- [1] Stefan Alexander Maier. *Plasmonics: Fundamentals and Applications*. Springer, New York, 2007 edition, May 2007.
- [2] Harry A. Atwater. The Promise of PLASMONICS. *Scientific American*, 2007.
- [3] Matthew Pelton, Javier Aizpurua, and Garnett Bryant. Metal-nanoparticle plasmonics. *Laser & Photonics Reviews*, 2(3):136–159, June 2008.
- [4] Vincenzo Amendola, Roberto Pilot, Marco Frasconi, Onofrio M. Maragò, and Maria Antonia Iatì. Surface plasmon resonance in gold nanoparticles: A review. *Journal of Physics: Condensed Matter*, 29(20):203002, April 2017.
- [5] Mathias Brust, Meryll Walker, Donald Bethell, David J. Schiffrin, and Robin Whyman. Synthesis of thiol-derivatised gold nanoparticles in a two-phase Liquid–Liquid system. *Journal of the Chemical Society, Chemical Communications*, 7:801–802, January 1994.
- [6] F. Schulz, W. Friedrich, K. Hoppe, T. Vossmeier, H. Weller, and H. Lange. Effective PEGylation of gold nanorods. *Nanoscale*, 8(13):7296–7308, March 2016.

-
- [7] Gustav Mie. Beiträge zur Optik trüber Medien, speziell kolloidaler Metallösungen. *Annalen der Physik*, 330(3):377–445, 1908.
- [8] John Turkevich, Peter Cooper Stevenson, and James Hillier. A study of the nucleation and growth processes in the synthesis of colloidal gold. *Discussions of the Faraday Society*, 11(0):55–75, January 1951.
- [9] M. A. Garcia. Surface plasmons in metallic nanoparticles: Fundamentals and applications. *Journal of Physics D: Applied Physics*, 44(28):283001, June 2011.
- [10] Mehdi Keshavarz Hedayati, Franz Faupel, and Mady Elbahri. Review of Plasmonic Nanocomposite Metamaterial Absorber. *Materials*, 7(2):1221–1248, February 2014.
- [11] Niclas S. Mueller, Yu Okamura, Bruno G. M. Vieira, Sabrina Jürgensen, Holger Lange, Eduardo B. Barros, Florian Schulz, and Stephanie Reich. Deep strong light–matter coupling in plasmonic nanoparticle crystals. *Nature*, 583(7818):780–784, July 2020.
- [12] Florian Schulz, Ondřej Pavelka, Felix Lehmkuhler, Fabian Westermeyer, Yu Okamura, Niclas S. Mueller, Stephanie Reich, and Holger Lange. Structural order in plasmonic superlattices. *Nature Communications*, 11(1):3821, July 2020.
- [13] Gregory V. Hartland. Optical Studies of Dynamics in Noble Metal Nanostructures. *Chemical Reviews*, 111(6):3858–3887, June 2011.
- [14] Svetlana V. Boriskina, Thomas Alan Cooper, Lingping Zeng, George Ni, Jonathan K. Tong, Yoichiro Tsurimaki, Yi Huang, Laureen Meroueh, Gerald Mahan, and Gang Chen. Losses in plasmonics: From mitigating energy dissipation to embracing loss-enabled functionalities. *Advances in Optics and Photonics*, 9(4):775–827, December 2017.
- [15] C. Voisin, D. Christofilos, P. A. Loukakos, N. Del Fatti, F. Vallée, J. Lermé, M. Gaudry, E. Cottancin, M. Pellarin, and M. Broyer. Ultrafast electron-electron scattering and energy exchanges in noble-metal nanoparticles. *Physical Review B*, 69(19):195416, May 2004.

-
- [16] Patrick O’Keeffe, Daniele Catone, Lorenzo Di Mario, Francesco Toschi, Michele Magnozzi, Francesco Bisio, Alessandro Alabastri, Remo Proietti Zaccaria, Andrea Toma, Giuseppe Della Valle, and Alessandra Paladini. Disentangling the Temporal Dynamics of Non-thermal Electrons in Photoexcited Gold Nanostructures. *Laser & Photonics Reviews*, 15(6):2100017, 2021.
- [17] Rogier H. M. Groeneveld, Rudolf Sprik, and Ad Lagendijk. Femtosecond spectroscopy of electron-electron and electron-phonon energy relaxation in Ag and Au. *Physical Review B*, 51(17):11433–11445, May 1995.
- [18] S. Link, C. Burda, Z. L. Wang, and M. A. El-Sayed. Electron dynamics in gold and gold–silver alloy nanoparticles: The influence of a nonequilibrium electron distribution and the size dependence of the electron–phonon relaxation. *The Journal of Chemical Physics*, 111(3):1255–1264, July 1999.
- [19] Christophe Voisin, Natalia Del Fatti, Dimitris Christofilos, and Fabrice Vallée. Ultrafast Electron Dynamics and Optical Nonlinearities in Metal Nanoparticles. *The Journal of Physical Chemistry B*, 105(12):2264–2280, March 2001.
- [20] A. Arbouet, C. Voisin, D. Christofilos, P. Langot, N. Del Fatti, F. Vallée, J. Lermé, G. Celep, E. Cottancin, M. Gaudry, M. Pellarin, M. Broyer, M. Maillard, M. P. Pileni, and M. Treguer. Electron-Phonon Scattering in Metal Clusters. *Physical Review Letters*, 90(17):177401, April 2003.
- [21] Kenneth O. Aruda, Mario Tagliazucchi, Christina M. Sweeney, Daniel C. Hannah, George C. Schatz, and Emily A. Weiss. Identification of parameters through which surface chemistry determines the lifetimes of hot electrons in small Au nanoparticles. *Proceedings of the National Academy of Sciences*, 110(11):4212–4217, March 2013.
- [22] Ana M. Brown, Ravishankar Sundararaman, Prineha Narang, William A. Goddard, and Harry A. Atwater. Ab initio phonon

- coupling and optical response of hot electrons in plasmonic metals. *Physical Review B*, 94(7):075120, August 2016.
- [23] B. Y. Mueller and B. Rethfeld. Relaxation dynamics in laser-excited metals under nonequilibrium conditions. *Physical Review B*, 87(3):035139, January 2013.
- [24] Yannic U. Staechelin, Dominik Hoeing, Florian Schulz, and Holger Lange. Size-Dependent Electron–Phonon Coupling in Monocrystalline Gold Nanoparticles. *ACS Photonics*, 8(3):752–757, March 2021.
- [25] Guillaume Baffou, Frank Cichos, and Romain Quidant. Applications and challenges of thermoplasmonics. *Nature Materials*, 19(9):946–958, September 2020.
- [26] Florian Dufey and Sighart F. Fischer. Short Time Vibrational Dynamics of Excited Metal Nanoparticles. *The Journal of Physical Chemistry C*, 111(10):3868–3872, March 2007.
- [27] Yiqun Zheng, Xiaolan Zhong, Zhiyuan Li, and Younan Xia. Successive, Seed-Mediated Growth for the Synthesis of Single-Crystal Gold Nanospheres with Uniform Diameters Controlled in the Range of 5–150 nm. *Particle & Particle Systems Characterization*, 31(2):266–273, 2014.
- [28] Leonardo Scarabelli, Ana Sánchez-Iglesias, Jorge Pérez-Juste, and Luis M. Liz-Marzán. A “Tips and Tricks” Practical Guide to the Synthesis of Gold Nanorods. *The Journal of Physical Chemistry Letters*, 6(21):4270–4279, November 2015.
- [29] Donna Strickland and Gerard Mourou. Compression of amplified chirped optical pulses. *Optics Communications*, 55(6):447–449, October 1985.
- [30] The Nobel Prize in Physics 2018. <https://www.nobelprize.org/prizes/physics/2018/press-release/>. accessed: 2023-07-28.

-
- [31] Claude Rullière, editor. *Femtosecond Laser Pulses: Principles and Experiments*. Advanced Texts in Physics. Springer, New York, NY, 2005.
- [32] Gregory V. Hartland. Measurements of the material properties of metal nanoparticles by time-resolved spectroscopy. *Physical Chemistry Chemical Physics*, 6(23):5263–5274, November 2004.
- [33] Tais Gorkhover, Sebastian Schorb, Ryan Coffee, Marcus Adolph, Lutz Foucar, Daniela Rupp, Andrew Aquila, John D. Bozek, Sascha W. Epp, Benjamin Erk, Lars Gumprecht, Lotte Holmegaard, Andreas Hartmann, Robert Hartmann, Günter Hauser, Peter Holl, Andre Hömke, Per Johnsson, Nils Kimmel, Kai-Uwe Kühnel, Marc Messerschmidt, Christian Reich, Arnaud Rouzée, Benedikt Rudek, Carlo Schmidt, Joachim Schulz, Heike Soltau, Stephan Stern, Georg Weidenspointner, Bill White, Jochen Küpper, Lothar Strüder, Ilme Schlichting, Joachim Ullrich, Daniel Rolles, Artem Rudenko, Thomas Möller, and Christoph Bostedt. Femtosecond and nanometre visualization of structural dynamics in superheated nanoparticles. *Nature Photonics*, 10(2):93–97, February 2016.
- [34] Kartik Ayyer, P. Lourdu Xavier, Johan Bielecki, Zhou Shen, Benedikt J. Daurer, Amit K. Samanta, Salah Awel, Richard Bean, Anton Barty, Martin Bergemann, Tomas Ekeberg, Armando D. Estillore, Hans Fangohr, Klaus Giewekemeyer, Mark S. Hunter, Mikhail Karneviskiy, Richard A. Kirian, Henry Kirkwood, Yoonhee Kim, Jayanath Koliyadu, Holger Lange, Romain Letrun, Jannik Lübke, Thomas Michelat, Andrew J. Morgan, Nils Roth, Tokushi Sato, Marcin Sikorski, Florian Schulz, John C. H. Spence, Patrik Vagovic, Tamme Wollweber, Lena Worbs, Oleksandr Yefanov, Yulong Zhuang, Filipe R. N. C. Maia, Daniel A. Horke, Jochen Küpper, N. Duane Loh, Adrian P. Mancuso, and Henry N. Chapman. 3D diffractive imaging of nanoparticle ensembles using an x-ray laser. *Optica*, 8(1):15–23, January 2021.
- [35] Cheng-ping Huang, Xiao-gang Yin, Qian-jin Wang, Huang Huang, and Yong-yuan Zhu. Long-Wavelength Optical Properties of a Plasmonic Crystal. *Physical Review Letters*, 104(1):016402, January 2010.

- [36] Dayne F. Swearer, Hangqi Zhao, Linan Zhou, Chao Zhang, Hossein Robatjazi, John Mark P. Martirez, Caroline M. Krauter, Sadegh Yazdi, Michael J. McClain, Emilie Ringe, Emily A. Carter, Peter Nordlander, and Naomi J. Halas. Heterometallic antenna-reactor complexes for photocatalysis. *Proceedings of the National Academy of Sciences*, 113(32):8916–8920, August 2016.
- [37] Umar Aslam, Vishal Govind Rao, Steven Chavez, and Suljo Linic. Catalytic conversion of solar to chemical energy on plasmonic metal nanostructures. *Nature Catalysis*, 1(9):656–665, September 2018.
- [38] Katherine Sytwu, Michal Vadai, and Jennifer A. Dionne. Bimetallic nanostructures: Combining plasmonic and catalytic metals for photocatalysis. *Advances in Physics: X*, 4(1):1619480, January 2019.
- [39] César Clavero. Plasmon-induced hot-electron generation at nanoparticle/metal-oxide interfaces for photovoltaic and photocatalytic devices. *Nature Photonics*, 8(2):95–103, February 2014.
- [40] Judith Langer, Dorleta Jimenez de Aberasturi, Javier Aizpurua, Ramon A. Alvarez-Puebla, Baptiste Auguie, Jeremy J. Baumberg, Guillermo C. Bazan, Steven E. J. Bell, Anja Boisen, Alexandre G. Brolo, Jaebum Choo, Dana Cialla-May, Volker Deckert, Laura Fabris, Karen Faulds, F. Javier Garcia de Abajo, Royston Goodacre, Duncan Graham, Amanda J. Haes, Christy L. Haynes, Christian Huck, Tamitake Itoh, Mikael Ka, Janina Kneipp, Nicholas A. Kotov, Hua Kuang, Eric C. Le Ru, Hiang Kwee Lee, Jian-Feng Li, Xing Yi Ling, Stefan A. Maier, Thomas Mayerhofer, Martin Moskovits, Kei Murakoshi, Jwa-Min Nam, Shuming Nie, Yukihiro Ozaki, Isabel Pastoriza-Santos, Jorge Perez-Juste, Juergen Popp, Annemarie Pucci, Stephanie Reich, Bin Ren, George C. Schatz, Timur Shegai, Sebastian Schlucker, Li-Lin Tay, K. George Thomas, Zhong-Qun Tian, Richard P. Van Duyne, Tuan Vo-Dinh, Yue Wang, Katherine A. Willets, Clauanlai Xu, Hongxin Xu, Yikai Xu, Yuko S. Yamamoto, Bing Zhao, and Luis M. Liz-Marzan. Present and Future of Surface-Enhanced Raman Scattering. *Acs Nano*, 14(1):28–117, January 2020.

-
- [41] Niclas S. Mueller, Emanuel Pfitzner, Yu Okamura, Georgy Gordeev, Patryk Kusch, Holger Lange, Joachim Heberle, Florian Schulz, and Stephanie Reich. Surface-Enhanced Raman Scattering and Surface-Enhanced Infrared Absorption by Plasmon Polaritons in Three-Dimensional Nanoparticle Supercrystals. *ACS Nano*, 15(3):5523–5533, March 2021.
- [42] Jianfeng Guo, Kamil Rahme, Yan He, Lin-Lin Li, Justin D. Holmes, and Caitriona M. O’Driscoll. Gold nanoparticles enlighten the future of cancer theranostics. *International Journal of Nanomedicine*, 12:6131–6152, 2017.
- [43] S I Anisimov, B L Kapeliovich, and T L Perelman. Electron emission from metal surfaces exposed to ultrashort laser pulses. *Journal of Experimental and Theoretical Physics*, 39(2):375–377, 1974.
- [44] José H. Hodak, Ignacio Martini, and Gregory V. Hartland. Observation of acoustic quantum beats in nanometer sized Au particles. *The Journal of Chemical Physics*, 108(22):9210–9213, June 1998.
- [45] M. Perner, S. Gresillon, J. März, G. von Plessen, J. Feldmann, J. Porsendorfer, K.-J. Berg, and G. Berg. Observation of Hot-Electron Pressure in the Vibration Dynamics of Metal Nanoparticles. *Physical Review Letters*, 85(4):792–795, July 2000.
- [46] Gregory V. Hartland. Coherent Excitation of Vibrational Modes in Metallic Nanoparticles. *Annual Review of Physical Chemistry*, 57(1):403–430, 2006.
- [47] Robert Salzwedel, Andreas Knorr, Dominik Hoeing, Holger Lange, and Malte Selig. Theory of radial oscillations in metal nanoparticles driven by optically induced electron density gradients. *The Journal of Chemical Physics*, 158(6):064107, February 2023.
- [48] C. Voisin, N. Del Fatti, D. Christofilos, and F. Vallée. Time-resolved investigation of the vibrational dynamics of metal nanoparticles. *Applied Surface Science*, 164(1):131–139, September 2000.

- [49] Aurélien Crut, Paolo Maioli, Natalia Del Fatti, and Fabrice Vallée. Acoustic vibrations of metal nano-objects: Time-domain investigations. *Physics Reports*, 549:1–43, 2015.
- [50] Dominik Hoeing, Florian Schulz, Niclas S. Mueller, Stephanie Reich, and Holger Lange. Dark plasmon modes for efficient hot electron generation in multilayers of gold nanoparticles. *The Journal of Chemical Physics*, 152(6):064710, February 2020.
- [51] Anthony Mark Fox. *Optical Properties of Solids*. Oxford University Press, 2001.
- [52] A. Sommerfeld. Zur Elektronentheorie der Metalle auf Grund der Fermischen Statistik. *Zeitschrift für Physik*, 47(1):1–32, January 1928.
- [53] P. B. Johnson and R. W. Christy. Optical Constants of the Noble Metals. *Physical Review B*, 6(12):4370–4379, December 1972.
- [54] Benjamin J. Sumlin, William R. Heinson, and Rajan K. Chakrabarty. Retrieving the aerosol complex refractive index using PyMieScatt: A Mie computational package with visualization capabilities. *Journal of Quantitative Spectroscopy and Radiative Transfer*, 205:127–134, January 2018.
- [55] Benjamin J. Sumlin. Online user’s guide for the Python Mie Scattering package (PyMieScatt). <https://pymiescatt.readthedocs.io/en/latest/#>, July 2023. accessed: 2023-07-28.
- [56] Kathryn M. Mayer and Jason H. Hafner. Localized Surface Plasmon Resonance Sensors. *Chemical Reviews*, 111(6):3828–3857, June 2011.
- [57] Carolina Novo, Daniel Gomez, Jorge Perez-Juste, Zhenyuan Zhang, Hristina Petrova, Maximilian Reismann, Paul Mulvaney, and Gregory V. Hartland. Contributions from radiation damping and surface scattering to the linewidth of the longitudinal plasmon band of gold nanorods: A single particle study. *Physical Chemistry Chemical Physics*, 8(30):3540–3546, July 2006.

-
- [58] Benjamin Foerster, Anneli Joplin, Katharina Kaefer, Sirin Celiksoy, Stephan Link, and Carsten Sönnichsen. Chemical Interface Damping Depends on Electrons Reaching the Surface. *ACS Nano*, 11(3):2886–2893, March 2017.
- [59] Alessandro Alabastri, Salvatore Tuccio, Andrea Giugni, Andrea Toma, Carlo Liberale, Gobind Das, Francesco De Angelis, Enzo Di Fabrizio, and Remo Proietti Zaccaria. Molding of Plasmonic Resonances in Metallic Nanostructures: Dependence of the Non-Linear Electric Permittivity on System Size and Temperature. *Materials*, 6(11):4879–4910, November 2013.
- [60] O. A. Yeshchenko, I. S. Bondarchuk, V. S. Gurin, I. M. Dmitruk, and A. V. Kotko. Temperature dependence of the surface plasmon resonance in gold nanoparticles. *Surface Science*, 608:275–281, February 2013.
- [61] Ana M. Brown, Ravishankar Sundararaman, Prineha Narang, William A. Goddard, and Harry A. Atwater. Nonradiative Plasmon Decay and Hot Carrier Dynamics: Effects of Phonons, Surfaces, and Geometry. *ACS Nano*, 10(1):957–966, January 2016.
- [62] C. Sönnichsen, T. Franzl, T. Wilk, G. von Plessen, and J. Feldmann. Plasmon resonances in large noble-metal clusters. *New Journal of Physics*, 4(1):93, November 2002.
- [63] Seung Beom Park, Kyungseung Kim, Wosik Cho, Sung In Hwang, Igor Ivanov, Chang Hee Nam, and Kyung Taec Kim. Direct sampling of a light wave in air. *Optica*, 5(4):402–408, April 2018.
- [64] C.-K. Sun, F. Vallée, L. H. Acioli, E. P. Ippen, and J. G. Fujimoto. Femtosecond-tunable measurement of electron thermalization in gold. *Physical Review B*, 50(20):15337–15348, November 1994.
- [65] C. Voisin, D. Christofilos, N. Del Fatti, F. Vallée, B. Prével, E. Cotancin, J. Lermé, M. Pellarin, and M. Broyer. Size-Dependent Electron-Electron Interactions in Metal Nanoparticles. *Physical Review Letters*, 85(10):2200–2203, September 2000.

- [66] H. E. Elsayed-Ali, T. Juhasz, G. O. Smith, and W. E. Bron. Femtosecond thermorefectivity and thermotransmissivity of polycrystalline and single-crystalline gold films. *Physical Review B*, 43(5):4488–4491, February 1991.
- [67] Zhibin Lin, Leonid V. Zhigilei, and Vittorio Celli. Electron-phonon coupling and electron heat capacity of metals under conditions of strong electron-phonon nonequilibrium. *Physical Review B*, 77(7):075133, February 2008.
- [68] Emanuele Minutella, Florian Schulz, and Holger Lange. Excitation-Dependence of Plasmon-Induced Hot Electrons in Gold Nanoparticles. *The Journal of Physical Chemistry Letters*, 8(19):4925–4929, October 2017.
- [69] Orla M. Wilson, Xiaoyuan Hu, David G. Cahill, and Paul V. Braun. Colloidal metal particles as probes of nanoscale thermal transport in fluids. *Physical Review B*, 66(22):224301, December 2002.
- [70] Zhenbin Ge, David G. Cahill, and Paul V. Braun. AuPd Metal Nanoparticles as Probes of Nanoscale Thermal Transport in Aqueous Solution. *The Journal of Physical Chemistry B*, 108(49):18870–18875, December 2004.
- [71] A. Plech, V. Kotaidis, S. Grésillon, C. Dahmen, and G. Von Plessen. Laser-induced heating and melting of gold nanoparticles studied by time-resolved x-ray scattering. *Physical Review B*, 70(19):195423, November 2004.
- [72] Harsha Reddy, Kun Wang, Zhaxylyk Kudyshev, Linxiao Zhu, Shen Yan, Andrea Vezzoli, Simon J. Higgins, Vikram Gavini, Alexandra Boltasseva, Pramod Reddy, Vladimir M. Shalaev, and Edgar Meyhofer. Determining plasmonic hot-carrier energy distributions via single-molecule transport measurements. *Science*, 369(6502):423–426, July 2020.

-
- [73] Michael Hartelt, Pavel N. Terekhin, Tobias Eul, Anna-Katharina Mahro, Benjamin Frisch, Eva Prinz, Baerbel Rethfeld, Benjamin Stadtmüller, and Martin Aeschlimann. Energy and Momentum Distribution of Surface Plasmon-Induced Hot Carriers Isolated via Spatiotemporal Separation. *ACS Nano*, 15(12):19559–19569, December 2021.
- [74] Marco Bernardi, Jamal Mustafa, Jeffrey B. Neaton, and Steven G. Louie. Theory and computation of hot carriers generated by surface plasmon polaritons in noble metals. *Nature Communications*, 6(1):7044, June 2015.
- [75] E. Carpene. Ultrafast laser irradiation of metals: Beyond the two-temperature model. *Physical Review B*, 74(2):024301, July 2006.
- [76] G. Della Valle, M. Conforti, S. Longhi, G. Cerullo, and D. Brida. Real-time optical mapping of the dynamics of nonthermal electrons in thin gold films. *Physical Review B*, 86(15):155139, October 2012.
- [77] Neil W. Ashcroft and David N. Mermin. *Festkörperphysik*. Oldenbourg Wissenschaftsverlag, München Wien, 2. auflage edition, 2005.
- [78] V. Recoules, J. Clérouin, G. Zérah, P. M. Anglade, and S. Mazevet. Effect of Intense Laser Irradiation on the Lattice Stability of Semiconductors and Metals. *Physical Review Letters*, 96(5):055503, February 2006.
- [79] Andrey V. Lugovskoy and Igor Bray. Ultrafast electron dynamics in metals under laser irradiation. *Physical Review B*, 60(5):3279–3288, August 1999.
- [80] P. J. van Hall. Ultrafast processes in Ag and Au: A Monte Carlo study. *Physical Review B*, 63(10):104301, February 2001.
- [81] Fabio Caruso and Dino Novko. Ultrafast dynamics of electrons and phonons: From the two-temperature model to the time-dependent Boltzmann equation. *Advances in Physics: X*, 7(1):2095925, December 2022.

- [82] Wenyu Huang, Wei Qian, Mostafa A. El-Sayed, Yong Ding, and Zhong Lin Wang. Effect of the Lattice Crystallinity on the Electron-Phonon Relaxation Rates in Gold Nanoparticles. *The Journal of Physical Chemistry C*, 111(29):10751–10757, July 2007.
- [83] Burak Guzelturk, James K. Utterback, Igor Coropceanu, Vladislav Kamysbayev, Eric M. Janke, Marc Zajac, Nuri Yazdani, Benjamin L. Cotts, Suji Park, Aditya Sood, Ming-Fu Lin, Alexander H. Reid, Michael E. Kozina, Xiaozhe Shen, Stephen P. Weathersby, Vanessa Wood, Alberto Salleo, Xijie Wang, Dmitri V. Talapin, Naomi S. Ginsberg, and Aaron M. Lindenberg. Nonequilibrium Thermodynamics of Colloidal Gold Nanocrystals Monitored by Ultrafast Electron Diffraction and Optical Scattering Microscopy. *ACS Nano*, 14(4):4792–4804, April 2020.
- [84] William M. Haynes. *Crc Handbook of Chemistry and Physics*. CRC Press LLC, Milton, UNITED KINGDOM, 2016.
- [85] Ana M. Brown, Ravishankar Sundararaman, Prineha Narang, Adam M. Schwartzberg, William A. Goddard, and Harry A. Atwater. Experimental and Ab Initio Ultrafast Carrier Dynamics in Plasmonic Nanoparticles. *Physical Review Letters*, 118(8):087401, February 2017.
- [86] José H. Hodak, Arnim Henglein, and Gregory V. Hartland. Electron-phonon coupling dynamics in very small (between 2 and 8 nm diameter) Au nanoparticles. *The Journal of Chemical Physics*, 112(13):5942–5947, April 2000.
- [87] J. R. M. Saavedra, Ana Asenjo-Garcia, and F. Javier García de Abajo. Hot-Electron Dynamics and Thermalization in Small Metallic Nanoparticles. *ACS Photonics*, 3(9):1637–1646, September 2016.
- [88] Yun Tang and Min Ouyang. Tailoring properties and functionalities of metal nanoparticles through crystallinity engineering. *Nature Materials*, 6(10):754–759, October 2007.

-
- [89] Ankit Jain and Alan J. H. McGaughey. Thermal transport by phonons and electrons in aluminum, silver, and gold from first principles. *Physical Review B*, 93(8):081206, February 2016.
- [90] Yuchao Zhang, Shuai He, Wenxiao Guo, Yue Hu, Jiawei Huang, Justin R. Mulcahy, and Wei David Wei. Surface-Plasmon-Driven Hot Electron Photochemistry. *Chemical Reviews*, 118(6):2927–2954, March 2018.
- [91] John A. Tomko, Evan L. Runnerstrom, Yi-Siang Wang, Weibin Chu, Joshua R. Nolen, David H. Olson, Kyle P. Kelley, Angela Cleri, Josh Nordlander, Joshua D. Caldwell, Oleg V. Prezhdo, Jon-Paul Maria, and Patrick E. Hopkins. Long-lived modulation of plasmonic absorption by ballistic thermal injection. *Nature Nanotechnology*, 16(1):47–51, January 2021.
- [92] Christian Engelbrekt, Kevin T. Crampton, Dmitry A. Fishman, Matt Law, and Vartkess Ara Apkarian. Efficient Plasmon-Mediated Energy Funneling to the Surface of Au@Pt Core-Shell Nanocrystals. *ACS Nano*, 14(4):5061–5074, April 2020.
- [93] B. D. Guenther. *Modern Optics*. Oxford University Press, 2015.
- [94] M. Lorenc, M. Ziolk, R. Naskrecki, J. Karolczak, J. Kubicki, and A. Maciejewski. Artifacts in femtosecond transient absorption spectroscopy. *Applied Physics B*, 74(1):19–27, January 2002.
- [95] Ryszard Naskrecki, Marjorie Ménard, Peter van der Meulen, Georges Vigneron, and Stanislas Pommeret. Three-photon absorption cross-section of simple molecular liquids. *Optics Communications*, 153(1):32–38, July 1998.
- [96] S. A. Kovalenko, A. L. Dobryakov, J. Ruthmann, and N. P. Ernsting. Femtosecond spectroscopy of condensed phases with chirped supercontinuum probing. *Physical Review A*, 59(3):2369–2384, March 1999.
- [97] K. Ekvall, P. van der Meulen, C. Dhollande, L.-E. Berg, S. Pommeret, R. Naskrecki, and J.-C. Mialocq. Cross phase modulation artifact in

- liquid phase transient absorption spectroscopy. *Journal of Applied Physics*, 87(5):2340–2352, March 2000.
- [98] Olivier Devos, Nicolas Mouton, Michel Sliwa, and Cyril Ruckebusch. Baseline correction methods to deal with artifacts in femtosecond transient absorption spectroscopy. *Analytica Chimica Acta*, 705(1):64–71, October 2011.
- [99] Sujit Kumar Ghosh and Tarasankar Pal. Interparticle Coupling Effect on the Surface Plasmon Resonance of Gold Nanoparticles: From Theory to Applications. *Chemical Reviews*, 107(11):4797–4862, November 2007.
- [100] Younan Xia, Xiaohu Xia, and Hsin-Chieh Peng. Shape-Controlled Synthesis of Colloidal Metal Nanocrystals: Thermodynamic versus Kinetic Products. *Journal of the American Chemical Society*, 137(25):7947–7966, July 2015.
- [101] Andre E. Nel, Lutz Mädler, Darrell Velegol, Tian Xia, Eric M. V. Hoek, Ponisseril Somasundaran, Fred Klaessig, Vince Castranova, and Mike Thompson. Understanding biophysicochemical interactions at the nano–bio interface. *Nature Materials*, 8(7):543–557, July 2009.
- [102] Florian Schulz, Gregor T. Dahl, Stephanie Besztejnan, Martin A. Schroer, Felix Lehmkuhler, Gerhard Grübel, Tobias Vossmeier, and Holger Lange. Ligand Layer Engineering To Control Stability and Interfacial Properties of Nanoparticles. *Langmuir*, 32(31):7897–7907, August 2016.
- [103] Victor K. LaMer and Robert H. Dinegar. Theory, Production and Mechanism of Formation of Monodispersed Hydrosols. *Journal of the American Chemical Society*, 72(11):4847–4854, November 1950.
- [104] Christopher B. Whitehead, Saim Özkar, and Richard G. Finke. LaMer’s 1950 Model for Particle Formation of Instantaneous Nucleation and Diffusion-Controlled Growth: A Historical Look at the Model’s Origins, Assumptions, Equations, and Underlying Sulfur Sol Formation

- Kinetics Data. *Chemistry of Materials*, 31(18):7116–7132, September 2019.
- [105] Wolfgang Haiss, Nguyen T. K. Thanh, Jenny Aveyard, and David G. Fernig. Determination of Size and Concentration of Gold Nanoparticles from UV-Vis Spectra. *Analytical Chemistry*, 79(11):4215–4221, 2007.
- [106] Brent Fultz and James Howe. *Transmission Electron Microscopy and Diffractometry of Materials*. Graduate Texts in Physics. Springer, Berlin, Heidelberg, 2013.
- [107] Yocef Hattori, Jie Meng, Kaibo Zheng, Ageo Meier de Andrade, Jolla Kullgren, Peter Broqvist, Peter Nordlander, and Jacinto Sá. Phonon-Assisted Hot Carrier Generation in Plasmonic Semiconductor Systems. *Nano Letters*, 21(2):1083–1089, January 2021.
- [108] Nandan Ghorai, Goutam De, and Hirendra N. Ghosh. Plasmon Mediated Electron Transfer and Temperature Dependent Electron-Phonon Scattering in Gold Nanoparticles Embedded in Dielectric Films. *ChemPhysChem*, 23(16):e202200181, 2022.
- [109] Ashutosh Giri, John T. Gaskins, Brian M. Foley, Ramez Cheaito, and Patrick E. Hopkins. Experimental evidence of excited electron number density and temperature effects on electron-phonon coupling in gold films. *Journal of Applied Physics*, 117(4):044305, January 2015.
- [110] Wei Wang and David G. Cahill. Limits to Thermal Transport in Nanoscale Metal Bilayers due to Weak Electron-Phonon Coupling in Au and Cu. *Physical Review Letters*, 109(17):175503, October 2012.
- [111] Xin Zhou, Linqiu Li, Hao Dong, Ashutosh Giri, Patrick E. Hopkins, and Oleg V. Prezhdo. Temperature Dependence of Electron–Phonon Interactions in Gold Films Rationalized by Time-Domain Ab Initio Analysis. *The Journal of Physical Chemistry C*, 121(32):17488–17497, August 2017.

- [112] T. H. Geballe and W. F. Giaque. The Heat Capacity and Entropy of Gold from 15 to 300K. *Journal of the American Chemical Society*, 74(9):2368–2369, May 1952.
- [113] N. Sultanova, S. Kasarova, and I. Nikolov. Dispersion Properties of Optical Polymers. *Acta Physica Polonica A*, 116(4):585–587, October 2009.
- [114] Marzia Ferrera, Giuseppe Della Valle, Maria Sygletou, Michele Magnozzi, Daniele Catone, Patrick O’Keeffe, Alessandra Paladini, Francesco Toschi, Lorenzo Mattera, Maurizio Canepa, and Francesco Bisio. Thermometric Calibration of the Ultrafast Relaxation Dynamics in Plasmonic Au Nanoparticles. *ACS Photonics*, 7(4):959–966, April 2020.
- [115] C. Voisin, D. Christofilos, N. Del Fatti, and F. Vallée. Environment effect on the acoustic vibration of metal nanoparticles. *Physica B: Condensed Matter*, 316–317:89–94, May 2002.
- [116] A. Arbouet, N. Del Fatti, and F. Vallee. Optical control of the coherent acoustic vibration of metal nanoparticles. *The Journal of Chemical Physics*, 124(14):144701, April 2006.
- [117] J. N. Clark, L. Beitra, G. Xiong, A. Higginbotham, D. M. Fritz, H. T. Lemke, D. Zhu, M. Chollet, G. J. Williams, M. Messerschmidt, B. Abbey, R. J. Harder, A. M. Korsunsky, J. S. Wark, and I. K. Robinson. Ultrafast Three-Dimensional Imaging of Lattice Dynamics in Individual Gold Nanocrystals. *Science*, 341(6141):56–59, July 2013.
- [118] Franco P. Bonafé, Bálint Aradi, Mengxue Guan, Oscar A. Douglas-Gallardo, Chao Lian, Sheng Meng, Thomas Frauenheim, and Cristián G. Sánchez. Plasmon-driven sub-picosecond breathing of metal nanoparticles. *Nanoscale*, 9(34):12391–12397, August 2017.
- [119] Ye-Jin Kim, Hayoon Jung, Sang Woo Han, and Oh-Hoon Kwon. Ultrafast Electron Microscopy Visualizes Acoustic Vibrations of Plasmonic Nanorods at the Interfaces. *Matter*, 1(2):481–495, August 2019.

-
- [120] N Del Fatti, C Voisin, F Chevy, F Vallée, and C Flytzanis. Coherent acoustic mode oscillation and damping in silver nanoparticles. *The Journal of chemical physics*, 110(23):11484–11487, 1999.
- [121] Tao Li, Andrew J. Senesi, and Byeongdu Lee. Small Angle X-ray Scattering for Nanoparticle Research. *Chemical Reviews*, 116(18):11128–11180, September 2016.
- [122] Jose H. Hodak, Arnim Henglein, and Gregory V. Hartland. Size dependent properties of Au particles: Coherent excitation and dephasing of acoustic vibrational modes. *The Journal of Chemical Physics*, 111(18):8613–8621, November 1999.
- [123] Jose H. Hodak, Arnim Henglein, and Gregory V. Hartland. Photo-physics of Nanometer Sized Metal Particles: Electron-Phonon Coupling and Coherent Excitation of Breathing Vibrational Modes. *The Journal of Physical Chemistry B*, 104(43):9954–9965, November 2000.
- [124] Gregory V Hartland. Coherent vibrational motion in metal particles: Determination of the vibrational amplitude and excitation mechanism. *The Journal of chemical physics*, 116(18):8048–8055, 2002.
- [125] Horace Lamb. On the vibrations of an elastic sphere. *Proceedings of the London Mathematical Society*, 1(1):189–212, 1881.
- [126] V. E. Gusev. On the duration of acoustic pulses excited by subpicosecond laser action on metals. *Optics Communications*, 94(1):76–78, November 1992.
- [127] Ravishankar Sundararaman, Prineha Narang, Adam S. Jermyn, William A. Goddard, and Harry A. Atwater. Theoretical predictions for hot-carrier generation from surface plasmon decay. *Nature Communications*, 5:5788, December 2014.
- [128] Ortwin Hess and Tilmann Kuhn. Spatio-temporal dynamics of semiconductor lasers: Theory, modelling and analysis. *Progress in quantum electronics*, 20(2):85–179, 1996.

- [129] Dominik Hoeing, Robert Salzwedel, Lena Worbs, Yulong Zhuang, Amit K. Samanta, Jannik Lübke, Armando D. Estillore, Karol Dlugolecki, Christopher Passow, Benjamin Erk, Nagitha Ekanayake, Daniel Ramm, Jonathan Correa, Christina C. Papadopoulou, Atia Tul Noor, Florian Schulz, Malte Selig, Andreas Knorr, Kartik Ayyer, Jochen Küpper, and Holger Lange. Time-Resolved Single-Particle X-ray Scattering Reveals Electron-Density Gradients As Coherent Plasmonic-Nanoparticle-Oscillation Source. *Nano Letters*, 23(13):5943–5950, July 2023.
- [130] W. C. Röntgen. On a New Kind of Rays. *Science*, 3(59):227–231, February 1896.
- [131] M. F. Hantke, J. Bielecki, O. Kulyk, D. Westphal, D. S. D. Larsson, M. Svenda, H. K. N. Reddy, R. A. Kirian, J. Andreasson, J. Hajdu, and F. R. N. C. Maia. Rayleigh-scattering microscopy for tracking and sizing nanoparticles in focused aerosol beams. *IUCrJ*, 5(6):673–680, November 2018.
- [132] L. Worbs, N. Roth, J. Lübke, A. D. Estillore, P. L. Xavier, A. K. Samanta, and J. Küpper. Optimizing the geometry of aerodynamic lens injectors for single-particle coherent diffractive imaging of gold nanoparticles. *Journal of Applied Crystallography*, 54(6):1730–1737, December 2021.
- [133] Peter Schmüser, Martin Dohlus, Jörg Rossbach, and Christopher Behrens. *Free-Electron Lasers in the Ultraviolet and X-Ray Regime: Physical Principles, Experimental Results, Technical Realization*, volume 258 of *Springer Tracts in Modern Physics*. Springer International Publishing, Cham, 2014.
- [134] B. Erk, J. P. Müller, C. Bomme, R. Boll, G. Brenner, H. N. Chapman, J. Correa, S. Düsterer, S. Dziarzhytski, S. Eisebitt, H. Graafsma, S. Grunewald, L. Gumprecht, R. Hartmann, G. Hauser, B. Keitel, C. von Korff Schmising, M. Kuhlmann, B. Manschwetus, L. Mercadier, E. Müller, C. Passow, E. Plönjes, D. Ramm, D. Rompotis, A. Rudenko,

- D. Rupp, M. Sauppe, F. Siewert, D. Schlosser, L. Strüder, A. Swiderski, S. Techert, K. Tiedtke, T. Tilp, R. Treusch, I. Schlichting, J. Ullrich, R. Moshhammer, T. Möller, and D. Rolles. CAMP@FLASH: An endstation for imaging, electron- and ion-spectroscopy, and pump-probe experiments at the FLASH free-electron laser. *Journal of Synchrotron Radiation*, 25(5):1529–1540, September 2018.
- [135] Lothar Strüder, Sascha Epp, Daniel Rolles, Robert Hartmann, Peter Holl, Gerhard Lutz, Heike Soltau, Rouven Eckart, Christian Reich, Klaus Heinzinger, Christian Thamm, Artem Rudenko, Faton Krasniqi, Kai-Uwe Kühnel, Christian Bauer, Claus-Dieter Schröter, Robert Moshhammer, Simone Techert, Danilo Miessner, Matteo Porro, Olaf Hälker, Norbert Meidinger, Nils Kimmel, Robert Andritschke, Florian Schopper, Georg Weidenspointner, Alexander Ziegler, Daniel Pietschner, Sven Herrmann, Ullrich Pietsch, Albert Walenta, Wolfram Leitenberger, Christoph Bostedt, Thomas Möller, Daniela Rupp, Marcus Adolph, Heinz Graafsma, Helmut Hirsemann, Klaus Gärtner, Rainer Richter, Lutz Foucar, Robert L. Shoeman, Ilme Schlichting, and Joachim Ullrich. Large-format, high-speed, X-ray pnCCDs combined with electron and ion imaging spectrometers in a multipurpose chamber for experiments at 4th generation light sources. *Nuclear Instruments and Methods in Physics Research Section A: Accelerators, Spectrometers, Detectors and Associated Equipment*, 614(3):483–496, March 2010.
- [136] M. O. Wiedorn, S. Awel, A. J. Morgan, M. Barthelmess, R. Bean, K. R. Beyerlein, L. M. G. Chavas, N. Eckerskorn, H. Fleckenstein, M. Heymann, D. A. Horke, J. Knoška, V. Mariani, D. Oberthür, N. Roth, O. Yefanov, A. Barty, S. Bajt, J. Küpper, A. V. Rode, R. A. Kirian, and H. N. Chapman. Post-sample aperture for low background diffraction experiments at X-ray free-electron lasers. *Journal of Synchrotron Radiation*, 24(6):1296–1298, November 2017.
- [137] H. Redlin, A. Al-Shemmary, A. Azima, N. Stojanovic, F. Tavella, I. Will, and S. Düsterer. The FLASH pump-probe laser system: Setup, characterization and optical beamlines. *Nuclear Instruments and Meth-*

- ods in Physics Research Section A: Accelerators, Spectrometers, Detectors and Associated Equipment*, 635(1, Supplement):S88–S93, April 2011.
- [138] Salah Awel, Richard A. Kirian, Niko Eckerskorn, Max Wiedorn, Daniel A. Horke, Andrei V. Rode, Jochen Küpper, and Henry N. Chapman. Visualizing aerosol-particle injection for diffractive-imaging experiments. *Optics Express*, 24(6):6507–6521, March 2016.
- [139] O. Krupin, M. Trigo, W. F. Schlotter, M. Beye, F. Sorgenfrei, J. J. Turner, D. A. Reis, N. Gerken, S. Lee, W. S. Lee, G. Hays, Y. Acremann, B. Abbey, R. Coffee, M. Messerschmidt, S. P. Hau-Riege, G. Lapertot, J. Lüning, P. Heimann, R. Soufli, M. Fernández-Perea, M. Rowen, M. Holmes, S. L. Molodtsov, A. Föhlisch, and W. Wurth. Temporal cross-correlation of x-ray free electron and optical lasers using soft x-ray pulse induced transient reflectivity. *Optics Express*, 20(10):11396–11406, May 2012.
- [140] O. Ekici, R. K. Harrison, N. J. Durr, D. S. Eversole, M. Lee, and A. Ben-Yakar. Thermal Analysis of Gold Nanorods Heated with Femtosecond Laser Pulses. *Journal of Physics D: Applied Physics*, 41(18):185501, 2008.
- [141] J. C. Slater. Atomic Radii in Crystals. *The Journal of Chemical Physics*, 41(10):3199–3204, 1964. atomic radius of gold: 0.135 nm.
- [142] Tian-Song Deng, John Parker, Yuval Yifat, Nolan Shepherd, and Norbert F. Scherer. Dark Plasmon Modes in Symmetric Gold Nanoparticle Dimers Illuminated by Focused Cylindrical Vector Beams. *The Journal of Physical Chemistry C*, 122(48):27662–27672, December 2018.
- [143] Niclas S. Mueller, Bruno G. M. Vieira, Dominik Hoewing, Florian Schulz, Eduardo B. Barros, Holger Lange, and Stephanie Reich. Direct optical excitation of dark plasmons for hot electron generation. *Faraday Discussions*, 214(0):159–173, May 2019.

-
- [144] Simon Lamowski, Charlie-Ray Mann, Felicitas Hellbach, Eros Mariani, Guillaume Weick, and Fabian Pauly. Plasmon polaritons in cubic lattices of spherical metallic nanoparticles. *Physical Review B*, 97(12):125409, March 2018.
- [145] Simone De Liberato. Light-Matter Decoupling in the Deep Strong Coupling Regime: The Breakdown of the Purcell Effect. *Physical Review Letters*, 112(1):016401, January 2014.
- [146] Angang Dong, Jun Chen, Patrick M. Vora, James M. Kikkawa, and Christopher B. Murray. Binary nanocrystal superlattice membranes self-assembled at the liquid–air interface. *Nature*, 466(7305):474–477, July 2010.
- [147] Florian Schulz and Holger Lange. Optimizing Interparticle Gaps in Large-Scale Gold Nanoparticle Supercrystals for Flexible Light-Matter Coupling. *Advanced Optical Materials*, 10(24):2202064, 2022.
- [148] Bhogeswararao Seemala, Andrew J. Therrien, Minhan Lou, Kun Li, Jordan P. Finzel, Ji Qi, Peter Nordlander, and Phillip Christopher. Plasmon-Mediated Catalytic O₂ Dissociation on Ag Nanostructures: Hot Electrons or Near Fields? *ACS Energy Letters*, 4(8):1803–1809, August 2019.
- [149] Marina Rodio, Matthias Graf, Florian Schulz, Niclas S. Mueller, Manfred Eich, and Holger Lange. Experimental Evidence for Nonthermal Contributions to Plasmon-Enhanced Electrochemical Oxidation Reactions. *ACS Catalysis*, 10(3):2345–2353, February 2020.
- [150] Mirko Vanzan, Gabriel Gil, Davide Castaldo, Peter Nordlander, and Stefano Corni. Energy Transfer to Molecular Adsorbates by Transient Hot Electron Spillover. *Nano Letters*, 23(7):2719–2725, April 2023.
- [151] Scott K. Cushing, Jiangtian Li, Joseph Bright, Brandon T. Yost, Peng Zheng, Alan D. Bristow, and Nianqiang Wu. Controlling Plasmon-Induced Resonance Energy Transfer and Hot Electron Injection Processes in Metal@TiO₂ Core–Shell Nanoparticles. *The Journal of Physical Chemistry C*, 119(28):16239–16244, July 2015.

- [152] Shuang Zhao, Marc Riedel, Javier Patarroyo, Neus G. Bastús, Victor Puntès, Zhao Yue, Fred Lisdat, and Wolfgang J. Parak. Tailoring of the photocatalytic activity of CeO₂ nanoparticles by the presence of plasmonic Ag nanoparticles. *Nanoscale*, 14(33):12048–12059, August 2022.
- [153] K. Wu, J. Chen, J. R. McBride, and T. Lian. Efficient hot-electron transfer by a plasmon-induced interfacial charge-transfer transition. *Science*, 349(6248):632–635, August 2015.
- [154] Mohammadreza Nazemi, Sajanlal R. Panikkanvalappil, Chih-Kai Liao, Mahmoud A. Mahmoud, and Mostafa A. El-Sayed. Role of Femtosecond Pulsed Laser-Induced Atomic Redistribution in Bimetallic Au–Pd Nanorods on Optoelectronic and Catalytic Properties. *ACS Nano*, 15(6):10241–10252, June 2021.
- [155] Xibo Zhang, Yunyan Fan, Enming You, Zexuan Li, Yongdi Dong, Luning Chen, Ye Yang, Zhaoxiong Xie, Qin Kuang, and Lansun Zheng. MOF encapsulated sub-nm Pd skin/Au nanoparticles as antenna-reactor plasmonic catalyst for light driven CO₂ hydrogenation. *Nano Energy*, 84:105950, June 2021.
- [156] Akihiro Furube, Luchao Du, Kohjiro Hara, Ryuzi Katoh, and Masanori Tachiya. Ultrafast Plasmon-Induced Electron Transfer from Gold Nanodots into TiO₂ Nanoparticles. *Journal of the American Chemical Society*, 129(48):14852–14853, December 2007.
- [157] Marcos Sanles-Sobrido, Miguel A. Correa-Duarte, Susana Carregal-Romero, Benito Rodríguez-González, Ramón A. Álvarez-Puebla, Pablo Hervés, and Luis M. Liz-Marzán. Highly Catalytic Single-Crystal Dendritic Pt Nanostructures Supported on Carbon Nanotubes. *Chemistry of Materials*, 21(8):1531–1535, April 2009.
- [158] Florian Schulz, Steffen Tober, and Holger Lange. Size-Dependent Phase Transfer Functionalization of Gold Nanoparticles To Promote Well-Ordered Self-Assembly. *Langmuir*, 33(50):14437–14444, December 2017.

- [159] Niclas S. Mueller, Bruno G. M. Vieira, Florian Schulz, Patryk Kusch, Valerio Oddone, Eduardo B. Barros, Holger Lange, and Stephanie Reich. Dark Interlayer Plasmons in Colloidal Gold Nanoparticle Bi- and Few-Layers. *ACS Photonics*, 5(10):3962–3969, October 2018.
- [160] Robert L Olmon, Brian Slovick, Timothy W Johnson, David Shelton, Sang-Hyun Oh, Glenn D Boreman, and Markus B Raschke. Optical dielectric function of gold. *Physical Review B*, 86(23):235147, 2012.
- [161] Edward D. Palik. *Handbook of Optical Constants of Solids*, volume 1. Academic Press, Boston, 1985.
- [162] Matias Herran, Sabrina Juergensen, Moritz Kessens, Dominik Hoening, Andrea Köppen, Ana Sousa-Castillo, Wolfgang J. Parak, Holger Lange, Stephanie Reich, Florian Schulz, and Emiliano Cortés. Plasmonic bimetallic two-dimensional supercrystals for H₂ generation. *Nature Catalysis*, 6(12):1205–1214, December 2023.
- [163] Michael Deffner. *Charge Transport through Molecules and Nanoparticles*. doctoralThesis, Universität Hamburg, Hamburg, 2020.
- [164] Shaunak Mukherjee, Florian Libisch, Nicolas Large, Oara Neumann, Lisa V. Brown, Jin Cheng, J. Britt Lassiter, Emily A. Carter, Peter Nordlander, and Naomi J. Halas. Hot Electrons Do the Impossible: Plasmon-Induced Dissociation of H₂ on Au. *Nano Letters*, 13(1):240–247, January 2013.
- [165] Ajay P. Manuel, Aaron Kirkey, Najia Mahdi, and Karthik Shankar. Plexcitonics – fundamental principles and optoelectronic applications. *Journal of Materials Chemistry C*, 7(7):1821–1853, February 2019.
- [166] K. George Thomas and Prashant V. Kamat. Chromophore-Functionalized Gold Nanoparticles. *Accounts of Chemical Research*, 36(12):888–898, December 2003.
- [167] Michał Malicki, Joel M. Hales, Mariacristina Rumi, Stephen Barlow, LaKeisha McClary, Seth R. Marder, and Joseph W. Perry. Excited-state dynamics and dye–dye interactions in dye-coated gold nanoparti-

cles with varying alkyl spacer lengths. *Physical Chemistry Chemical Physics*, 12(23):6267–6277, June 2010.

Chapter 8

Appendix

Acknowledgements

Although I am the sole author of this thesis, none of my work would have been possible without the many people that have helped me along the journey and I want to express my gratitude towards all of them. In particular, I want to thank

Dr. Holger Lange for giving me the opportunity to work in his group, for his supervision and for his mentorship, especially during rough patches of my work and life,

my colleagues in the Lange group: Yannic Stächelin, Shivani Kesarwani, Sandra Hinz, Claudio Pineda-Bosque, Michael Deffner and Florian Schulz, for their help in optical lab work, sample preparation or proof reading as well as the many, many fruitful discussions, general support and great working atmo-

sphere, this also includes all the students that I had the pleasure to work with during their Bachelor or Master thesis, in particular Kai-Fu Wong,

my collaborators from the group of Prof. Andreas Knorr at TU Berlin, in particular Robert Salzwedel and Dr. Malte Selig, for the development of the theoretical framework to explain the breathing mode excitation,

my collaborators from the groups of Prof. Jochen Küpper at CFEL, Dr. Kartik Ayyer at MPI-MPSD and the team at the CAMP endstation at FLASH, DESY, for all their work in conducting and analyzing the single-particle imaging experiment,

my collaborators from the group of Prof. Stephanie Reich at FU Berlin, in particular Sabrina Jürgensen, and the group of Prof. Emiliano Cortes, in particular Dr. Matias Heran, for their work in studying the photocatalytic properties of Au-Pt hybrid superlattices,

my colleagues at the Department of Chemistry, Universität Hamburg for their services, such as the EM service for TEM imaging, IT service, and all other teams that keep the university running and thereby facilitated my research,

my funding agency, the Cluster of Excellence "CUI: Advanced Imaging of Matter", for financial support and in particular the CUI Office, the Graduate School and the Student Representatives for supporting me in my professional development,

and last but not least all my friends and my family for their lifelong emotional support. Thank you all!

List of Figures

2.1	Depiction of different plasmon oscillation types in gold. . . .	20
2.2	Dispersion relation of volume plasmons and reflectivity depending on plasma frequency.	22
2.3	Refractive index of gold	23
2.4	Dispersion relation of surface plasmon polaritons.	24
2.5	Simulated absorbance spectrum of a 40 nm AuNP.	26
2.6	Size-dependent extinction-, absorption- and scattering cross sections by Mie-theory	27
2.7	Temperature dependence of gold absorbance	30
2.8	Overview of the hot electron dynamics in AuNP	31
2.9	Electron and lattice temperatures simulated by two-temperature model	36
2.10	Typical e-ph coupling time vs. $\Delta T_{el}^{init.}$ for AuNP.	38

2.11	Crystallinity assessment of AuNP by TEM, UV-Vis spectroscopy and x-ray diffraction	40
2.12	Size- and crystallinity dependent electron-phonon coupling constant	41
3.1	Schematic of transient absorption spectroscopy. An optical pump pulse excites the sample and the absorbance of a time-delayed probe pulse is determined. By referencing the absorbance in the excited state with the absorbance at ground state a differential absorption spectrum is determined per delay time. Scanning a delay time window allows to assess the dynamics of the differential absorption.	46
3.2	Exemplary transient absorption data	47
3.3	Minimum values of the difference in extinction cross section ΔQ_{ext} as a function of electron temperature differences ΔT_e	48
3.4	Schematic of the TA spectrometer used in this work.	49
3.5	Illustration of chirped laser pulses in a frame moving with the pulse.	51
3.6	Example of an intensity autocorrelation measurement at the laser output	56
3.7	Analysis of the coherent artifact in TA to determine the time resolution.	57
3.8	Chirp correction	58
3.9	Data analysis of the bleach kinetic	58
3.10	AuNP seeded growth synthesis	63


















4.1	Gold lattice heat capacity	70
4.2	Lattice heat capacity influence on two temperature model	71
4.3	Sample characterization for temperature-dependent TA	72
4.4	Comparison of TA power series quality.	74
4.5	Bleach kinetics: different fits	75
4.6	TA kinetics fit: quality assessment	76
4.7	TA pressure test	77
4.8	Increase in electron temperature calculated as described in Eqs. 4.3 and 4.4.	78
4.9	E-ph coupling times obtained from TA and the 2TM vs. increase in electron temperature after optical excitation.	78
4.10	Temperature dependent TA fit discussion	80
5.1	Updated overview of the hot electron dynamics, including the new direct breathing mode excitation.	85
5.2	Example of breathing mode observation in TA spectroscopy.	86
5.3	Predictions of the breathing mode onset by our microscopic theory.	93
5.4	Illustration of SAXS on AuNP. Incident x-rays with wave vector \mathbf{k}_0 are scattered by the particle. \mathbf{k}' denotes the wave vector of the scattered light at a given deviation from the incident x-rays. The deviation is described by the scattering vector \mathbf{q}	96
5.5	Illustration of single-particle imaging	98

5.6	Sketch of the experimental setup at the BL1 endstation for the SPI experiment.	101
5.7	Model diffraction patterns for analysis of the SPI data.	104
5.8	Exemplary breathing mode fitting.	107
5.9	UV-Vis spectrum of the AuNP-batch used for breathind mode study.	109
5.10	TEM analysis of the AuNP-batch used for breathing mode study.	110
5.11	Particle diameter obtained from SPI	112
5.12	TA results of breathing mode	113
5.13	Breathing mode experiments-theory comparison	115
5.14	Breathing mode fluence-dependent phase: theory and experiments	116
6.1	Optical properties of AuNP superlattices. From Ref. [11]	122
6.2	Illustration of the evaporation induced self-assembly of AuNP at a liquid-liquid interface.	125
6.3	Wavelength-dependent e-ph coupling times of a AuNP superlattice. From Ref. [50]	127
6.4	TEM analysis of photocatalysis sample	135
6.5	Absorbance spectra of AuNP-PtNP mixture, PtNP solution, AuNP superlattice and Au-Pt superlattice	136
6.6	Comparison of the hydrogen production in the photocatalytic reaction between the samples and illumination levels	137

6.7	Measured hydrogen yield depending on the excitation wavelength related to the local E-field enhancement simulated by FDTD simulations [162].	138
6.8	Simulation of wavelength dependent E-field enhancement by FDTD	139
6.9	a) Steady state NIR absorbance spectrum of a AuNP superlattice. b) NIR probe TA measurement of a AuNP superlattice. The excitation wavelength was 450 nm.	140
6.10	TA results of the AuNP and Au-Pt superlattice	142
6.11	Influence of PtNP on the TA signal	144

List of chemicals

chemical	GHS togram	pic-	hazard statements (H)	precautionary statements (P)
11-mercaptoundecanoic acid			315, 319, 335	261, 264, 271, 280, 302+352, 305+351+338
acetone			225, 319, 336, EUH066	210, 240, 305+351+338, 403+233
aqua regia			272, 314	210, 220, 221, 280, 303+361+353, 305+351+338+310
cetyltrimethylammonium bromide			302, 315, 318, 335, 373, 410	273, 280, 301+312, 302+352, 305+351+338, 314
cetyltrimethylammonium chloride			302, 311, 314, 410	280, 301+330+331, 303+361+353, 305+351+338
chloroform			302, 331, 315, 319, 351, 361d, 336, 372, 412	201, 273, 301+312+330, 302+352, 304+340+311, 308+313

chemical	GHS togram	pic-	hazard state- ments (H)	precautionary statements (P)
diethylene glycol	 		302, 373	360, 301+312+330
ethanol	 		225, 319	210, 240, 305+351+338, 403+223
hydrochloric acid	 		290, 314, 335	280, 303+361+353, 305+351+338+310
methanol	  		225, 301+311+331, 370	210, 233, 280, 301+310, 303+361+353, 304+340+311
nitric acid	  		272, 290, 330, 314, EUH071	210, 220, 280, 303+361+353, 304+340+310, 305+351+338
sodium borohydride	   		260, 301, 314, 360F, EUH014	201, 231+232, 280, 308+313, 370+378, 402+404
sodium hydroxide			290, 314	280, 301+330+331, 305+351+338

chemical	GHS togram	pic-	hazard statements (H)	precautionary statements (P)
tetrachloroauric acid	 		290, 302, 314, 373, 411	260, 273, 280, 303+361+353, 305+351+338, 314
tetrahydrofuran	 		225, 302, 319, 335, 336, 351, EUH019	210, 280, 301+312+330, 305+351+338, 370+378, 403+235
toluene	 		225, 304, 315, 336, 361d, 373	210, 240, 301+310+330, 302+352, 314, 403+233

Table 8.2: All H, EUH, and P Statements.

Identifier	Statement
H200	Unstable explosives.
H201	Explosive; mass explosion hazard.
H202	Explosive, severe projection hazard.
H203	Explosive; fire, blast or projection hazard.
H204	Fire or projection hazard.
H205	May mass explode in fire.
H220	Extremely flammable gas.
H221	Flammable gas.

continues on next page

Identifier	Statement
H222	Extremely flammable aerosol.
H223	Flammable aerosol.
H224	Extremely flammable liquid and vapour.
H225	Highly flammable liquid and vapour.
H226	Flammable liquid and vapour.
H228	Flammable solid.
H240	Heating may cause an explosion.
H241	Heating may cause a fire or explosion.
H242	Heating may cause a fire.
H250	Catches fire spontaneously if exposed to air.
H251	Self-heating; may catch fire.
H252	Self-heating in large quantities; may catch fire.
H260	In contact with water releases flammable gases which may ignite spontaneously.
H261	In contact with water releases flammable gases.
H270	May cause or intensify fire; oxidiser.
H271	May cause fire or explosion; strong oxidiser.
H272	May intensify fire; oxidiser.
H280	Contains gas under pressure; may explode if heated.
H281	Contains refrigerated gas; may cause cryogenic burns or injury.
H290	May be corrosive to metals.
H300	Fatal if swallowed.
H301	Toxic if swallowed.
H302	Harmful if swallowed.
H304	May be fatal if swallowed and enters airways.

continues on next page

Identifier	Statement
H310	Fatal in contact with skin.
H311	Toxic in contact with skin.
H312	Harmful in contact with skin.
H314	Causes severe skin burns and eye damage.
H315	Causes skin irritation.
H317	May cause an allergic skin reaction.
H318	Causes serious eye damage.
H319	Causes serious eye irritation.
H330	Fatal if inhaled.
H331	Toxic if inhaled.
H332	Harmful if inhaled.
H334	May cause allergy or asthma symptoms or breathing difficulties if inhaled.
H335	May cause respiratory irritation.
H336	May cause drowsiness or dizziness.
H340	May cause genetic defects.
H341	Suspected of causing genetic defects.
H350	May cause cancer.
H351	Suspected of causing cancer.
H360	May damage fertility or the unborn child.
H361	Suspected of damaging fertility or the unborn child.
H362	May cause harm to breast-fed children.
H370	Causes damage to organs.
H371	May cause damage to organs.
H372	Causes damage to organs through prolonged or repeated exposure.

continues on next page

Identifier	Statement
H373	May cause damage to organs through prolonged or repeated exposure.
H400	Very toxic to aquatic life.
H410	Very toxic to aquatic life with long lasting effects.
H411	Toxic to aquatic life with long lasting effects.
H412	Harmful to aquatic life with long lasting effects.
H413	May cause long lasting harmful effects to aquatic life.
H350i	May cause cancer by inhalation.
H360F	May damage fertility.
H360D	May damage the unborn child.
H361f	Suspected of damaging fertility.
H361d	Suspected of damaging the unborn child.
H360FD	May damage fertility. May damage the unborn child.
H361fd	Suspected of damaging fertility. Suspected of damaging the unborn child.
H360Fd	May damage fertility. Suspected of damaging the unborn child.
H360Df	May damage the unborn child. Suspected of damaging fertility.
EUH001	Explosive when dry.
EUH006	Explosive with or without contact with air.
EUH014	Reacts violently with water.
EUH018	In use may form flammable/explosive vapour-air mixture.
EUH019	May form explosive peroxides.
EUH044	Risk of explosion if heated under confinement.
EUH029	Contact with water liberates toxic gas.

continues on next page

Identifier	Statement
EUH031	Contact with acids liberates toxic gas.
EUH032	Contact with acids liberates very toxic gas.
EUH066	Repeated exposure may cause skin dryness or cracking.
EUH070	Toxic by eye contact.
EUH071	Corrosive to the respiratory tract.
EUH059	Hazardous to the ozone layer.
EUH201	Contains lead. Should not be used on surfaces liable to be chewed or sucked by children.
EUH201A	Warning! contains lead.
EUH202	Cyanoacrylate. Danger. Bonds skin and eyes in seconds. Keep out of the reach of children.
EUH203	Contains chromium (VI). May produce an allergic reaction.
EUH204	Contains isocyanates. May produce an allergic reaction.
EUH205	Contains epoxy constituents. May produce an allergic reaction.
EUH206	Warning! Do not use together with other products. May release dangerous gases (chlorine).
EUH207	Warning! Contains cadmium. Dangerous fumes are formed during use. See information supplied by the manufacturer. Comply with the safety instructions.
EUH208	Contains <i><name of sensitising substance></i> . May produce an allergic reaction.
EUH209	Can become highly flammable in use.
EUH209A	Can become flammable in use.
EUH210	Safety data sheet available on request.

continues on next page

Identifier	Statement
EUH401	To avoid risks to human health and the environment, comply with the instructions for use.
P101	If medical advice is needed, have product container or label at hand.
P102	Keep out of reach of children.
P103	Read label before use.
P201	Obtain special instructions before use.
P202	Do not handle until all safety precautions have been read and understood.
P210	Keep away from heat/sparks/open flames/hot surfaces. — No smoking.
P211	Do not spray on an open flame or other ignition source.
P220	Keep/Store away from clothing/.../combustible materials.
P221	Take any precaution to avoid mixing with combustibles ...
P222	Do not allow contact with air.
P223	Keep away from any possible contact with water, because of violent reaction and possible flash fire.
P230	Keep wetted with ...
P231	Handle under inert gas.
P232	Protect from moisture.
P233	Keep container tightly closed.
P234	Keep only in original container.
P235	Keep cool.
P240	Ground/bond container and receiving equipment.

continues on next page

Identifier	Statement
P241	Use explosion-proof electrical/ventilating/lighting/... equipment.
P242	Use only non-sparking tools.
P243	Take precautionary measures against static discharge.
P244	Keep reduction valves free from grease and oil.
P250	Do not subject to grinding/shock/.../friction.
P251	Pressurized container: Do not pierce or burn, even after use.
P260	Do not breathe dust/fume/gas/mist/vapours/spray.
P261	Avoid breathing dust/fume/gas/mist/vapours/spray.
P262	Do not get in eyes, on skin, or on clothing.
P263	Avoid contact during pregnancy/while nursing.
P264	Wash ... thoroughly after handling.
P270	Do not eat, drink or smoke when using this product.
P271	Use only outdoors or in a well-ventilated area.
P272	Contaminated work clothing should not be allowed out of the workplace.
P273	Avoid release to the environment.
P280	Wear protective gloves/protective clothing/eye protection/face protection.
P281	Use personal protective equipment as required.
P282	Wear cold insulating gloves/face shield/eye protection.
P283	Wear fire/flame resistant/retardant clothing.
P284	Wear respiratory protection.
P285	In case of inadequate ventilation wear respiratory protection.
P231 + P232	Handle under inert gas. Protect from moisture.

continues on next page

Identifier	Statement
P235 + P410	Keep cool. Protect from sunlight.
P301	IF SWALLOWED:
P302	IF ON SKIN:
P303	IF ON SKIN (or hair):
P304	IF INHALED:
P305	IF IN EYES:
P306	IF ON CLOTHING:
P307	IF exposed:
P308	IF exposed or concerned:
P309	IF exposed or if you feel unwell:
P310	Immediately call a POISON CENTER or doctor/physician.
P311	Call a POISON CENTER or doctor/physician.
P312	Call a POISON CENTER or doctor/physician if you feel unwell.
P313	Get medical advice/attention.
P314	Get medical advice/attention if you feel unwell.
P315	Get immediate medical advice/attention.
P320	Specific treatment is urgent (see ... on this label).
P321	Specific treatment (see ... on this label).
P322	Specific measures (see ... on this label).
P330	Rinse mouth.
P331	Do NOT induce vomiting.
P332	If skin irritation occurs:
P333	If skin irritation or rash occurs:
P334	Immerse in cool water/wrap in wet bandages.

continues on next page

Identifier	Statement
P335	Brush off loose particles from skin.
P336	Thaw frosted parts with lukewarm water. Do not rub affected area.
P337	If eye irritation persists:
P338	Remove contact lenses, if present and easy to do. Continue rinsing.
P340	Remove victim to fresh air and keep at rest in a position comfortable for breathing.
P341	If breathing is difficult, remove victim to fresh air and keep at rest in a position comfortable for breathing.
P342	If experiencing respiratory symptoms:
P350	Gently wash with plenty of soap and water.
P351	Rinse cautiously with water for several minutes.
P352	Wash with plenty of soap and water.
P353	Rinse skin with water/shower.
P360	Rinse immediately contaminated clothing and skin with plenty of water before removing clothes.
P361	Remove/Take off immediately all contaminated clothing.
P362	Take off contaminated clothing and wash before reuse.
P363	Wash contaminated clothing before reuse.
P370	In case of fire:
P371	In case of major fire and large quantities:
P372	Explosion risk in case of fire.
P373	DO NOT fight fire when fire reaches explosives.
P374	Fight fire with normal precautions from a reasonable distance.

continues on next page

Identifier	Statement
P375	Fight fire remotely due to the risk of explosion.
P376	Stop leak if safe to do so.
P377	Leaking gas fire: Do not extinguish, unless leak can be stopped safely.
P378	Use ... for extinction.
P380	Evacuate area.
P381	Eliminate all ignition sources if safe to do so.
P390	Absorb spillage to prevent material damage.
P391	Collect spillage.
P301 + P310	IF SWALLOWED: Immediately call a POISON CENTER or doctor/physician.
P301 + P312	IF SWALLOWED: Call a POISON CENTER or doctor/physician if you feel unwell.
P301 + P330 + P331	IF SWALLOWED: rinse mouth. Do NOT induce vomiting.
P302 + P334	IF ON SKIN: Immerse in cool water/wrap in wet bandages.
P302 + P350	IF ON SKIN: Gently wash with plenty of soap and water.
P302 + P352	IF ON SKIN: Wash with plenty of soap and water.
P303 + P361 + P353	IF ON SKIN (or hair): Remove/Take off immediately all contaminated clothing. Rinse skin with water/shower.
P304 + P340	IF INHALED: Remove victim to fresh air and keep at rest in a position comfortable for breathing.
P304 + P341	IF INHALED: If breathing is difficult, remove victim to fresh air and keep at rest in a position comfortable for breathing.

continues on next page

Identifier	Statement
P305 + P351 + P338	IF IN EYES: Rinse cautiously with water for several minutes. Remove contact lenses, if present and easy to do. Continue rinsing.
P306 + P360	IF ON CLOTHING: Rinse immediately contaminated clothing and skin with plenty of water before removing clothes.
P307 + P311	IF exposed: Call a POISON CENTER or doctor/physician.
P308 + P313	IF exposed or concerned: Get medical advice/attention.
P309 + P311	IF exposed or if you feel unwell: Call a POISON CENTER or doctor/physician.
P332 + P313	If skin irritation occurs: Get medical advice/attention.
P333 + P313	If skin irritation or rash occurs: Get medical advice/attention.
P335 + P334	Brush off loose particles from skin. Immerse in cool water/wrap in wet bandages.
P337 + P313	If eye irritation persists: Get medical advice/attention.
P342 + P311	If experiencing respiratory symptoms: Call a POISON CENTER or doctor/physician.
P370 + P376	In case of fire: Stop leak if safe to do so.
P370 + P378	In case of fire: Use ... for extinction.
P370 + P380	In case of fire: Evacuate area.
P370 + P380 + P375	In case of fire: Evacuate area. Fight fire remotely due to the risk of explosion.
P371 + P380 + P375	In case of major fire and large quantities: Evacuate area. Fight fire remotely due to the risk of explosion.
P401	Store ...

continues on next page

Identifier	Statement
P402	Store in a dry place.
P403	Store in a well-ventilated place.
P404	Store in a closed container.
P405	Store locked up.
P406	Store in corrosive resistant/... container with a resistant inner liner.
P407	Maintain air gap between stacks/pallets.
P410	Protect from sunlight.
P411	Store at temperatures not exceeding °C/°F.
P412	Store at temperatures not exceeding 50 °C/122 °F.
P413	Store bulk masses greater than kg/lbs at temperatures not exceeding °C/°F.
P420	Store away from other materials.
P422	Store contents under ...
P402 + P404	Store in a dry place. Store in a closed container.
P403 + P233	Store in a well-ventilated place. Keep container tightly closed.
P403 + P235	Store in a well-ventilated place. Keep cool.
P410 + P403	Protect from sunlight. Store in a well-ventilated place.
P410 + P412	Protect from sunlight. Do not expose to temperatures exceeding 50 °C/122 °F.
P411 + P235	Store at temperatures not exceeding °C/°F. Keep cool.
P501	Dispose of contents/container to ...

Eidesstattliche Erklärung

Hiermit versichere ich an Eides statt, die vorliegende Dissertationsschrift selbst verfasst und keine anderen als die angegebenen Quellen und Hilfsmittel benutzt zu haben.

Hamburg, 04.08.2023

Dominik Höing